Nonlinear Dynamics of Magnetic Vortices in Spin-Torque Nano-Oscillators

Simon DE WERGIFOSSE

Thesis submitted in partial fulfillment
of the requirements for the degree of
Docteur en sciences de l'ingénieur et technologie

Dissertation committee:

Prof. Flavio ABREU ARAUJO	*Supervisor*	UCLouvain, Belgium
Prof. Evelyne VAN RUYMBEKE	*President*	UCLouvain, Belgium
Prof. Benoit HACKENS	*Secretary*	UCLouvain, Belgium
Prof. Luc PIRAUX		UCLouvain, Belgium
Dr. Grégoire DE LOUBENS		SPEC, France
Dr. Philippe TALATCHIAN		SPINTEC, France

November 2025

Contents

Abstract

NONLINEAR science explores systems for which the principle of superposition fails to apply, meaning that the response to a combination of inputs can not be predicted by the sum of the individual outputs, helping describe phenomena in biology, optics, or condensed matter physics. This inherent complexity often renders their modeling challenging. In this thesis, the strongly nonlinear dynamics of magnetic vortices in spin-torque nano-oscillators are investigated. These devices, which are nanoscale structures able to convert direct currents to alternating voltages, rely on magnetic tunnel junction stacks for which the free layer exhibits a nonuniform vortex magnetization state. When subjected to a sufficient injected current, sustained gyrotropic precessions of the vortex core may occur, generating an oscillatory output signal through magnetoresistance effects. These dynamics are typically captured using two main approaches. Micromagnetic simulations, though delivering high accuracy, demand substantial computational resources. In contrast, the Thiele equation provides analytical solutions by modeling the vortex core as a quasiparticle, yet relying on assumptions and linearization.

In this work, we enhance the Thiele equation by improving the magnetostatic and Zeeman terms, the latter arising from the Ampère-Oersted field induced by the current. These modifications reveal a clear chirality-dependent splitting of the dynamics, validated through micromagnetic simulations. While our model remains qualitative in the steady-state oscillating regime, we introduce a method to extract the vortex stiffness, linked to the potential magnetic energy, directly from micromagnetic data. This method highlights discrepancies between analytical expressions and simulations, notably due to deformations of the magnetic texture caused by the Ampère-Oersted field. To refine our predictions, we then develop a quantitative model incorporating the vortex core position-dependence of the gyrotropic and damping terms. Due to cumbersome analytical derivations, these terms are instead calibrated using steady-state simulation results. Our data-driven Thiele equation approach achieves up to eight orders of magnitude faster computation than micromagnetism, while maintaining equivalent accuracy. It precisely reproduces both transient and steady-state dynamics, even for arbitrary input waveforms. Furthermore, our findings reveal a unique dynamical regime for larger-diameter junctions, for which the vortex core is confined between two orbits due to successive double-polarity reversals, a behavior analogous to the leaky integrate-and-fire model of biological neurons. Finally, we examine a system consisting of a pair of oscillators in close proximity, focusing on the Ampère-Oersted field influence rather than well-known synchronization through dipolar interactions. We derive an analytical expression for the associated Zeeman energy, confirmed by simulations. Lastly, we underscore the necessity of accounting for this field in theoretical models by displaying shifts in the vortex core equilibrium position and ferromagnetic resonance effects.

Author's publication list

Peer-reviewed articles

[1] F. Abreu Araujo, C. Chopin, and **S. de Wergifosse**, *Ampère-Oersted field splitting of the nonlinear spin-torque vortex oscillator dynamics*, *Scientific Reports* **12**, 10605 (2022).

[2] **S. de Wergifosse**, C. Chopin, and F. Abreu Araujo, *Quantitative and realistic description of the magnetic potential energy of spin-torque vortex oscillators*, *Physical Review B* **108**, 174403 (2023).

[3] C. Chopin, **S. de Wergifosse**, N. Marchal, P. Van Velthem, L. Piraux, and F. Abreu Araujo, *Memristive and Tunneling Effects in 3D Interconnected Silver Nanowires*, *ACS Omega* **8**, 6663-6668 (2023).

[4] T. da Câmara Santa Clara Gomes, N. Marchal, A. Moureaux, **S. de Wergifosse**, C. Chopin, L. Piraux, J. de la Torre Medina, and F. Abreu Araujo, *Geometrical properties of three-dimensional crossed nanowire networks*, *Physical Review Research* **6**, 23211 (2024).

[5] C. Chopin, **S. de Wergifosse**, A. Moureaux, and F. Abreu Araujo, *Current-controlled periodic double-polarity reversals in a spin-torque vortex oscillator*, *Scientific Reports* **14**, 24177 (2024).

Preprint articles

[1] F. Abreu Araujo, C. Chopin, and **S. de Wergifosse**, *Data-driven Thiele equation approach for solving the full nonlinear spin-torque vortex oscillator dynamics*, *arXiv:2206.13596* (2022).

[2] C. Chopin, L. Martins, L. Benetti, **S. de Wergifosse**, A. S. Jenkins, R. Ferreira, and F. Abreu Araujo, *A semi-analytical model to simulate the spin-diode effect and accelerate its use in neuromorphic computing*, *arXiv:2301.11980* (2023).

[3] A. Moureaux, **S. de Wergifosse**, C. Chopin, J. Weber, and F. Abreu Araujo, *Neuromorphic spintronics accelerated by an unconventional data-driven Thiele equation approach*, *arXiv:2301.11025v2* (2023).

[4] A. Moureaux, C. Chopin, **S. de Wergifosse**, L. Jacques, and F. Abreu Araujo, *Spintronics for image recognition: performance benchmarking via ultrafast data-driven simulations*, *arXiv:2308.05810v3* (2023).

[5] C. Ducarme, **S. de Wergifosse**, and F. Abreu Araujo, *Core position-dependent gyrotropic and damping contributions to the Thiele equation approach for accurate spin-torque vortex oscillator dynamics*, *arXiv:2508.14829v2* (2025).

Oral invited presentations at peer reviewed conferences

[1] **S. de Wergifosse**, C. Chopin, and F. Abreu Araujo, *Accelerating the simulations of spintronic oscillators using an unconventional data-driven approach*, *SPIE Spintronics XVI*, Aug 2023, San Diego (USA).

Oral presentations at peer reviewed conferences

[1] **S. de Wergifosse**, F. Abreu Araujo, and C. Chopin, *Splitting of the nonlinear spin-torque vortex oscillator dynamics originating from the Ampère-Oersted field induced by the excitation current*, *Joint MMM-Intermag XV*, Jan 2022, New Orleans (USA).

[2] **S. de Wergifosse**, C. Chopin, and F. Abreu Araujo, *Impact of the Ampère-Oersted field on the dynamics of spin-torque vortex oscillators*, *Intermag*, May 2023, Sendai (Japan).

[3] **S. de Wergifosse**, C. Chopin, A. Moureaux, and F. Abreu Araujo, *Accélération des simulations d'oscillateurs spintroniques à l'aide d'une approche non-conventionnelle guidée par les données*, *Congrès Général de la Société française de Physique XXVI*, Jul 2023, Paris (France).

[4] **S. de Wergifosse**, C. Chopin, Moureaux Anatole, and F. Abreu Araujo, *Accelerating the simulations of spintronic oscillators using an unconventional data-driven approach*, *Joint European Magnetic Symposia XIII*, Aug 2023, Madrid (Spain).

[5] **S. de Wergifosse**, C. Chopin, Moureaux Anatole, and F. Abreu Araujo, *Capturing the full analytical dynamics of spin-torque vortex oscillators from micromagnetic simulations*, *Colloque Louis Néel XXI*, Nov 2023, Sète (France).

[6] **S. de Wergifosse**, C. Chopin, Moureaux Anatole, and F. Abreu Araujo, *Quantitative Description of the Impact of the Ampère-Oersted Field on the Stiffness of Magnetic Vortices*, *Intermag*, May 2024, Rio de Janeiro (Brazil).

Poster presentations at peer reviewed conferences

[1] **S. de Wergifosse**, C. Chopin, and F. Abreu Araujo, *Quantitative data-driven model for solving the spin-torque vortex oscillator dynamics*, *Colloque Louis Néel XX*, Jun 2022, Obernai (France).

[2] C. Chopin, **S. de Wergifosse**, Moureaux Anatole, and F. Abreu Araujo, *Leaky integrate-and-fire behavior through spin-wave emission using a spin-torque vortex oscillator*, *Workshop on Neuromorphic Magnonics*, Apr 2024, Paris (France).

[3] **S. de Wergifosse**, C. Chopin, A. Moureaux, and F. Abreu Araujo, *Impact of the Ampère-Oersted field on the stiffness and texture of magnetic vortices*, *International Conference on Magnetism*, Jun 2024, Bologna (Italy).

[4] **S. de Wergifosse**, T. da Câmara Santa Clara Gomes, A. Moureaux, C. Chopin, U. Ebels, and F. Abreu Araujo, *Oersted field driven dynamics in spin-torque vortex oscillators*, *Colloque Louis Néel XXII*, Jun 2025, Vogüé (France).

List of acronyms

AC	Alternating Current
AI	Artificial Intelligence
ANN	Artificial Neural Network
(A)OF	(Ampère-)Oersted Field
AP	Antiparallel
CGS	Centimeter-Gram-Second
CMOS	Complementary Metal-Oxide-Semiconductor
CPU	Central Processing Unit
DC	Direct Current
DD-TEA	Data-Driven Thiele Equation Approach
DOS	Density Of States
FLT	Field-Like Torque
GMR	Giant Magnetoresistance
GPU	Graphics Processing Unit
IP	In-Plane
LIF	Leaky Integrate-and-Fire
LLGS	Landau-Lifshitz-Gilbert-Slonczewski
MMS	Micromagnetic Simulations
MR	Magnetoresistance
MTJ	Magnetic Tunnel Junction
ODE	Ordinary Differential Equation
OOP	Out-Of-Plane
P	Parallel
Py	Permalloy
RF	Radiofrequency
SAF	Synthetic Antiferromagnet
SI	Système International d'unités
STNO	Spin-Torque Nano-Oscillators
S(T)T	Spin(-Transfer) Torque

STVO	Spin-Torque Vortex Oscillator
SVA	Single-Vortex *Ansatz*
SW	Spin-Wave
TEA	Thiele Equation Approach
TMR	Tunnel Magnetoresistance
TVA	Two-Vortex *Ansatz*

Acknowledgements

Une thèse, c'est sans aucun doute beaucoup de souvenirs, et la plupart de ces souvenirs sont pour moi des moments partagés avec d'autres personnes.

Flavio, j'ai la chance d'être, à tout jamais, ton tout premier doctorant. Quand nous nous sommes rencontrés pour mon mémoire de master, tu étais encore post-doc', en quête d'un poste permanent. Te voilà Prof. Abreu Araujo, et directeur de ton propre groupe de recherche en ingénierie neuromorphique. Je suis fier d'avoir pu assister à cette partie essentielle de ta carrière scientifique. Merci pour la liberté que tu as toujours su me donner, tout en m'offrant un encadrement quotidien (sans organiser aucune réunion, qu'aucun de nous deux n'affectionne, ce qui n'est pas une mince prouesse). Merci pour ton intérêt pour mes résultats et tes conseils avisés à la moindre question ou sollicitation, merci pour l'ensemble des responsabilités que tu as pu me confier, et d'avoir toujours cru en moi. Tous les moments vécus en conférences avec le groupe resteront aussi marqués dans ma mémoire. Et finalement, je t'avoue que je suis sincèrement persuadé d'être meilleur que toi au Zauber.

Je remercie l'ensemble des membres de mon jury de thèse: Evelyne van Ruymbeke, Benoit Hackens, Luc Piraux, Grégoire de Loubens, et Philippe Talachian. Merci à vous d'avoir accepté de lire ces quelques pages, pour le temps que vous y avez consacré et pour vos très justes commentaires lors de ma défense privée, qui m'ont permis d'améliorer la qualité de mon manuscrit. J'espère que mes travaux ont pu vous intéresser. Un merci tout particulier à Luc, qui m'a transmis sa passion de la physique de la matière condensée à travers les différents cours qu'il a pu me donner durant mon master et pour nos discussions sur le cyclisme, et à Evelyne pour son humanité et son désir de faire de notre institut un espace de travail enrichissant scientifiquement et agréable pour tous et toutes.

Je tiens également à remercier l'ensemble des collègues que j'ai eu le bonheur de côtoyer, de près ou de loin, tout au long de ces quatre années. Anatole, j'ai eu le privilège d'être ton co-doctorant durant l'ensemble de ma thèse, que j'ai terminée avec un ami supplémentaire. Merci d'avoir accepté mes confidences, pour l'aide à la réalisation de ce template (avec Flavio), d'avoir toujours été là pour moi et pour tous les moments légers passés à deux. C'est notamment grâce à toi que je n'ai jamais eu l'impression d'aller travailler. Merci également à

Tristan pour ses merveilleux choix musicaux écoutés ensemble en travaillant et de m'avoir accepté dans son bureau historique, et à Chloé pour tout ce qu'elle m'a apporté scientifiquement et humainement. Je pense également à l'ensemble des membres de notre étage au Boltzmann, et en particulier à tous les membres des groupes de magnétisme et de rhéologie. Merci à elles et eux pour les barbecues, les parties de cartes où je n'ai pas toujours pu contrôler ma colère face à l'injustice, les gâteaux et les tartes, et l'ensemble des moments agréables passés en leur compagnie. Merci aussi à Anne pour l'ensemble des tâches qu'elle mène et qui facilitent notre quotidien, à tout le personnel administratif et technique, ainsi qu'au personnel nettoyant nos bureaux, dans des conditions de travail qui ne sont pas toujours faciles.

J'ai également eu le plaisir de pouvoir m'investir dans diverses instances de l'université. Il parait que les conversations avec des gens qu'on apprécie autour de sujets qui ont de l'importance pour nous peuvent compter comme des heures de travail. Je remercie l'ensemble des membres du Conseil CORSCI pour tous les combats menés pour une université plus juste et plus inclusive, les membres de l'ACIM pour avoir contribué à construire des ponts entre les différents pôles de notre institut, et à la Horde des Ingés en Transition pour avoir su redonner du sens à mon cursus d'ingénieur. Un merci tout particulier à Anne, pour nos trajets hebdomadaires à vélo jusqu'au travail, par tous les temps, et pour toutes les conversations que nous avons eues sur la selle.

La recherche c'est aussi des interactions avec d'autres domaines d'expertise, d'autres idées, et surtout d'autres personnes. Je remercie donc tous les partenaires avec qui j'ai eu l'occasion d'échanger, en particulier Alex et Tim chez INL pour la qualité de leurs dispositifs, le groupe d'Ursula et de Philippe à SPINTEC pour nos discussions à Grenoble, et Jack à l'Imperial College pour sa confiance et son engouement. Merci également aux trois mémorants que j'ai eu l'honneur d'encadrer et d'embarquer sur le chemin du doctorat: Anatole (toujours lui), Thomas, et plus récemment Colin. Leur enthousiasme, leurs questionnements, et leur soif d'apprendre m'auront permis de prendre du recul sur mes travaux et d'admettre que je n'avais pas toujours de réponse à leurs très justes remarques.

Je tiens également à avoir un mot pour l'ensemble du personnel médical qui m'a pris en charge depuis six ans, et qui d'une façon ou d'une autre, m'a fait aller un petit peu mieux chaque jour. J'ai une pensée particulière pour ma kinésithérapeute et pour mon psy, pour leur expertise dans leurs métiers respectifs et leur soutien sans faille.

Par ailleurs, je remercie chaleureusement l'ensemble de mes proches, ma famille et mes ami·es, pour leur support et le bonheur qu'ils et elles m'apportent au quotidien. Un tout grand merci à l'ensemble des colocs avec qui j'ai eu la chance d'habiter, et à qui j'ai eu le malheur de tenter d'expliquer ce que je faisais de mes journées. Merci à mes frères, Robin et Pierrot, et à ma soeur, Juliette, pour leur soutien et de m'avoir permis de vivre une enfance animée et heureuse. Merci à mes grands-parents, pour leur amour et leur aide depuis mes premiers devoirs. Merci à mon Papa, de m'avoir transmis son intérêt pour les sciences et son envie de découvrir le monde, et à ma Maman qui, jusqu'au bout de sa maladie, aura toujours tout fait pour nous et pour moi.

Et finalement, merci à toi Juliette ! Merci pour tes délicieux gâteaux, merci d'avoir été là pour moi depuis que nous nous sommes rencontrés, et de me rendre heureux.

Simon de Wergifosse is a FRIA grantee, of the Fonds de la Recherche Scientifique de Belgique (F.R.S.-FNRS). Computational resources have been provided by the Consortium des Équipements de Calcul Intensif (CÉCI), funded by the F.R.S.-FNRS under Grant No. 2.5020.11 and by the Walloon Region.

À ma Maman, qui aurait été tellement fière de moi.

Introduction

Context and motivation

NONLINEAR science explores physical system exhibiting nonproportional responses to input changes, thus not obeying the superposition principle. This complexity, prevalent in many natural phenomena, implies intricate dynamics and inherent challenges in predictions. Such systems are extensively investigated across diverse scientific fields, including biology, optics, climatology, and condensed matter physics [1,2,3,4]. Mathematically, nonlinear dynamics are typically modeled using differential equation systems. However, deriving analytical solutions to these models proves to be a formidable challenge, necessitating strategies like linearization to simplify analyses, albeit at the expense of accuracy and sometimes validity. In magnetism, the Landau-Lifshitz-Gilbert (LLG) equation governs magnetization dynamics in ferromagnetic materials. In particular, it can be used to capture the dynamics of the magnetic vortex state, a ground state in thin nanopillars [5,6]. This nonuniform magnetization distribution has attracted significant interest over the past decades, notably for data storage applications [7]. However, the complex magnetization of such systems hinders the derivation of direct analytical solutions to the LLG equation. Consequently, the micromagnetism formalism becomes necessary to examine these magnetic textures, through a discretization into numerous nanoscale basic-shaped cells [8]. Alternatively, the Thiele equation [9,10] approach offers a conceptual simplification by treating the vortex core as a quasiparticle, recasting the collective dynamics into a form analogous to a driven harmonic oscillator model. In parallel, recent endeavors have explored the development of physics-informed machine learning models to capture the dynamics of magnetic systems [11].

Concomitantly with advancements in vortex dynamics understanding, spin-torque nano-oscillators (STNOs) emerged [12,13,14,15], making use of magnetic tunnel junction structures to inject spin-polarized currents into a free ferromagnetic layer. This electron flow exerts a spin-transfer torque on the magnetization, enabling control of its mean magnetic moment direction. By magnetoresistance measurements, an alternating signal can be retrieved from a constant current input, making them compact dc-to-ac converters. For specific geometries, the free layer may exhibit a vortex as its magnetic ground state, leading to the development of the so-called spin-torque vortex oscillators (STVOs) [16,17]. In such devices, the vortex core is initially at rest at the center of the nanodot. Upon applying a sufficient input current density, steady-state magnetization oscillations occur, in the hundreds-of-MHz range, driven by the off-centered precessing vortex core. STVOs offer numerous interesting properties [16], including nanoscale dimensions, low noise sensitivity, narrow bandwidth and wide frequency tunability. These attributes have rendered these spintronic devices appealing for various prospective applications, such as radiofrequency (rf) signal transmission and detection [18], neuromorphic computing [19,20], or solving optimization problems [21]. Notably, STVOs already demonstrated promising results in pattern recognition tasks.

Despite important theoretical efforts, none of the above-mentioned methods is particularly suited to processing long-duration input signals, due to quantitative limitations or computational inefficiency. This is particularly apparent when input signals of arbitrary shapes are considered, or when several oscillators interact with each other.

Thesis objectives

This thesis aims at achieving three objectives, outlined below, to fill some gaps in the current literature. Primarily, we endeavor to refine several existing theoretical works, and to propose a novel quantitative model, which would be fast, yet accurate.

Objective n°1: Analytical models based on the Thiele equation suffer from inaccuracies under high excitation, common in STVOs, due to linearization. We thus aim to enhance the magnetic energy terms, governing the vortex stiffness, by taking into account higher-order effects and the Ampère-Oersted field influence.

Objective n°2: The often neglected nonlinearity of the gyrotropic and damping terms, usually assumed constant, will be addressed by incorporating the vortex core position dependence. Subsequently, we should be able to develop a quantitative model for the dynamics.

Objective n°3: The dipolar interactions between oscillators have already been studied, notably for synchronization purposes. However, the influence of the Ampère-Oersted field is systematically overlooked. A term incorporating this Zeeman energy component should therefore be introduced to account for its impact.

Thesis overview

This work includes four Chapters, each summarized by a take-home message, encapsulating our main findings.

Chapter 1 provides a comprehensive overview of the current state-of-the-art in spintronics and nanomagnetism, introducing the subsequent Chapters and highlighting unresolved challenges in the field. It also explores prospective applications for spin-torque nano-oscillators.

In **Chapter 2**, we develop an analytical model based on the Thiele equation, incorporating high-order magnetostatic and Zeeman energy terms, the latter being induced by the Ampère-Oersted field. We demonstrate a chirality-dependent splitting of the dynamics, and present a method for extracting vortex stiffness from micromagnetic simulations. Furthermore, we demonstrate the impact of the Ampère-Oersted field on the magnetic texture, influencing the dynamics.

Chapter 3 introduces a data-driven model based on the Thiele equation, accounting for gyrotropic and damping term variations with vortex core position. This approach offers up to eight orders of magnitude faster calculations over simulations, while maintaining accuracy and facilitates predictions under long-duration arbitrary currents. Additionally, we highlight a unique oscillatory regime where successive core polarity reversals confine the dynamics between two boundary orbits.

In **Chapter 4**, we investigate the impact of the Ampère-Oersted field from an adjacent oscillator on an STVO placed in close proximity. We derive an analytical expression for the associated Zeeman energy and showcase ferromagnetic resonance effects and equilibrium position shifts.

Finally, this thesis is concluded with a general summary, highlighting our specific findings, acknowledging its limitations, and proposing perspectives for future works.

1
State-of-the-art

MAGNETISM has been around for hundreds of years, from the advent of the navigation compass to souvenir magnets decorating our fridges. However, recent decades have witnessed unprecedented advancements in nanofabrication techniques and quantum mechanics understanding, unveiling extraordinary and often counterintuitive phenomena at the nanoscales. Magnetism is no exception to this paradigm shift. Spin-torque vortex oscillators (STVOs) exemplify perfectly this situation, operating on many principles inconceivable a century ago.

This Chapter presents the state-of-the-art in the field, essential for understanding the following Chapters. First, fundamental spintronic concepts are discussed, including magnetoresistance and spin-transfer torque effects. Subsequently, it delves into nanoscale magnetism, with a particular focus on the vortex state and the theoretical frameworks for its investigation. Finally, these concepts are merged to explore spintronic oscillators, particularly STVOs, and their prospective applications.

1.1 Spintronics

Until the 20^{th} century, electronics solely focused on charge transport. Mott's theoretical work expanded this view by proposing spin-polarized currents in ferromagnetic materials. Experimental validation by Albert Fert, in the seventies, marked the actual birth of spintronics, which makes use of both electron charge and spin. This discovery led to significant advancements in magnetic data storage technologies through magnetoresistance effects, among other applications.

Here, the fundaments of spintronics are presented, beginning with spin-dependent electron transport in ferromagnets, then introducing giant and tunnel magnetoresistance, and finishing with an introduction to spin-transfer torques, which are critical for vortex excitation in spin-torque nano-oscillators.

1.1.1 Spin-dependent electronic transport

In iron, nickel, and cobalt, which are $3d$-transition metals, the electron conduction is spin-dependent due to their high density of states (DOS) at the Fermi level E_F, situated within the narrow d-band. This large DOS $N(E_F)$ allows to satisfy the Stoner criterion [22]:

$$\mathcal{I}N(E_F) > 1, \tag{1.1}$$

where $\mathcal{I}$ quantifies the exchange interaction strength. Consequently, a spontaneous energy band splitting occurs as the system minimizes energy by creating a spin imbalance, due to the Coulomb interaction and Pauli exclusion principle, despite the associated cost in kinetic energy.

As depicted in Figure 1.1, in paramagnetic metals like copper, both spin half-bands exhibit equal density of states, leading to a non-spin-dependent electrical conduction. Conversely, in $3d$-ferromagnetic metals such as cobalt, the exchange interaction splits the spin half-bands, resulting in a partial filling of the minority spin electron d-band states up to the Fermi energy, and a net magnetic moment due to the majority-minority spin imbalance.

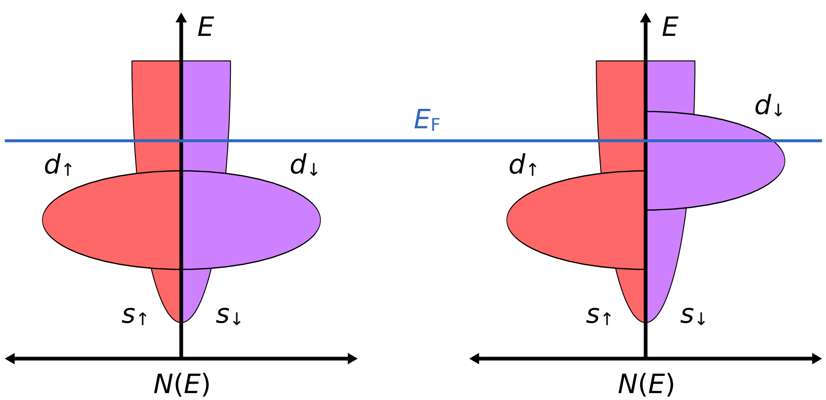

Figure 1.1: Schematic of the density of states $N(E)$ of the $4s$ and $3d$-bands in transition metals, near the Fermi level E_F. For a paramagnetic material like copper (left), the two spin half-bands are symmetrical. In ferromagnetic materials like cobalt (right), spin-dependent band splitting occurs, resulting in spontaneous magnetization.

In metals, the Drude-Lorentz model provides a simple expression for electron mobility:

$$\mu_e = \frac{e\tau}{m_e^*}, \tag{1.2}$$

where e is the electron charge, τ denotes the mean free time between scattering events, and m_e^* is the effective mass of the charge carriers. An analysis of the band structure reveals that s-electron bands exhibit a larger curvature, compared to d-electron bands. Consequently, s-electrons present a significantly smaller effective mass, rendering them the primary carriers of the electrical current. In $3d$-ferromagnetic materials, a spin-dependent scattering therefore governs the electrical conduction due to the spin-polarized DOS at the Fermi level. Minority spin electrons experience an important scattering probability, because of the large number of available states within the $3d$-band, which reduces the mean free time between scattering events. In contrast, majority spin electrons encounter fewer accessible states at the Fermi level, as the transitions are limited to the $s-s$ type. This results in a diminished scattering probability for majority spin electrons.

In this context, Mott proposed a two-channel model for electron transport [23], arising from the direct relationship between conductivity and mean free time. Within this framework, the total current density J is given as

$$J = J_\downarrow + J_\uparrow, \tag{1.3}$$

which sums the majority and minority spin contributions. As the currents are in a parallel configuration, a global resistivity can be calculated as

$$\rho = \frac{1}{\left(\frac{1}{\rho_\downarrow} + \frac{1}{\rho_\uparrow}\right)}, \tag{1.4}$$

where $\rho_\downarrow$ and $\rho_\uparrow$ are the channel-specific resistivities, which account for the higher conductivity of majority electrons compared to minority ones, as illustrated in Figure 1.2.

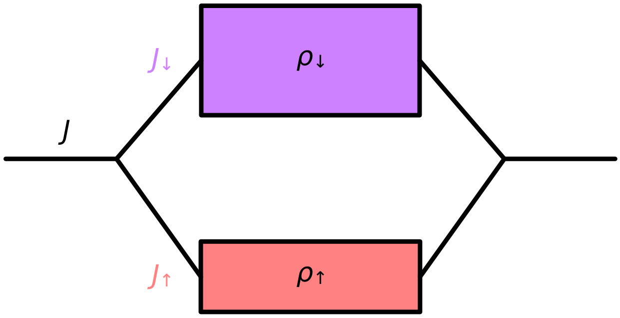

Figure 1.2: Mott's two-channel model, depicting the spin-dependent electron conduction in ferromagnetic materials, as majority and minority spin electron channels exhibit different resistivities.

Low temperatures are required for such model validity, ensuring that the spin diffusion length l_{sd} (of the order of the nm to hundreds-of-nm, depending on the material and temperature) significantly exceeds the electron mean free path [24]. Failure to meet this condition results in a short-circuit between the current channels, due to spin-flip events.

1.1.2 Magnetoresistance

Based on these spin-dependent conduction properties, extensive research has been conducted on magnetic thin films separated with nonmagnetic spacers (*e.g.*, Cu or Cr). In the eighties, Fert [25] and Grünberg [26] independently discovered giant magnetoresistance (GMR), a phenomenon that significantly exceeds anisotropic magnetoresistance effects, for which they were jointly awarded the 2007 Nobel Prize in Physics.

When the magnetizations of the two successive ferromagnetic layers are aligned parallel, a spin-polarized current with majority spins parallel to the magnetization experience minimal scattering at the interface, facilitating efficient conduction. Conversely, an antiparallel configuration results in a high resistance state, due to increased scattering for both spin channels. Therefore, considering an antiferromagnetic coupling between ferromagnetic layers [27], the resistance peaks at zero field and decreases under applied magnetic fields, yielding a characteristic bell-shaped magnetoresistance curve. The magnitude of the magnetoresistance (MR) effect is quantified as

$$\mathrm{MR} = \frac{R_{\mathrm{AP}} - R_{\mathrm{P}}}{R_{\mathrm{P}}}, \tag{1.5}$$

where R_{AP} and R_P denote resistances in antiparallel and parallel configurations, respectively.

Although GMR can reach values of tens of percents, the spin-filtering efficiency of the structure is imperfect and led to the development of alternative approaches. As a result, metallic spacers were substituted with oxide barriers (*e.g.*, MgO or Al_2O_3), yielding magnetic tunnel junctions (MTJs) and their tunnel magnetoresistance (TMR) properties [28,29,30]. The physical principle differs from GMR stacks, as it relies on the spin-dependent tunneling probability across the oxide barrier of majority and minority spin electrons. Nonetheless, the resulting effect is similar to that of GMR, in the sense that a parallel configuration shows lower resistance than an antiparallel one. Since then, advancements in nanofabrication techniques have enabled TMR ratios exceeding hundreds of percents [31], as displayed in Figure 1.3.

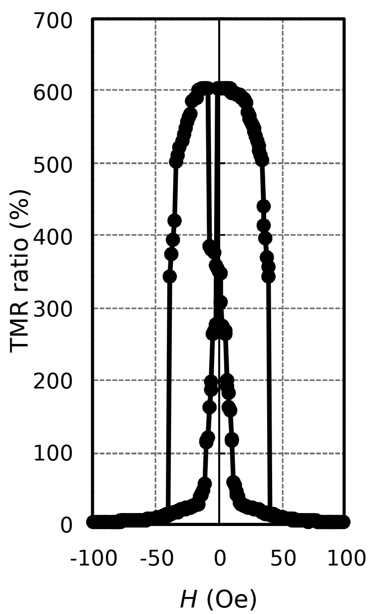

Figure 1.3: Magnetoresistance loop at 300 K of a CoFeB/MgO/CoFeB pseudo-spin-valve magnetic tunnel junction annealed at 525 °C. TMR ratio is as high as 604 % at 300 K. Reproduced from Ikeda *et al.* [32], with permission of the *American Institute of Physics*.

For practical implementations, a synthetic antiferromagnet typically pins one of the two ferromagnetic layers, in a pseudo-spin-valve configuration. The other ferromagnetic layer, thinner and designated as the free layer, can switch magnetization at low magnetic fields. Therefore, only the free layer magnetization flips direction under standard operating conditions of the MTJ, with the polarizer, *i.e.*, the fixed layer, serving as a reference magnetization.

1.1.3 Spin-transfer torque

Spin-transfer torque (STT) is a mechanism of quantum origin enabling the local manipulation of the magnetization of thin magnetic layers without requiring external magnetic fields [33,34,35], as illustrated in Figure 1.4.

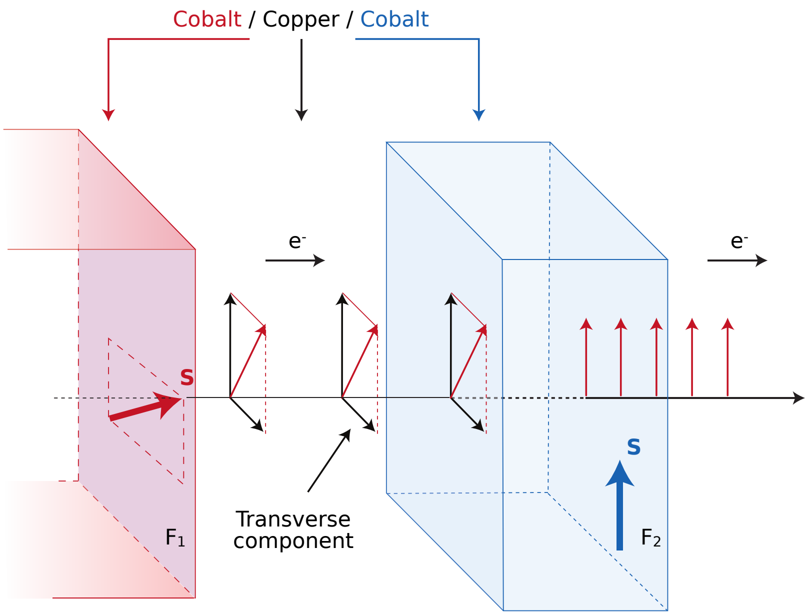

Figure 1.4: Principle of the STT effect, for a typical case Co(F_1)/Cu/Co(F_2) trilayer pillar. A current of *s*-electrons flowing from left to right will acquire through F_1 (assumed to be thick and acting as a spin-polarizer) an average spin moment along the magnetization of F_1. When the electrons reach F_2, the $s-d$ exchange interaction quickly aligns the average spin moment along the magnetization of F_2. To conserve the total angular momentum, the transverse spin angular momentum lost by the electrons is transferred to the magnetization of F_2, which senses a resulting torque tending to align its magnetization towards F_1. Reproduced from Chappert *et al.* [36], with permission of *Springer Nature*.

This phenomenon typically involves a trilayer structure, made of a polarizer with fixed magnetization, a nonmagnetic spacer, and a free ferromagnetic layer. Upon injecting a perpendicular-to-plane current through this multilayer, electrons become spin-polarized, aligning with the polarization direction. These spin-polarized electrons are then transferred to the free layer, whose initial magnetization may not align with that of the polarizer. *Via* exchange interaction, electron spins align with the free layer magnetization while transferring their transverse component. Due to the conservation of the total angular momentum, a spin-transfer torque is therefore generated within the free layer [37]. This torque can induce complete switching of magnetization, enabling local bit writing in STT-magnetic random access memories, or sustained magnetization oscillations, as will be discussed in Section 1.3.

It is critical to emphasize that large current densities are necessary for STT to impact significantly the magnetization in the free layer [24]. Consequently, nanoscale structures likes nanopillars are usually employed, delivering current densities of the order of 10^{10} to 10^{12} A/m^2 at moderate absolute current values. This is particularly critical in magnetic tunnel junctions, where excessive voltage bias across the insulating barrier can induce dielectric breakdown, compromising the integrity of the device.

1.2 Nanomagnetism

Examining nanoscale magnetic textures, such as skyrmions and vortices, demands theoretical frameworks going beyond classical macroscopic Maxwell's equations. Indeed, magnetization in ferromagnets is typically not completely uniform but separated into the so-called magnetic domains. This heterogeneity intensifies when considering nanoscale structures, as nonuniform magnetic solitons can emerge. In this Section, we start by introducing the fundamental relationships governing magnetism. We then focus on micromagnetism, which allows to study microscopic magnetic systems using the Landau-Lifshitz-Gilbert-Slonczewski equation. Subsequently, we explore magnetic vortices and present the Thiele equation approach, treating them as quasiparticles for predicting their dynamics.

To comprehend the emergence of magnetism in materials, the Hamiltonian governing the exchange interaction between neighboring spins must be considered:

$$\mathcal{H} = -\sum_{\langle i,j \rangle} J_{ij} \mathbf{S}_i \cdot \mathbf{S}_j, \tag{1.6}$$

where J_{ij} denotes the exchange integral. Its sign dictates whether a material can become ferromagnetic or antiferromagnetic, as a parallel or antiparallel alignment between adjacent spins is favored, respectively. It is important to highlight that spontaneous magnetization in ferromagnets (antiferromagnets) arises solely below the Curie temperature T_C (Néel temperature T_N). Above this temperature, thermal fluctuations dominate, disordering magnetic moments and inducing a paramagnetic behavior.

The magnetization field $\mathbf{M}$, representing the density of magnetic moments per unit volume, is linked to the magnetic induction $\mathbf{B}$ and magnetic field $\mathbf{H}$ through the fundamental equation:

$$\mathbf{B} = \mu_0(\mathbf{M} + \mathbf{H}), \tag{1.7}$$

where $\mu_0 = 4\pi \times 10^{-7}$ H/m is the vacuum permeability. In paramagnetic systems, where magnetic moments are randomly oriented in the absence of external field, a linear response is observed under weak applied field $\mathbf{H}$, yielding

$$\mathbf{B} = \mu_0(1 + \chi)\mathbf{H}, \tag{1.8}$$

where χ is the magnetic susceptibility of the material.

The relationship does not hold for ferromagnetic materials due to their highly nonlinear response $\mathbf{M}(\mathbf{H})$ and concomitant hysteresis. Upon application of a sufficiently strong field, these materials saturate at a value M_s, corresponding to a complete alignment of the magnetic moments with the external field. For $Ni_{80}Fe_{20}$ permalloy (Py), this saturation magnetization is roughly 800×10^3 A/m.

1.2.1 Micromagnetism

Micromagnetism investigates magnetic materials at the mesoscopic scale, within a continuous medium approximation, serving as an intermediary between atomic lattice quantum phenomena and macroscopic behavior, which is usually studied using Maxwell's equations. This framework, operating at a nano- to microscopic level, facilitates the examination of both the ground state and dynamics of magnetic textures through the energy functional W of the system, which includes all contributions to the magnetic energy, as described hereafter [38,39]. Typically, systems studied using micromagnetism span from a few nanometers up to several micrometers. Below this scale, the continuous medium approximation does not account for discrete atomic structures. Above it, the theory remains valid but the computational resources required for relevant results become prohibitive.

The exchange interaction between neighboring spins, a primary cause of ferromagnetism (or antiferromagnetism) in materials, yields an exchange energy:

$$W^{\mathrm{ex}} = \int_V A(\nabla \mathbf{m})^2 \mathrm{d}V, \tag{1.9}$$

where A is the exchange stiffness coefficient, and $\mathbf{m} = \mathbf{M}/M_s$ is the reduced magnetization. The magnetostatic energy, arising from the interplay between the magnetization and its demagnetizing field (or stray field), is expressed as

$$W^{\mathrm{ms}} = -\frac{\mu_0}{2} \int_V \mathbf{M} \cdot \mathbf{H}^{\mathrm{ms}} \mathrm{d}V, \tag{1.10}$$

where the demagnetizing field $\mathbf{H}^{\mathrm{ms}}$ satisfies

$$\begin{cases} \nabla \times \mathbf{H}^{\mathrm{ms}} = 0 \\ \nabla \cdot \left(\mu_0(\mathbf{M} + \mathbf{H}^{\mathrm{ms}})\right) = 0 \end{cases} . \tag{1.11}$$

In addition, the application of an external magnetic field $\mathbf{H}^{\mathrm{ext}}$ introduces a Zeeman energy contribution:

$$W^{\mathrm{Z}} = -\mu_0 \int_V \mathbf{M} \cdot \mathbf{H}^{\mathrm{ext}} \mathrm{d}V. \tag{1.12}$$

Finally, magnetocrystalline anisotropy can lead to easy magnetization axes, and contributes to the total energy through an anisotropy energy given as

$$W^{\mathrm{anis}} = \int_V K f^{\mathrm{anis}}(\mathbf{m}) \mathrm{d}V, \tag{1.13}$$

where K is an anisotropy constant and f^{anis} a function that depends on the crystal structure. Other energy contributions, such as magnetoelastic and thermal energies, or the Dzyaloshinskii-Moriya interaction, may also be relevant but are out of scope of this thesis. More specifically, certain material parameters, such as M_s and A are considered at room temperature, thus incorporating temperature effects to some degree. However, thermal noise will not be considered in our study. Additionally, the permalloy free layers considered in this thesis have thicknesses of ~ 10 nm, which allows to disregard specific interfacial anisotropy and voltage-controlled magnetic anisotropy effects [40].

The energy functional enables the computation of an effective field $\mathbf{H}^{\text{eff}}$ at any point in the material, encompassing all energy contribution affecting the magnetization [41,42]. This effective field is calculated using the functional derivative:

$$\mathbf{H}^{\text{eff}} = -\frac{1}{\mu_0 M_s}\frac{\delta W}{\delta \mathbf{m}}. \tag{1.14}$$

This effective field exerts a torque τ^{LL} on the magnetization, inducing a Larmor precession, expressed as

$$\boldsymbol{\tau}^{\text{LL}} = -\gamma_0 \mathbf{m} \times \mathbf{H}^{\text{eff}}, \tag{1.15}$$

where $\gamma_0 = \mu_0 \gamma_G$, with γ_G the gyromagnetic ratio. To account for experimental observations not rendered using solely this conservative term, like saturation in hysteresis curves, a dissipative phenomenological damping term has been introduced:

$$\boldsymbol{\tau}^{\text{G}} = \alpha_G \mathbf{m} \times \frac{\partial \mathbf{m}}{\partial t}, \tag{1.16}$$

where α_G is the Gilbert damping coefficient ($\alpha_G \ll 1$, generally). Adding these two terms gives rise to the well-known Landau-Lifshitz-Gilbert-Slonczewski (LLGS) equation [43,44], governing the magnetization dynamics:

$$\frac{\partial \mathbf{m}}{\partial t} = -\gamma_0 \mathbf{m} \times \mathbf{H}^{\text{eff}} + \alpha \mathbf{m} \times \frac{\partial \mathbf{m}}{\partial t} + \boldsymbol{\tau}^{\text{ST}}. \tag{1.17}$$

Here, $\boldsymbol{\tau}^{\text{ST}}$ represents the spin-transfer torques, studied notably by Slonczewski [33], as well as Berger [45], and Zhang & Li [46,47], which must be considered for magnetic tunnel junctions.

The LLGS equation, in its explicit form, is implement in micromagnetic solvers, like OOMMF [48] (CPU-based) and mumax^3/mumax$^+$ [8,49,50] (GPU-accelerated), enabling to study the dynamics of nano- to microscopic magnetic textures. The spatial discretization of the lattice through finite element (*e.g.*, the

Nmag software [51]) or finite difference methods must be nanometric, typically below

$$l_{\mathrm{ex}} = \sqrt{\frac{2A}{\mu_0 M_s^2}}, \tag{1.18}$$

which is the exchange length [52] of the material (roughly 5 nm for Py), to ensure physically meaningful predictions. This constraint renders micromagnetic simulations (MMS) computationally intensive, necessitating substantial resources for accurate modeling.

1.2.2 Magnetic vortices

Soft ferromagnetic nanopillars can exhibit a nonuniform magnetic ground state, known as a vortex. Such magnetic texture features in-plane spins swirling around a vortex core [53,54], minimizing magnetostatic energy by closing the magnetic flux, while increasing exchange energy due to adjacent spin noncollinearity. The vortex core, whose radius is comparable to the exchange length of the material, presents an out-of-plane magnetization, that prevents an exchange energy singularity. These solitons, of winding number $S = +1$, are characterized by two topological parameters, namely the chirality C (also called circulation, or helicity), denoting clockwise ($C = -1$) or anticlockwise ($C = +1$) in-plane magnetization curling, and polarity P, indicating upwards ($P = +1$) or downwards ($P = -1$) out-of-plane magnetization in the vortex core. Magnetic vortices thus appear in four distinct states, based on each P and C combinations, as illustrated in Figure 1.5.

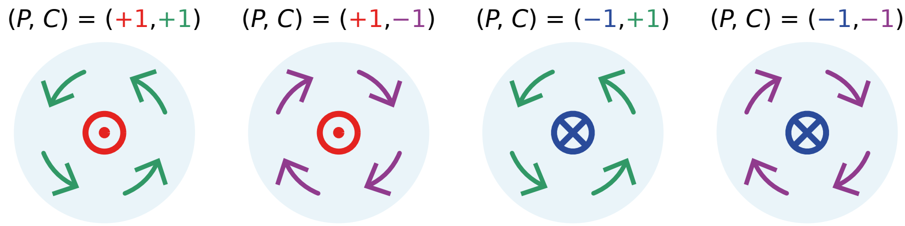

Figure 1.5: Vortex magnetic states in circular nanopillars, depending on the polarity P, upwards or downwards (in red and blue, respectively), and chirality C, clockwise or counterclockwise (in purple and green, respectively).

The aspect ratio of the pillar, *i.e.*, $\xi = h/(2R)$ with h the thickness and R the radius, governs the nucleation of a vortex as magnetic ground state. In permalloy nanomagnets, negligible magnetocrystalline anisotropy renders shape anisotropy dominant. For either flat or elongated cylinders ($h \ll R$ or $h \gg R$, respectively), magnetization aligns uniformly along the easy axis to minimize magnetostatic energy. Conversely, vortex states can be stabilized for intermediate aspect ratios. Magnetic phase diagrams, as illustrated in Figure 1.6, reveal equilibrium boundaries and stability regions of uniform and vortex states through magnetic energy calculations, simulations, and experiments [6,55,56,57]. These studies confirm uniform in-plane and out-of-plane magnetization for extreme aspect ratios, while nonuniform vortex states emerge for intermediate ξ values. For the smallest sizes, the superparamagnetic limit may be reached, wherein rapid thermally-induced magnetic switching occurs, which is exploitable for applications demanding pure random numbers [58,59]. It is noteworthy that the aspect ratio is not the only geometric parameter of importance. For instance, nanopillars with micrometer-scale radii or larger favor multidomain states, as a vortex configuration becomes increasingly costly in terms of exchange energy over a large surface area [24].

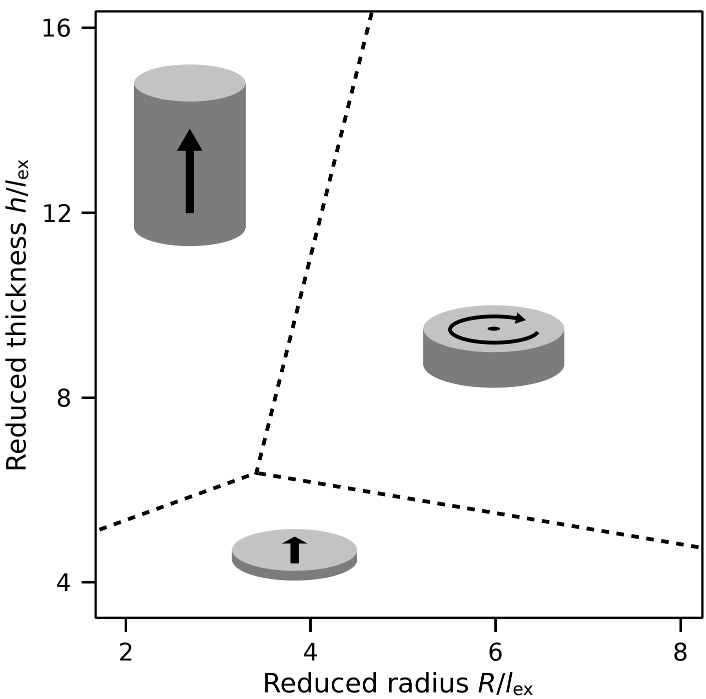

Figure 1.6: Schematic phase diagram of nanoscale permalloy cylinders as a function of their reduced radius and thickness. The various magnetization ground states are separated by dashed lines. In reality, some states can be metastable close to boundaries. Depending on the aspect ratio of the pillar, the magnetization is either uniform (in-plane or out-of-plane) or forms a vortex configuration. Inspired from Refs. [6,57].

In the Bloch sphere formalism, the three spatial components of the magnetization field **m** are defined as

$$\mathbf{m} = \begin{bmatrix} m_x \\ m_y \\ m_z \end{bmatrix} = \begin{bmatrix} \cos(\phi)\sin(\Theta) \\ \sin(\phi)\sin(\Theta) \\ \cos(\Theta) \end{bmatrix}, \tag{1.19}$$

where ϕ and Θ are functions that represent the planar and out-of-plane angles, respectively. This definition ensures that $\|\mathbf{m}\| = 1$. For a magnetic vortex, the magnetization at any point $\mathbf{r} = (r, \theta)$, in polar coordinates (or $\mathbf{r} = (x, y)$, in Cartesian coordinates), in the nanomagnet can be determined by these angles, whose value depend on the vortex core position $\mathbf{X} = (\rho, \varphi)$, or $\mathbf{X} = (X, Y)$ in Cartesian coordinates, as depicted in Figure 1.7.

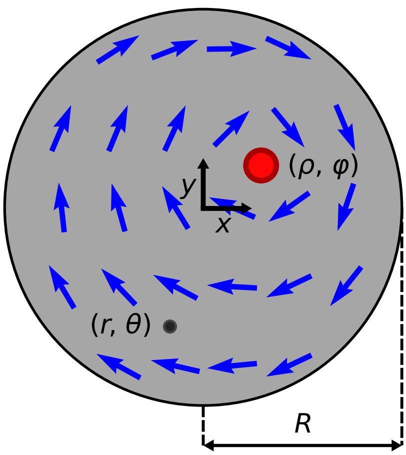

Figure 1.7: Schematic top view of a magnetic vortex. The in-plane vortex magnetization field **M** is depicted by the blue arrows. The vortex core (highlighted in red) gyrates at a position (ρ, φ), in polar coordinates. All points in the plane (in dark gray) are denoted using a vector $\mathbf{r} = (r, \theta)$.

Several theoretical frameworks describe mathematically the vortex magnetization in circular nanopillars of radius R and thickness h, particularly for off-centered vortex core. The single-vortex *Ansatz* (SVA), developed by Guslienko *et al.* [60], has been employed for stability calculations, vortex core displacement under magnetic fields, or resonant frequency calculations. This model assumes a rigid translation of the vortex from its equilibrium position, maintaining an unaltered magnetization distribution $\mathbf{m}(\mathbf{r} - \mathbf{X})$. However, this hypothesis introduces surface magnetic charges at the edge surface of the nanodot, notably limiting its applicability for large vortex core displacement.

To address this issue, the two-vortex *Ansatz* (TVA) was introduced [61]. This model combines two off-centered rigid vortices with cores located in $\mathbf{X} = (\rho, \varphi)$ and $\mathbf{X}_{\mathcal{I}} = \left(R^2/\rho, \varphi\right)$, in polar coordinates, to satisfy Dirichlet boundary conditions. Indeed, contrary to the SVA, it meets $(\mathbf{m} \cdot \mathbf{n})_S = 0$, with $\mathbf{n}$ the normal vector to the surface S, thereby eliminating surface magnetic charges. Within this framework, the planar magnetization components are described as

$$m_x^{\mathrm{TVA}} = \frac{C\left(s\left(\eta^2 \sin(2\theta - \varphi) + \sin(\varphi)\right) - \left(1 + s^2\right)\eta \sin(\theta)\right)\sin(\Theta)}{\sqrt{s^2 + \eta^2 - 2s\eta\cos(\theta - \varphi)}\sqrt{1 + s^2\eta^2 - 2s\eta\cos(\theta - \varphi)}}, \tag{1.20}$$

$$m_y^{\mathrm{TVA}} = \frac{C\left(\left(1 + s^2\right)\eta \cos(\theta) - s\left(\eta^2 \cos(2\theta - \varphi) + \cos(\varphi)\right)\right)\sin(\Theta)}{\sqrt{s^2 + \eta^2 - 2s\eta\cos(\theta - \varphi)}\sqrt{1 + s^2\eta^2 - 2s\eta\cos(\theta - \varphi)}}, \tag{1.21}$$

where s is the reduced vortex core position, defined as $s = \sqrt{X^2 + Y^2}/R = \rho/R$, with (X, Y) the Cartesian coordinates of the core, and $\eta = r/R$.

The OOP angle Θ can be determined using

$$m_z = P f_z(\|\mathbf{r} - \mathbf{X}\|), \tag{1.22}$$

where P is the vortex polarity and f_z represents the vortex core profile. Various bell-shaped curves have been proposed in previous works, as compared by Gaididei *et al.* [62]. Usov and Peschany [63] suggested a simple expression dividing the vortex into two distinct regions:

$$f_z^{\mathrm{Usov}} = \begin{cases} \frac{\rho_c^2 - (\rho^2 + r^2 - 2\rho r \cos(\theta - \varphi))}{\rho_c^2 + \rho^2 + r^2 - 2\rho r \cos(\theta - \varphi)}, & \text{for } \sqrt{\rho^2 + r^2 - 2\rho r \cos(\theta - \varphi)} < \rho_c \\ 0, & \text{for } \sqrt{\rho^2 + r^2 - 2\rho r \cos(\theta - \varphi)} > \rho_c \end{cases}, \tag{1.23}$$

with ρ_c the vortex core radius. However, thus function lacks differentiability at the domain intersection. Feldtkeller & Thomas proposed a Gaussian alternative [64], given as

$$f_z^{\mathrm{Feldt.}} = \exp\left(-\frac{\rho^2 + r^2 - 2\rho r \cos(\theta - \varphi)}{\rho_c^2}\right), \tag{1.24}$$

which resolves this issue, by proposing a simple but continuous core structure. Later, Höllinger *et al.* [65] introduced a 'Mexican Hat' *Ansatz*:

$$f_z^{\text{Höll.}} = c \exp\left(-\frac{\rho^2 + r^2 - 2\rho r \cos(\theta - \varphi)}{l_{\text{ex}}^2}\right) + (1-c) \exp\left(-\frac{\rho^2 + r^2 - 2\rho r \cos(\theta - \varphi)}{4 l_{\text{ex}}^2}\right), \tag{1.25}$$

where c is a thickness-dependent constant, which accounts for the halo effect observed in thick dots, *i.e.*, a region at the core boundary where m_z can be negative (positive) when polarity is positive (negative). These various vortex core profiles are compared in Figure 1.8.

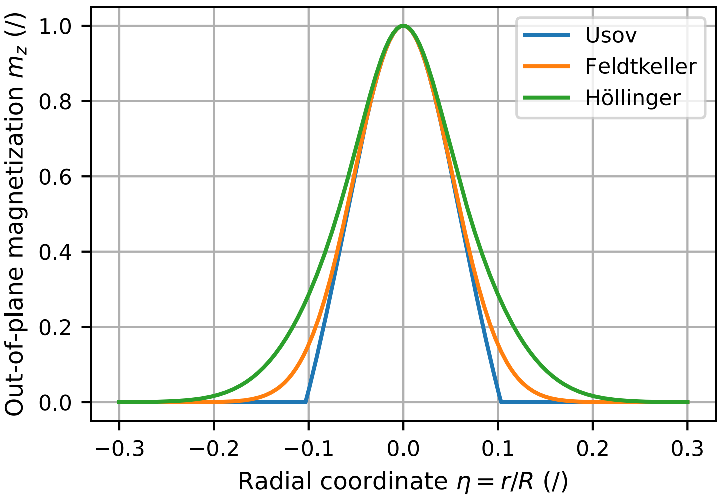

Figure 1.8: Comparison between the vortex core out-of-plane profiles from Usov [63], Feldtkeller [64], and Höllinger [65], for a $R = 100$ nm and $h = 10$ nm permalloy disk. Inspired from Ref. [62].

1.2.3 Thiele equation approach

The Thiele equation approach, originally derived from the LLGS formalism to analyze domain wall motion [9,10], is commonly employed to model vortex dynamics within MTJ free layers. This theoretical framework, first adapted to vortices by Huber [66] after works on bubble materials by Malozemoff & Slonczewski [67], treats the vortex core as a quasiparticle accounting for any modification of the global magnetization field. Interestingly, the Thiele equation approach can also be applied to other magnetic solitons, *e.g.*, skyrmions and hopfions. This model considers a net sum of forces acting on the vortex core to predict its in-plane position $\mathbf{X} = (X, Y)$, *i.e.*, the collective coordinates. At equilibrium, the most general description of this system is

$$\bar{\bar{\mathbf{M}}} \cdot \ddot{\mathbf{X}} + \bar{\bar{\mathbf{G}}} \cdot \dot{\mathbf{X}} - \frac{\partial W}{\partial \mathbf{X}} = \mathbf{F}^{\text{ext}} - \bar{\bar{\mathbf{D}}} \cdot \dot{\mathbf{X}}, \tag{1.26}$$

where $\bar{\bar{\mathbf{M}}} \cdot \ddot{\mathbf{X}}$ is an inertial mass term, $\bar{\bar{\mathbf{G}}} \cdot \dot{\mathbf{X}}$ the gyrotropic force relative to the vortex low-frequency excitation mode (comparable to a Magnus-like force in fluid dynamics [68]), $-\partial W/\partial \mathbf{X}$ the restoring forces, $\mathbf{F}^{\text{ext}}$ any external force acting on the system, and $-\bar{\bar{\mathbf{D}}} \cdot \dot{\mathbf{X}}$ a Gilbert dissipation term. Equation (1.26) is derived by assuming a rigid translation of the initial magnetization, *i.e.*, $\mathbf{m}(\mathbf{r}, t) = \mathbf{m}_0(\mathbf{r} - \mathbf{X})$. Following the chain rule, we obtain $\partial \mathbf{m}/\partial t = -\dot{\mathbf{X}} \cdot \nabla \mathbf{m}_0$, which, after substitution into the LLGS equation and developements, leads to the various Thiele equation terms [9]. To incorporate a mass term or any higher-order contributions, deformations of the magnetization with respect to the velocity and its derivatives must also be taken into account.

It should be noted that $\bar{\bar{\mathbf{M}}}$, $\bar{\bar{\mathbf{G}}}$, and $\bar{\bar{\mathbf{D}}}$ are tensor quantities whose components can be derived from the magnetization field $\mathbf{m}$. While extensive literature exists on the vortex mass [69,70,71,72,73,74,75,76,77], it will be disregarded in this thesis as it is considered negligible for thin free layers [78]. As for the gyrotropic and damping tensors, they can be calculated as follows [79,80]:

$$G_{\alpha\beta} = \frac{M_s}{\gamma_G} \int_V \left(\left(\frac{\partial \mathbf{m}}{\partial X_\alpha} \times \frac{\partial \mathbf{m}}{\partial X_\beta} \right) \cdot \mathbf{m} \right) \mathrm{d}V, \tag{1.27}$$

$$D_{\alpha\beta} = -\alpha_G \frac{M_S}{\gamma_G} \int_V \left(\frac{\partial \mathbf{m}}{\partial X_\alpha} \cdot \frac{\partial \mathbf{m}}{\partial X_\beta} \right) \mathrm{d}V, \tag{1.28}$$

with γ_G the gyromagnetic ratio and α_G the Gilbert damping constant. Considering a magnetic vortex hosted in a nanodisk, the gyrotropic and damping tensors are in fact anti-diagonal and diagonal, respectively [66]. Consequently, these terms can be simplified to a gyrovector $G\left(\mathbf{e}_z \times \dot{\mathbf{X}}\right)$, where $G = G_{YX}$ denotes the gyroconstant, and a damping vector $D\dot{\mathbf{X}}$, with $D = D_{XX}$ representing the damping parameter (if small nondiagonal terms are negligible [80]). For an isolated spin-torque vortex oscillator, Equation (1.26) therefore simplifies to

$$G\left(\mathbf{e}_z \times \dot{\mathbf{X}}\right) - \frac{\partial W}{\partial \mathbf{X}} = \mathbf{F}^{\text{ST}} - D\dot{\mathbf{X}}, \tag{1.29}$$

where the external forces acting on the system $\mathbf{F}^{\text{ext}} = \mathbf{F}^{\text{ST}}$ are only related to the spin-transfer in this case. Such steady-state equilibrium of forces is depicted in Figure 1.9, leading to a circular vortex core trajectory.

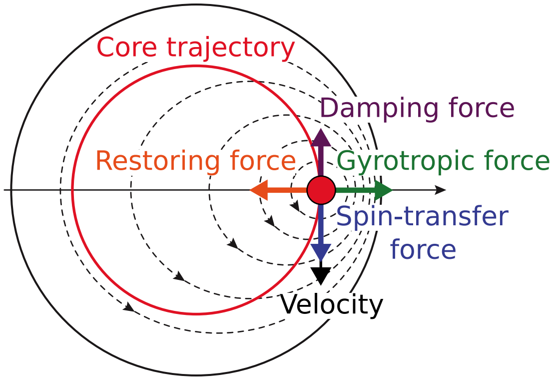

Figure 1.9: Schematic of the different forces having an effect on the vortex core. Reproduced from Dussaux *et al.* [81], with permission from *Springer Nature*.

Using the mathematical *Ansätze* of the magnetization field, presented in Section 1.2.2, as well as the aforementioned equations, expressions for each term of Equation (1.29) have been derived in past decades. However, analytical developments have proved to be cumbersome, due to the complexity of the involved expressions, necessitating approximations and simplifications. Consequently, the terms presented hereafter, originally developed for resonant regime calculations, are mainly valid for small core displacements, and typically considered idependent of the vortex core position.

The gyroconstant is given by

$$G = -2\pi P h \frac{M_s}{\gamma_G}, \tag{1.30}$$

where h is the free layer thickness [61,66]. Similarly, the Gilbert damping term can be calculated, yielding

$$D = -\alpha_G \eta \, |G|, \tag{1.31}$$

where η is a geometry-dependent parameter that takes various formulations across existing literature. For instance, some studies employ [82,83]

$$\eta = \frac{1}{2} \ln\left(\frac{R}{\rho_c}\right) + 1, \tag{1.32}$$

with ρ_c the core radius, while others [84,85] use

$$\eta = \frac{1}{2}\ln\left(\frac{R}{2l_{\mathrm{ex}}}\right) + \frac{3}{8}. \tag{1.33}$$

Several alternative expressions are also reported [86,87].

The restoring forces can be obtained through an analogy with a simple harmonic oscillator, characterized by an effective stiffness constant k, related to the vortex core displacement $\mathbf{X}$, which modifies the energy landscape:

$$-\frac{\partial W}{\partial \mathbf{X}} = -k\mathbf{X}. \tag{1.34}$$

Using the expressions for the energy contributions given in Section 1.2.1, stiffness constants associated to each magnetic energy component can be derived. For permalloy nanodisks, magnetocrystalline and magnetoelastic contributions are negligible, leaving predominantly exchange and magnetostatic interactions to consider, if thermal effects are disregarded.

Under the single-vortex *Ansatz*, Guslienko *et al.* [5] determined the exchange stiffness as

$$k_{\mathrm{SVA}}^{\mathrm{ex}} = -\pi\mu_0 M_s^2 h\left(\frac{l_{\mathrm{ex}}}{R}\right)^2 \frac{1}{1-s^2}, \tag{1.35}$$

with s representing the reduced vortex core position. Alternatively, Gaididei *et al.* derived [62], employing the two-vortex *Ansatz*,

$$k_{\mathrm{TVA}}^{\mathrm{ex}} = 2\pi\mu_0 M_s^2 h\left(\frac{l_{\mathrm{ex}}}{R}\right)^2 \frac{1}{1-s^2}, \tag{1.36}$$

noting a (−2) factor between the two results. This suprising change of sign likely arises from the image vortex introduced within TVA. In the thin-film limit ($\xi = 0$), the magnetostatic contribution [88], which dominates the exchange term, is expressed as

$$k^{\mathrm{ms}} = \frac{10}{9}\mu_0 M_s^2 \frac{h^2}{R}. \tag{1.37}$$

The expressions of k^{ex} and k^{ms} indicate that the confinement weakens for larger radii.

Lastly, spin-transfer torques, originating from diverse physical phenomena in MTJs, need to be considered. These forces can be decomposed into three components:

$$\mathbf{F}^{\mathrm{ST}} = \mathbf{F}_{\perp}^{\mathrm{ST}} + \mathbf{F}_{\parallel}^{\mathrm{ST}} + \mathbf{F}_{\mathrm{FLT}}^{\mathrm{ST}}, \tag{1.38}$$

where $\mathbf{F}_{\perp}^{\mathrm{ST}}$ and $\mathbf{F}_{\parallel}^{\mathrm{ST}}$ are the perpendicular and parallel Slonczewski torque contributions [33], respectively, and $\mathbf{F}_{\mathrm{FLT}}^{\mathrm{ST}}$ is the field-like torque [46]. All terms depend on the polarizer orientation $\mathbf{p} = \left(p_x, p_y, p_z\right)$, and may vanish in specific polarization configurations. The first term is expressed as

$$\mathbf{F}_{\perp}^{\mathrm{ST}} = \kappa_{\perp}^{\mathrm{ST}} J(\mathbf{e}_z \times \mathbf{X}), \tag{1.39}$$

where J is the OOP current density, and the parameter $\kappa_{\perp}^{\mathrm{ST}}$ is given as

$$\kappa_{\perp}^{\mathrm{ST}} = \pi a_J M_{\mathrm{s}} h p_z, \tag{1.40}$$

with $a_J = p_J \hbar / \left(2|e| M_{\mathrm{s}}^{\mathrm{ref}} h\right)$, where p_J is the polarization efficiency and $M_{\mathrm{s}}^{\mathrm{ref}}$ the saturation magnetization of the polarizer [79,84]. The in-plane component of the Slonczewski torque can be expressed as

$$\mathbf{F}_{\parallel}^{\mathrm{ST}} = \ln(2) \pi M_{\mathrm{s}} h \rho_{\mathrm{c}} C a_J J \mathbf{p}_{x,y}, \tag{1.41}$$

where $\mathbf{p}_{x,y}$ are the in-plane components of the polarization unit vector [86,89]. Finally, the field-like torque is given by

$$\mathbf{F}_{\mathrm{FLT}}^{\mathrm{ST}} = \kappa_{\mathrm{FLT}}^{\mathrm{ST}} (\mathbf{e}_z \times \mathbf{p}), \tag{1.42}$$

where the parameter $\kappa_{\mathrm{FLT}}^{\mathrm{ST}}$ is

$$\kappa_{\mathrm{FLT}}^{\mathrm{ST}} = -\frac{2}{3} C \pi M_{\mathrm{s}} h R a_J J \xi_{\mathrm{FLT}}, \tag{1.43}$$

with ξ_{FLT} its relative efficiency with respect to the Slonczewski torque [86]. In MTJs, the field-like torque arises from electron spins precessing during tunneling and acquiring phase shifts, which leads to interference effects that produce a net torque [90]. The latter acts perpendicular to the magnetization and to the other torque component, similar to an effective magnetic field, hence its name.

Additionally, external magnetic fields may also influence magnetic vortex dynamics through the Zeeman energy, inducing magnetization deformation dependent on their orientation relative to the disk. These fields may originate from experimental setups and other magnetic layers, or be current-induced.

On the one hand, uniform in-plane fields have been extensively studied [5,61,91,92], as they facilitate vortex core excitation in nano-oscillators and modulate resonant frequencies, or for field sensing applications. Applying an in-plane field favors parallel magnetization, while disadvantaging antiparallel components. It results in a displacement of the vortex core perpendicular to the field direction on a side that depends on the chirality, as illustrated in Figure 1.10.

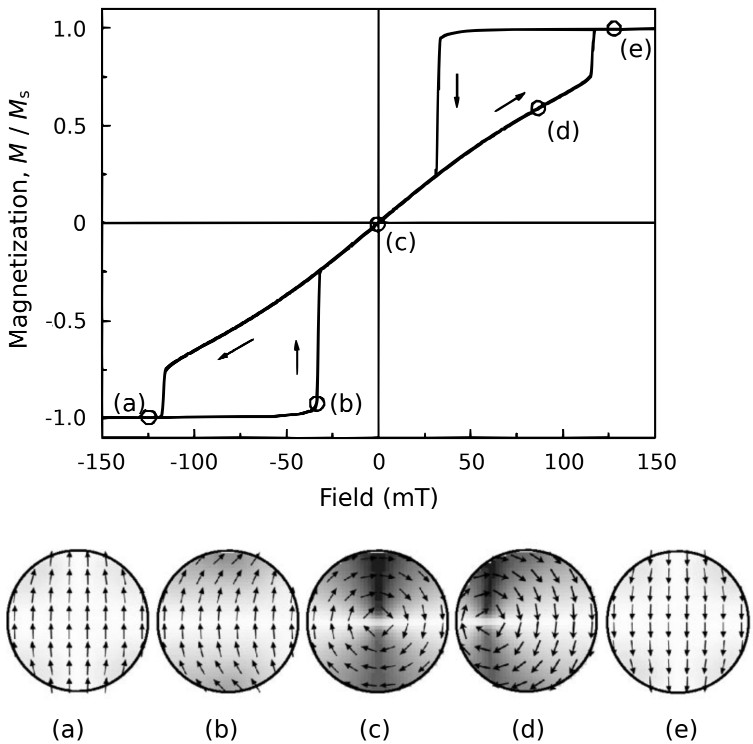

Figure 1.10: The typical hysteresis loop and magnetization reversal process due to the vortex nucleation displacement, and annihilation as calculated with micro-magnetic solver for an isolated dot with R = 100 nm and h = 30 nm. Reproduced from Guslienko *et al.* [91], with permission of the *American Physical Society*.

Near saturation, a critical annihilation field is reached, collapsing the vortex into an in-plane state aligned with the field. Reducing the magnetic field from saturation reveals a sudden jump in the hysteresis curve, marking a vortex nucleation. At rest, *i.e.*, in the remanent state, the average magnetization $\langle \mathbf{m}(\mathbf{r}) \rangle_V = -2/3C(\mathbf{e}_z \times \mathbf{X})/R$ is zero by symmetry [82], the vortex core resting at the center of the nanodot. The impact of an in-plane field can be incorporated into the Thiele equation through a Zeeman energy-derived force [82], given as

$$\mathbf{F}^{\mathrm{Z}} = \mu(\mathbf{e}_z \times \mathbf{H}), \tag{1.44}$$

with $\mu = 2\pi/3\mu_0 ChM_s R$ and $\mathbf{H} = \left(H_x, H_y\right)$ the in-plane magnetic field.

On the other hand, out-of-plane fields are frequently employed in experiments to facilitate gyrotropic excitation of the vortex core, notably by tilting the polarizer [81]. These bias fields indirectly influence the dynamics by expanding the core diameter and increasing m_z uniformly [93,94], offset by H_z/H_s with H_z the applied OOP field and H_s the saturation field. As the magnetization norm must be conserved, the in-plane components $\left(m_x, m_y\right)$ adjust consequently. This impacts the Thiele equation terms, necessitating modifications for accurate modeling [86,89]. Notably, de Loubens *et al.* [95] showed that the gyrotropic frequency scales with $(1 + PH_z/H_s)$, with P the polarity, under OOP magnetic fields.

Finally, magnetic fields may also be generated by a current [96], as in spin-torque vortex oscillators. When an OOP current traverses a nanopillar, it induces a magnetic field following Ampère's law:

$$\oint_{\mathcal{C}} \mathbf{B} \cdot \mathrm{d}\mathbf{l} = \mu_0 \mathcal{I}_{\mathcal{C}}, \tag{1.45}$$

where $\mathcal{I}_{\mathcal{C}}$ is the current enclosed by a closed curve $\mathcal{C}$. Assuming a uniform current density $J = \mathcal{I}/\left(\pi R^2\right)$, as well as an infinitely long, circular cylinder, it yields

$$\left\| \mathbf{B}^{\mathrm{Oe}}(r) \right\| = \begin{cases} \frac{\mu_0}{2} J r, & \text{for } r \leq R \text{ (inside the pillar)}, \\ \frac{\mu_0}{2} J \frac{R^2}{r}, & \text{for } r > R \text{ (outside the pillar)}. \end{cases} \tag{1.46}$$

The swirling Ampère-Oersted field influences vortex stability, upon its relative orientation with the in-plane magnetization [97]. Moreover, it enables deterministic chirality setting during vortex nucleation, through minimization of the

Zeeman energy [98]. Within the Thiele framework, this field contributes to the restoring forces [84,99,100], similarly the other energy components. Its associated stiffness constant is given as [79]

$$k^{\mathrm{Oe}} = CJ\kappa^{\mathrm{Oe}} = CJ\frac{8\pi}{30}\mu_0 M_s hR. \tag{1.47}$$

In a steady-state system, Equation (1.29) and Figure 1.9 reveal two distinct collinear force equilibria, as the gyroforce is counterbalanced by restoring forces, while the spin-transfer forces compensate for damping. This dual equilibrium between conservative and dissipative forces enables deducing key vortex properties, such as the resonant frequency or the critical current required to trigger sustained auto-oscillations. Indeed, assuming a circular trajectory, $G\left(\mathbf{e}_z \times \dot{\mathbf{X}}\right) = -G\omega\mathbf{X}$, with ω the angular frequency, since $\dot{\mathbf{X}} = \omega\mathbf{e}_z \times \mathbf{X}$ [61]. The resonant frequency can thus be calculated using

$$\omega_0 = -\frac{k}{G}, \tag{1.48}$$

where k is the total vortex stiffness, combining every energy contributions. This yields eigenfrequency values in the hundreds-of-MHz range, corresponding to the microwave spectrum, and up to GHz for the smallest oscillators.

In the context of magnetic vortices within the free layer of MTJs, a critical current density J_{c1} can be defined, representing the threshold at which sustained auto-oscillations are initiated, surpassing Gilbert damping. Neglecting the exchange energy and considering a perpendicular polarizer, J_{c1} is governed by the following relationship [100]:

$$J_{c1} = \frac{-Dk^{\mathrm{ms}}}{DC\kappa^{\mathrm{Oe}} + G\kappa_{\perp}^{\mathrm{ST}}}. \tag{1.49}$$

For an applied current density exceeding J_{c1}, the vortex core exhibits a circular trajectory around the geometric center, with a steady-state orbital radius $s(J)$ scaling as

$$s(J) = \lambda\sqrt{\frac{J}{J_{c1}} - 1}, \tag{1.50}$$

where λ is a material and geometry dependent parameter [79]. Analogously, a second critical current density J_{c2} marks the operational limit of such oscillators. Beyond this value, two scenarii may arise [79]. Either the vortex core attains a critical velocity, triggering an instability that may invert its polarity, or the core collapses on the edges of the nanodisk and annihilates. These mechanisms are discussed in Chapters 2 & 3.

The physical origins underlying polarity reversals, specifically involving the annihilation of vortex-antivortex pairs, will be detailed in Section 3.2. However, it is worth noting that various means can be employed to control core reversals, such as spin-polarized currents or magnetic fields [7,18,89]. Mastering these reversals, along with those of chirality, is of obvious interest for data storage applications using magnetic vortices.

1.3 Spin-torque nano-oscillators

Following preliminary investigations into magnetization switching using spin-transfer torque, particularly relevant for magnetic data storage applications, the exploration rapidly extended to other scenarii, going beyond simple binary parallel-antiparallel states. This included cases where the magnetization of the free layer could undergo sustained precessions, as spin-torque (or spin-transfer) nano-oscillators (STNOs) emerged. These nanoscale devices, engineered to convert direct currents into oscillating voltages, are the focus of this Section. Initially, their fundamental operating principle will be eplained. Then, one of their most prominent prospective applications, neuromorphic spintronics, will be examined.

Before that, it is important to note that STNOs belong to the broad category of nonlinear oscillating systems, which extends far beyond magnetism. Those may thus exhibit phenomena common to this class of dynamics, such as bifurcation behavior, chaos, synchronization, or steady-state auto-oscillations. In this context, Slavin & Tiberkevich developed a model based on spin-wave theory to describe STNO dynamics [14]. This model allows the characterization of spintronic oscillators using parameters closer to experiments compared to micromagnetism, such as the output power. In general, these auto-oscillators share certain fundamental aspects, *i.e.*, resonance behavior, natural losses through dissipations, and an active element that acts as anti-damping to counteract them. The general equation describing their dynamics is

$$\dot{c} + c\big(i\omega(p) + \Gamma_+(p) - \Gamma_-(p)\big) = f(t), \tag{1.51}$$

where c represents the complex oscillation amplitude, ω is the resonance frequency, $p = |c|^2$ is the power, Γ_+ and Γ_- are the damping and anti-damping rates, respectively, and $f(t)$ accounts for any interaction with the environment. The p-dependence of the parameters clearly underlines the nonlinear dynamics. Additionnaly, the form of this equation resembles that of the LLGS equation, suggesting that this theoretical framework can be applied to various types of spintronic oscillators, regardless of the physical origin driving the anti-damping effect. Examples, besides uniform and vortex-based spin-torque oscillators, include spin-Hall [101] or spin-orbit nano-oscillators [102].

1.3.1 Nanoscale transducers

Spin-torque nano-oscillators [13,103,104] exploit both spin-transfer torque and magnetoresistance phenomena, detailed in Section 1.1. Similarly to magnetic storage devices, their architecture is made of a fixed magnetic layer, a nonmagnetic spacer, and a free layer. However, STNOs are engineered to facilitate wider phase space exploration by the free layer magnetization, diverging from the bistable configuration of memory devices obtained using magnetic anisotropies. The operating principle of STNOs is detailed in Figure 1.11.

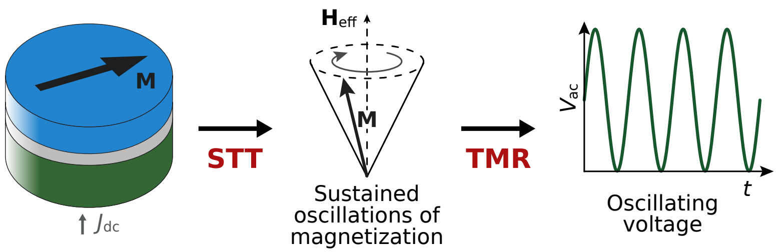

Figure 1.11: Operation principle of a spin-torque nano-oscillator, consisting of a polarizer (in green), an oxide barrier (in gray), and a free magnetic layer (in blue). Upon injecting an out-of-plane current into the stack, spin-polarized electrons from the fixed ferromagnetic layer induce sustained magnetization precessions in the free layer, transduced into an oscillating voltage through magnetoresistance effects.

Upon current injection, electrons are spin-polarized by the fixed layer and transferred to the free layer. Providing a sufficiently large current, sustained magnetization oscillations can be induced by spin-transfer torque. Through magnetoresistive effects, these oscillations translate into ac voltage output when a dc current is applied, rendering STNOs nanoscale nonlinear dc-to-ac converters, which are CMOS compatible. Typically operating in the microwave range, STNOs yield GHz frequencies, with output powers of up to µW for injected currents of the order of the mA, using MTJs [105].

As established in Section 1.2.2, magnetic vortices can emerge as the ground state of ferromagnetic nanopillars, for specific geometric and material parameters. For a given range of STNO free layer thickness and radius, the magnetization adopts therefore a nonuniform vortex state, giving rise to spin-torque vortex oscillators (STVOs) [16]. Upon injecting a spin-polarized current, the vortex core initiates gyrotropic precessions, inducing oscillations in the mean magnetization of the free layer. These oscillations, analogous to uniformly magnetized STNOs, manifest at lower frequency (< 1 GHz), corresponding to the gyrotropic mode, as illustrated in Figure 1.12. However, STVOs exhibit notable advantages over uniform STNOs, including narrower linewidth and lower noise sensitivity [81,87].

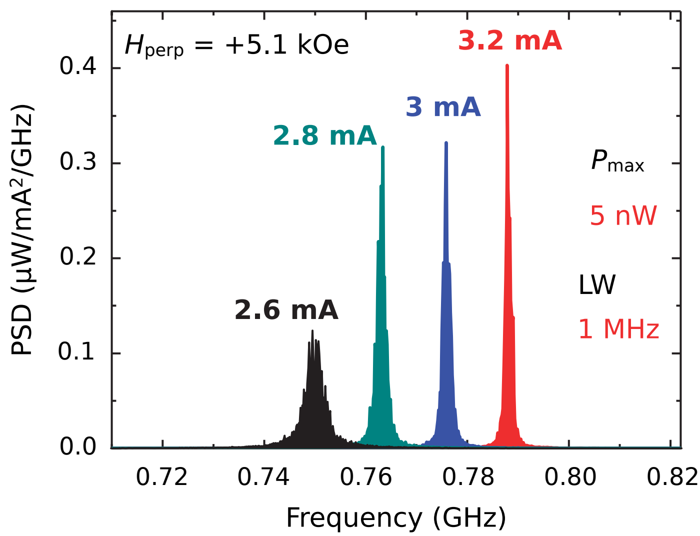

Figure 1.12: Large microwave emission spectra associated with vortex oscillations. Power spectral densities (PSD) normalized by I_{dc}^2, obtained for I_{dc} = 2.6, 2.8, 3, and 3.2 mA with H_{perp} = 5.1 kOe. Reproduced from Dussaux *et al.* [81], with permission from *Springer Nature*.

It seems crucial to point out that the observable parameters in experiments and simulations are not directly equivalent, particularly for electrical measurements. Experimentally, an oscillating electrical signal is obtained, which depends on the evolution of the device resistance. In contrast, simulations and theoretical models focus on the magnetization field and the position of the vortex core.

While there is a clear relationship between the magnetic state in the free layer and the TMR signal, no quantitative equation has yet been established to link the core position with magnetoresistance.

Two distinct configurations enable STVO realization, nanocontacts [106,107] and nanopillars [15,81]. Nanocontacts are attractive for their relatively simple fabrication process, involving straightforward layer deposition and localized electrical contact using a microscopic tip or an etched hole, yielding locally high current density. Vortex stabilization is achieved through the Ampère-Oersted field, with core oscillations that are induced if a sufficient current density is generated. Conversely, nanopillars, illustrated in Figure 1.13, provide a superior control at the expense of difficult fabrication, requiring circular pillar definition using etching techniques followed by a SiO_2 passivation step. Using this configuration, the current stays within the magnetic tunnel junction, while a spatially-confined vortex can be stabilized as the free layer magnetic ground state. This thesis focuses exclusively on STVOs in nanopillar structures.

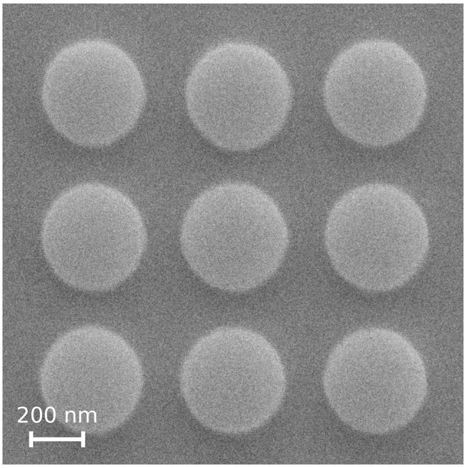

Figure 1.13: Scanning electron microscope (10 kV, 7.5 µm aperture) of a dense 3×3 array of spin-torque vortex oscillators (top view), with a radius of 200 nm and separated by about 100 nm. Image courtesy of Dr. Tristan da Câmara Santa Clara Gomes (INESC-MN, Portugal).

It is noteworthy that STNOs (and STVOs) can also rectify injected microwave signals into dc voltage [108]. The output of the resulting spin-diode effect, analogous to classical electronic diodes, depends on the input signal frequency, external parameters like an applied magnetic field or bias current, and the device resonant frequency. This phenomenon holds promise for frequency detection

[18] and ambient energy harvesting applications [109], though efficiency remains limited.

Up to this point, we have described our MTJ as having a three-layer structure. In reality, the stacks used consist of a much larger number of layers, each serving a specific purpose. For instance, our partners at INL (Braga, Portugal) have produced stacks with the following specifications (thicknesses in nanometers) [110]: Ta(5)/CuN(50)/Ta(5)/CuN(50)/Ta(5)/Ru(5)/IrMn(6)/$Co_{70}Fe_{30}$(2)/Ru (0.7)/$Co_{40}Fe_{40}B_{20}$(2.6)/MgO/$Co_{40}Fe_{40}B_{20}$(2)/Ta(0.2)/NiFe(7)/Ta(10)/Ru(7). In practice, we will only simulate the free layer with mumax^3, *i.e.*, the CoFeB/Ta/NiFe part, which we approximate as a single homogeneous permalloy layer. Consequently, certain fabrication defects or effects of each individual layer will be partly neglected in our micromagnetic simulations, due to constraints on cell size or practical considerations.

1.3.2 Neuromorphic spintronics

Magnetic vortices, and by extension STVOs, have rapidly gained attention for prospective applications due to their wide array of features. Initially, they were investigated as promising candidates for nanoscale data storage using their various stable magnetic states [7]. Subsequently, their microwave properties were studied to develop electrically-tunable devices capable of generating or capturing rf signals [16]. More recently, they have attracted significant interest in the quickly emerging field of hardware-based artificial intelligence due to their nonlinear behavior, which can be harnessed as an activation function for artifical neurons [111], as explored hereafter.

Cognitive task resolution stands as a prominently explored application for STNOs. With the surging popularity of artifical neural networks (ANNs), their associated energy consumption has become a critical concern. A potential alternative to conventional CMOS architectures lies in neuromorphic computing, which proposes to go beyond the von Neumann bottleneck, which limits efficiency due to memory-CPU data transfer, by mimicking some of the human brain working principles. This paradigm enables the integration of low-power hardware devices within physical ANNs to emulate neuronal and synaptic functions at reduced energy costs. To fulfill such neural tasks, these devices must ideally satisfy stringent criteria, such as nanoscale dimensions, CMOS compatibility, intrinsic memory, and above all nonlinearity [111]. Several spintronic devices meet all these requirements. Within the neuromorphic framework, Grollier's group pioneering works demonstrated the first successful execution of cognitive tasks using STNOs [19,20], nearly a decade ago.

In this context, reservoir computing, which is a type of recurrent neural network with fixed and random weights (illustrated in Figure 1.14), has received significant interest for spintronic applications due to its simplified training step, which solely adjusts the ouput layer weights [112]. However, its inferior performance compared to other architectures led to explore alternative approaches more recently. In fact, numerous research efforts have focused on neuromorphic sprintronic systems employing diverse devices for both synaptic and neuronal emulation, including oscillator-based networks [113,114], or other quasiparticles like magnons [115,116] and skyrmions [117,118].

Despite the promising results achieved with reservoir computing and other ANN architectures, their operating principles diverge quite significantly from that of the human brain. A fundamental framework emulating biological neurons is the leaky integrate-and-fire (LIF) model, depicted in Figure 1.15, which has been successfully implemented using spintronics [111,119].

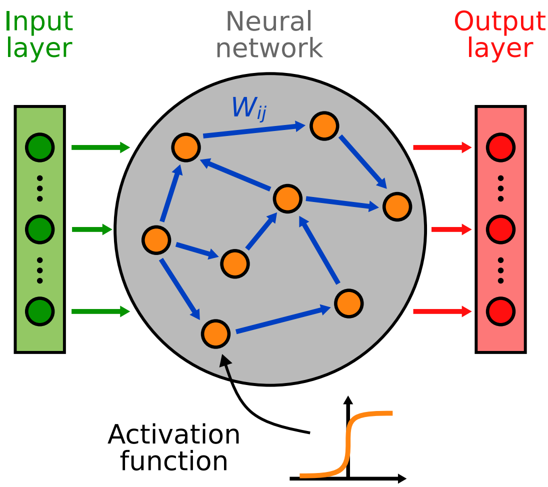

Figure 1.14: Schematic of a reservoir computing neural network. Input data is injected into a network with random and fixed weights, only the output layer wieghts being trained. Each neuron applies a nonlinear activation function, potentially provided by spintronic device dynamics.

In this model, spiking signals from adjacent neurons are combined through a weighted sum operation at the synaptic level. The neuron subsequently integrates these signals over time, while exhibiting passive decay in the absence of stimulation. Upon sufficient temporal proximity of input signals, a potential threshold is reached, triggering a spike emission. Post-firing event, the neuron undergoes a reset to its resting state, waiting for further excitation inputs.

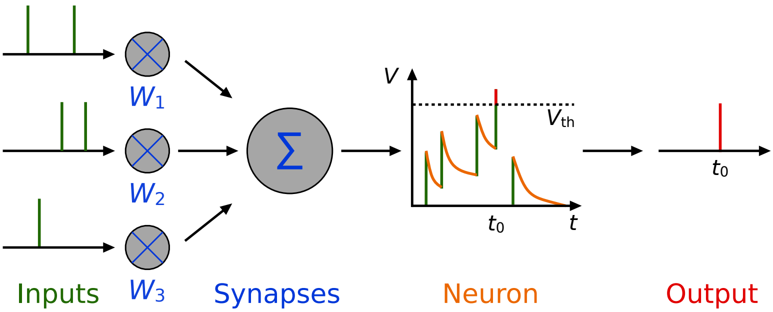

Figure 1.15: Leaky integrate-and-fire model, emulating biological neurons. Input signals undergo a weighted sum operation (with corresponding weights W_i) at the synapses and integration by the neuron, which leaks without stimulations. A threshold V_{th} crossing triggers a firing event, where an output spike is emitted and followed by neuronal reset.

Chapter's take-home message

- The advent of **spintronics** has made it possible to **exploit the electron spin** in addition to its charge. In particular, **magnetic tunnel junctions** (MTJ) feature **large magnetoresistance** values, making them attractive for a wide range of applications.
- At small scales, magnetism can behave differently than for bulk materials. For example, in **magnetic nanopillars**, a **vortex state** can be stabilized as the **ground state**, as it helps reducing the magnetostatic energy.
- Using a **MTJ with a free layer in a vortex state**, it is possible to retrieve an **rf voltage by injecting a dc current** into it, thanks to the spin-transfer torque that causes **gyrotropic oscillations** of the vortex core.
- **Spin-torque vortex oscillators** (STVOs) offer a number of **advantages**, such as their emitted power and CMOS compatibility. One of the most valuable is their **nonlinearity**, which can be exploited for **neuromorphic computing**.
- Either the **Thiele equation approach** or **micromagnetic simulations** are available to study those devices theoretically. However, each of these methods **presents limitations**, whether in terms of **accuracy** of their predictions, or the significant **computational resources** required to carry them out, respectively.

2

Magnetic energy in spin-torque vortex oscillators

As discussed in Chapter 1, we have seen that it is possible to control the dynamics of magnetic structures by imposing a spin-polarized current through them, among other means. However, many studies on spin-torque vortex oscillators (STVOs) neglect the impact of the Ampère-Oersted field (AOF) induced by this same current (dc and/or ac) [62,85,120,121,122]. In addition, it has also been shown that the AOF influences clearly the magnetization dynamics in nanopillars [123], as well as the spin-wave dynamics in spin-torque oscillators [124]. Therefore, the present Chapter aims at demonstrating that this Zeeman contribution is not negligible and, most importantly, not avoidable by any means as it originates from the injected current responsible for the oscillatory excitation, as far as STVOs are concerned.

In Section 2.1, we propose potential improvements to existing analytical models of vortex dynamics based on the Thiele equation approach (TEA), extending their validity over a wider range of currents and taking into account the AOF. However, we will see that these developments are not sufficient to obtain a quantitative model rendering properly the full vortex dynamics. We then attempt to understand the origin of the discrepancies observed between analytics and simulations in Section 2.2, to eventually propose an alternative method to purely analytical calculations to derive the energy terms. The results and figures presented in this Chapter are adapted from two of our recent papers, published in *Scientific Reports* [125] and *Physical Review B* [126]. These works were carried out within the Neuromorphic Engineering Group at UCLouvain, in particular through joint efforts with Dr. Chloé Chopin and Prof. Flavio Abreu Araujo.

2.1 Ampère-Oersted field splitting of the dynamics

Two improvements to the commonly used Thiele equation approach are considered and validated through micromagnetic simulations. The first one is related to the magnetostatic contribution to the vortex energy, as described by Gaididei *et al.* [62]. Indeed, as this energy component is highly dependent on the nanodot aspect ratio $\xi = h/(2R)$, with h the thickness of the free layer and R its radius, a significant correction of this contribution when ξ is different from zero has to be considered. The second contribution we bring to the TEA is an analytical description of the AOF contribution to the potential energy, which has been already considered by Khvalkovskiy *et al.* [84] and Dussaux *et al.* [86]. The latter studies report this contribution for limited displacements of the vortex core reduced position $s = \|\mathbf{X}\|/R = \sqrt{X^2 + Y^2}/R$, *i.e.*, $0 < s < 0.1$. The version we propose is accurate for the whole range of validity of vortex core positions in the considered circular dot, *i.e.*, $0 < s < 0.8$. It is noteworthy that the analytical AOF model presented hereafter has already been successfully used in a previous study by Abreu Araujo & Grollier [127]. We will see that, for the specific geometry considered in our study, the vortex core is expelled from the magnetic dot for $s > 0.8$. Such value corresponds to the position at which the vortex core reaches the edge of the nanodot. In other cases, the vortex reaches a critical velocity inducing a polarity switch and damps back to the dot center. Sometimes, when the vortex core is expelled, a dynamic C-state may also be stabilized, giving rise to sustained oscillations, as shown by Wittrock *et al.* [128].

2.1.1 Methods

Micromagnetic simulations including the Ampère-Oersted field $\mathbf{H}^{\mathrm{Oe}}$ are performed using the GPU-based solver mumax^3 [8]. A trilayer nanopillar presenting a free layer of radius $R = 100$ nm and thickness $h = 10$ nm is studied (see Figure 2.1). The spacer is a tunnel barrier, typically MgO, and the polarizer, usually clamped by a synthetic antiferromagnet (SAF), presents a perpendicular direction of magnetization $\mathbf{p} = \left(p_x, p_y, p_z\right) = (0, 0, 1)$. Typical permalloy material parameters are used for the free layer [24,129,130]. The saturation magnetization and exchange stiffness coefficient are $M_s = 800 \times 10^3$ A/m and $A = 1.07 \times 10^{-11}$ J/m, respectively. The Gilbert damping constant α_G is fixed at 0.01 and the spin-current polarization p_J at 0.2. The magnetic dot is discretized into cells of dimensions $2.5 \times 2.5 \times 5$ nm^3. This ensures that the micromagnetic cells are smaller than the characteristic exchange length $l_{ex} = \sqrt{2A/(\mu_0 M_s^2)}$ of permalloy (about 5 nm). The dc current density injected into the MTJ under study ranges from 0 to 10×10^{10} A/m^2, in the positive z-direction. Mumax^3 includes both Slonczewski [33] and Zhang-Li [47] spin-transfer torques. Nonetheless, given the out-of-plane current configuration, the Zhang-Li torque has a limited influence on the dynamics as the vortex profile is uniform along the free layer for thin magnetic dots [78]. In light of these considerations, we have chosen to simplify the analysis by assuming an adiabatic situation, where the degree of nonadiabaticity is fixed at zero.

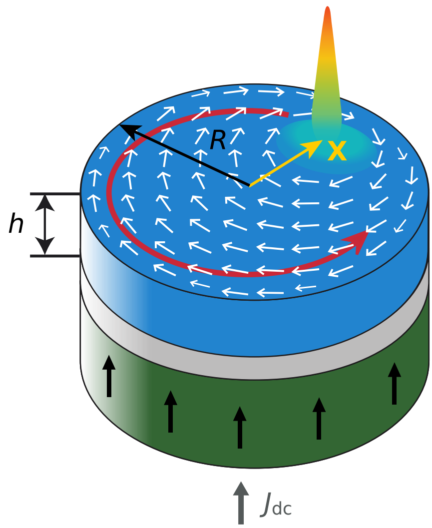

Figure 2.1: Schematic of the magnetic tunnel junction (MTJ) under study. The MTJ is a standard Py/MgO/SAF stack (in blue, gray, and green, respectively) with a permalloy (Py) free layer of radius R and thickness h, a nonmagnetic spacer (typically MgO), and a synthetic antiferromagnet (SAF) polarizer that generates a perpendicular spin polarization p_J. The in-plane components of the vortex magnetization field **m** are represented by the white arrows. The precessional gyration of the vortex core, located at **X**, is depicted by the red arrow. The color gradient represents the magnitude of the out-of-plane magnetization m_z. For clarity, the depicted core polarity is positive here, while it is $P = -1$ in our study.

The vortex core position is initially off-centered and is internally computed when the simulation is running by mumax^3, while the frequency is extracted with a very accurate technique called *simple numerical instantaneous frequency approximation* (SNIFA [131]) developed for that purpose. The micromagnetic simulations are performed for a sufficient duration (> 1 µs) to avoid considering the transient regime. To minimize computation time while ensuring a final steady-state, we initialize the vortex close to its final position for each specific current density at the beginning of the simulations. Moreover, the current-induced AOF is added to mumax^3 as an external field as there is no built-in implementation. To evaluate this field, we consider an ideal situation where the current density is uniform across the pillar. Furthermore, as the thickness of the free layer is considerably smaller than the overall thickness of the pillar, edge effects are considered negligible, *i.e.*, an infinite cylinder is assumed. Finally, no bias magnetic field is applied and the influence of temperature is not taken into account in this study ($T = 0$ K). More precisely, thermal noise is excluded from this study, though certain material parameters (*e.g.*, M_s or A) are provided at room temperature. Additionally, part of the phenomenological Gilbert damping is due to magnon-phonon interactions.

Three different configurations are investigated (see Figure 2.2) in order to quantify the impact of the AOF on the vortex dynamics, for a polarity $P = -1$:
1. without considering the Ampère-Oersted field ($\mathbf{H}^{\mathrm{Oe}}$) contribution,
2. with $\mathbf{H}^{\mathrm{Oe}}$ parallel to the curling in-plane magnetization, *i.e.*, $C = +1$,
3. with $\mathbf{H}^{\mathrm{Oe}}$ antiparallel to the curling in-plane magnetization, *i.e.*, $C = -1$.

Those are labeled below as noOe, C^+, and C^-, respectively.

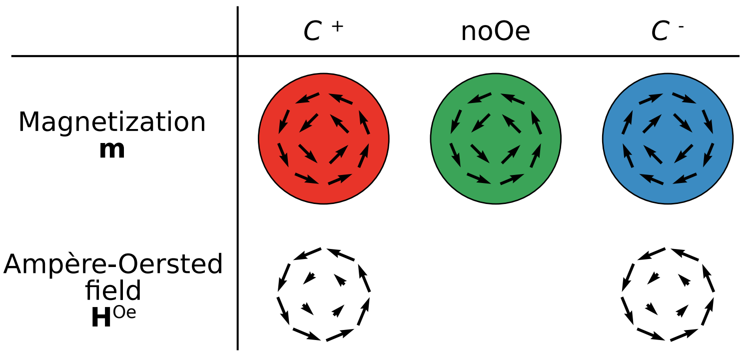

Figure 2.2: Relative orientation between the vortex in-plane magnetization $\mathbf{m}$ and the Ampère-Oersted field (AOF) $\mathbf{H}^{\mathrm{Oe}}$ in the three investigated configurations (*i.e.*, C^+, noOe, and C^-, in red, green, and blue, respectively). Considering an out-of-plane positive current, the curling magnetization is parallel (antiparallel) to the AOF if the chirality is positive (negative). For noOe, the AOF is not taken into account. Adapted from Ref. [126].

2.1.2 A spin-torque-driven harmonic oscillator

In order to understand analytically the STVO dynamics, the Thiele equation approach is used. As introduced in Chapter 1, the STVO dynamics, where the vortex core is reduced to a quasiparticle located at an in-plane position $\mathbf{X} = (X, Y)$, can be described within this framework by

$$G\left(\mathbf{e}_z \times \dot{\mathbf{X}}\right) + D\dot{\mathbf{X}} = \frac{\partial W}{\partial \mathbf{X}} + \mathbf{F}^{\mathrm{ST}}, \tag{2.1}$$

where $G = -2\pi P M_s h/\gamma_G$ [61,88], with $\gamma_G = g|e|/(2m_e)$ the gyromagnetic ratio with g the electron g-factor and m_e the electron mass, $D = -\alpha_G \eta |G|$ with $\eta = \frac{1}{2}\ln(R/(2l_{\mathrm{ex}})) + \frac{3}{8}$ [84], and $W = W^{\mathrm{ex}} + W^{\mathrm{ms}} + W^{\mathrm{Oe}}$ which are the three main contributions to the energy, if magnetocrystalline anisotropy is neglected. As introduced in Chapter 1, the restoring forces are expressed using their springlike restoring force parameters

$$\frac{\partial\left(W^{\mathrm{ex}} + W^{\mathrm{Oe}} + W^{\mathrm{ms}}\right)}{\partial \mathbf{X}} = \left(k^{\mathrm{ex}} + CJ\kappa^{\mathrm{Oe}} + k^{\mathrm{ms}}\right)\mathbf{X}. \tag{2.2}$$

As stated, three energy contributions are taken into account. The first expression is related to the exchange energy, as proposed by Gaididei *et al.* [62], based on developments from Guslienko *et al.* [5],

$$k^{\mathrm{ex}} = 2\pi\mu_0 M_s^2 h\left(\frac{l_{\mathrm{ex}}}{R}\right)^2 \frac{1}{1-s^2}. \tag{2.3}$$

Subsequently, we have calculated the Zeeman contribution $k^{\mathrm{Oe}} = CJ\kappa^{\mathrm{Oe}}$, related to the Ampère-Oersted field [127], under the two-vortex *Ansatz*. It is expressed as (see Supplementary Materials of Ref. [125] for details)

$$\kappa^{\mathrm{Oe}} = \frac{8\pi}{30}\mu_0 M_s h R\left(1 - \frac{4}{7}s^2 - \frac{1}{7}s^4 - \frac{16}{231}s^6 - \frac{125}{3003}s^8\right). \tag{2.4}$$

Finally, to enhance the precision of the model, a last contribution is considered. Indeed, a correction to the magnetostatic W^{ms} component has to be made. The latter has been calculated by Gaididei *et al.* [62] under the two-vortex *Ansatz*, giving $W^{\mathrm{ms}}(\xi, s) = \mu_0 M_s^2 h^2 R s^2 \Omega(\xi, s)$, which is the magnetostatic energy for a given aspect ratio ξ and reduced vortex core position s. An analytical solution exists [62] for the multiple integral $\Omega(\xi, s)$, but only when $\xi = 0$ and $s = 0$. In this study the aspect ratio ξ is 0.05, thus, a different method is used instead (again, see Supplementary Materials of Ref. [125] for details). Let us note that this method is applicable to any ξ, including $\xi = 0$. First, a nondeterministic Monte-Carlo integration technique is used to obtain numerically values of $W^{\mathrm{ms}}(\xi, s) \equiv W_\xi^{\mathrm{ms}}(s)$, for a given ξ and for s ranging between 0 and 1. Then, $W_\xi^{\mathrm{ms}}(s)$ is fitted with a polynomial and the resulting expression is derived, following Equation (2.2). As a result, the contribution of the magnetostatic energy for a given aspect ratio ξ can be modeled as

$$k_\xi^{\mathrm{ms}} = 2\mu_0 M_s^2 \frac{h^2}{R} \Lambda_{0,\xi}\left(1 + a_\xi s^2 + b_\xi s^4 + c_\xi s^6\right). \tag{2.5}$$

For $\xi = 0.05$, the coefficients $\Lambda_{0,\xi}$, a_ξ, b_ξ, and c_ξ are 0.507, 0.175, 0.065, and -0.054. For $\xi = 0$, $\Lambda_{0,\xi} = 0.555$ which is in good agreement with the analytical result by Guslienko *et al.* [88], with $2\mu_0\Lambda_{0,\xi=0} \approx \frac{10}{9}\mu_0$ (difference of less than 0.2%). To simplify the notations, k_ξ^{ms} is replaced by k^{ms} for the rest of this Chapter.

Finally, the spin-transfer forces are composed of different terms: $\mathbf{F}^{\mathrm{ST}} = \mathbf{F}_\perp^{\mathrm{ST}} + \mathbf{F}_\parallel^{\mathrm{ST}} + \mathbf{F}_{\mathrm{FLT}}^{\mathrm{ST}}$. The first two contributions are the perpendicular and parallel Slonczewski spin-torques [33,86], respectively, while the third one is the field-like torque (FLT) [46]. For the sake of clarity, a perpendicular polarizer is considered in this study, *i.e.*, $\mathbf{p} = (0, 0, 1)$, as already investigated by Ivanov & Zaspel [132] within TEA. So, $\mathbf{F}_\parallel^{\mathrm{ST}}$, proportional to $\mathbf{p}_{x,y} = (0, 0)$ in this case [86], and $\mathbf{F}_{\mathrm{FLT}}^{\mathrm{ST}} = \kappa_{\mathrm{FLT}}^{\mathrm{ST}} J\left(\mathbf{e}_z \times \mathbf{p}\right)$ are both equal to zero, and only $\mathbf{F}_\perp^{\mathrm{ST}}$ contributes to the dynamics. $\mathbf{F}_\perp^{\mathrm{ST}} = \kappa_\perp^{\mathrm{ST}} J\left(\mathbf{e}_z \times \mathbf{X}\right)$, where $\kappa_\perp^{\mathrm{ST}} = \pi a_J M_s h p_z$, with $a_J = p_J \hbar / \left(2|e| M_s^{\mathrm{ref}} h\right)$ [84], with $M_s^{\mathrm{ref}} = 800 \times 10^3$ A/m.

From Equation (2.1), STVO dynamics can be easily simplified as [100]

$$\begin{bmatrix} D & -G \\ G & D \end{bmatrix} \begin{bmatrix} \dot{X} \\ \dot{Y} \end{bmatrix} = \begin{bmatrix} k & -\kappa^{\mathrm{ST}} J \\ \kappa^{\mathrm{ST}} J & k \end{bmatrix} \begin{bmatrix} X \\ Y \end{bmatrix}, \tag{2.6}$$

where $k = k^{\mathrm{ex}} + CJ\kappa^{\mathrm{Oe}} + k^{\mathrm{ms}}$. This equation can be reduced to a homogeneous system of linear first-order differential equations:

$$\begin{bmatrix} \dot{X} \\ \dot{Y} \end{bmatrix} = \underbrace{\begin{bmatrix} \Gamma & -\omega \\ \omega & \Gamma \end{bmatrix}}_{\bar{\bar{\Omega}}} \begin{bmatrix} X \\ Y \end{bmatrix}, \tag{2.7}$$

where the parameters ω and Γ are given as follows

$$\omega = \frac{DJ\kappa^{\mathrm{ST}} - G\left(k^{\mathrm{ex}} + CJ\kappa^{\mathrm{Oe}} + k^{\mathrm{ms}}\right)}{D^2 + G^2}, \tag{2.8}$$

$$\Gamma = \frac{D\left(k^{\mathrm{ex}} + CJ\kappa^{\mathrm{Oe}} + k^{\mathrm{ms}}\right) + GJ\kappa^{\mathrm{ST}}}{D^2 + G^2}. \tag{2.9}$$

These developments show that the dynamics of our STVO are described by the simple harmonic oscillator equation $\dot{\mathbf{X}} = \bar{\bar{\mathbf{\Omega}}}\mathbf{X}$. More specifically, our system is equivalent to a harmonic oscillator driven by spin-transfer torque and damped by Gilbert phenomena. Considering $\Gamma \to 0$ and ω as being constant, one can prove (see Appendix A for details) that a valid solution to this system is

$$\begin{bmatrix} X(t) \\ Y(t) \end{bmatrix} = \|\mathbf{X}\|\, e^{\Gamma t} \begin{bmatrix} \sin(\omega t) \\ -\cos(\omega t) \end{bmatrix}, \tag{2.10}$$

which describes a spiral trajectory. We should highlight that, in general, Γ and ω are not constant in time, but in the steady-state oscillating regime they effectively are. We will show hereafter that important properties of the STVO dynamics can be derived from this regime of oscillations.

From the first parameter, *i.e.*, ω, it is straightforward to identify the vortex gyrotropic frequency of oscillations as $f^{\mathrm{STVO}}(J) = \omega(J)/(2\pi)$. Qualitatively, Equation (2.8) thus supports the fact that larger vortices, being less confined and thus less stiff, oscillate at lower frequencies. Furthermore, the $CJ\kappa^{\mathrm{Oe}}$ term indicates that the AOF introduces a linear current density dependence to the frequency, at least within the resonant regime. Meanwhile the second parameter, *i.e.*, Γ, is responsible for the transient regime. When $\Gamma < 0$, the transient dynamics is in the damping regime leading to $s = 0$, which gives rise to a resonant regime. When $\Gamma > 0$, the transient dynamics is in the driving regime ($s > 0$), which leads to the steady-state oscillating regime where $\Gamma = 0$ and s becomes constant. The first critical current J_{c1} can therefore be analytically defined as the limit when $\Gamma = 0$ and $s = 0$. Mathematically, this condition translates to

$$\Gamma(s=0) = \frac{D\left(k_0^{\mathrm{ex}} + CJ_{c1}\kappa_0^{\mathrm{Oe}} + k_0^{\mathrm{ms}}\right) + GJ_{c1}\kappa_\perp^{\mathrm{ST}}}{D^2 + G^2} = 0. \tag{2.11}$$

After simplifications, the critical current is therefore given as

$$J_{c1} = \frac{-D\left(k_0^{\mathrm{ex}} + k_0^{\mathrm{ms}}\right)}{DC\kappa_0^{\mathrm{Oe}} + G\kappa_\perp^{\mathrm{ST}}}, \tag{2.12}$$

which implies that smaller-radius STVOs thus necessitate a larger current density to enter the auto-oscillating regime. Additionally, the critical current is expected to vary based on the configuration, because of the $DC\kappa_0^{\mathrm{Oe}}$ term. A vortex with an in-plane magnetization aligned parallel to the AOF should exhibit greater stability, resulting on a larger critical current density.

The corrections to several terms of the TEA we brought here allow having a model valid for s up to 0.8, which is the limit of the vortex existence. As previously mentioned, for $s > 0.8$ the vortex becomes unstable and switches polarity in the present case, *i.e.*, for an aspect ratio $\xi = 0.05$. As the vortex core position depends on the current density J imposed, one can define a second critical current J_{c2} above which the vortex core polarity switches. Once the vortex switches polarity, the model accurately describes the STVO dynamics, providing the opposite polarity (damping regime). As a consequence, the critical current J_{c2} establishes the limit between the steady-state oscillating regime and the second resonant regime, due to the core polarity reversal.

To summarize, two resonant regimes ($s = 0$) exist and one steady-state regime, which is characterized by in-plane oscillations of the vortex core ($s > 0$). To be in the steady-state regime, two conditions need to be fulfilled:

$$\begin{cases} JPp_z < 0, \\ \pm\left|J_{c1}\right| \lesseqgtr \pm|J| \lesseqgtr \pm\left|J_{c2}\right|. \end{cases} \tag{2.13}$$

For both resonant regimes, at least one of these conditions is not satisfied. The existence of the second critical current J_{c2} originates from the fact that when $\pm|J| \lesseqgtr \pm\left|J_{c2}\right|$, then $s > 0.8$ and the vortex core switches polarity, meaning that the first condition is not fulfilled anymore. Improvement for the other terms of the TEA (s-dependence of G and D for instance) will be considered in Chapter 3.

2.1.3 Chirality-dependent frequency splitting

The critical current and vortex gyrotropic frequency given by the analytical model and micromagnetic simulations are compared. The critical current J_{c1} is extracted from the micromagnetic simulations by the following method. First, the reduced vortex core position s is plotted as a function of the current density J (see Figure 2.3). Then, the points for which $0 \leq s \leq 0.8$ (*i.e.*, when steady-state is reached and before crossing the limit of vortex stability) are fitted after performing an interpolation which increases the fit accuracy. The fitting function used is $s(J) = \left(a_0 + a_1 J + a_2 J^2\right)\sqrt{J/J_{c1} - 1}$ (see Figure 2.3). This function has no direct physical origin, but its form is based on the square-root expression proposed by Guslienko *et al.* [79] and captures a typical bifurcation behavior of the dynamics.

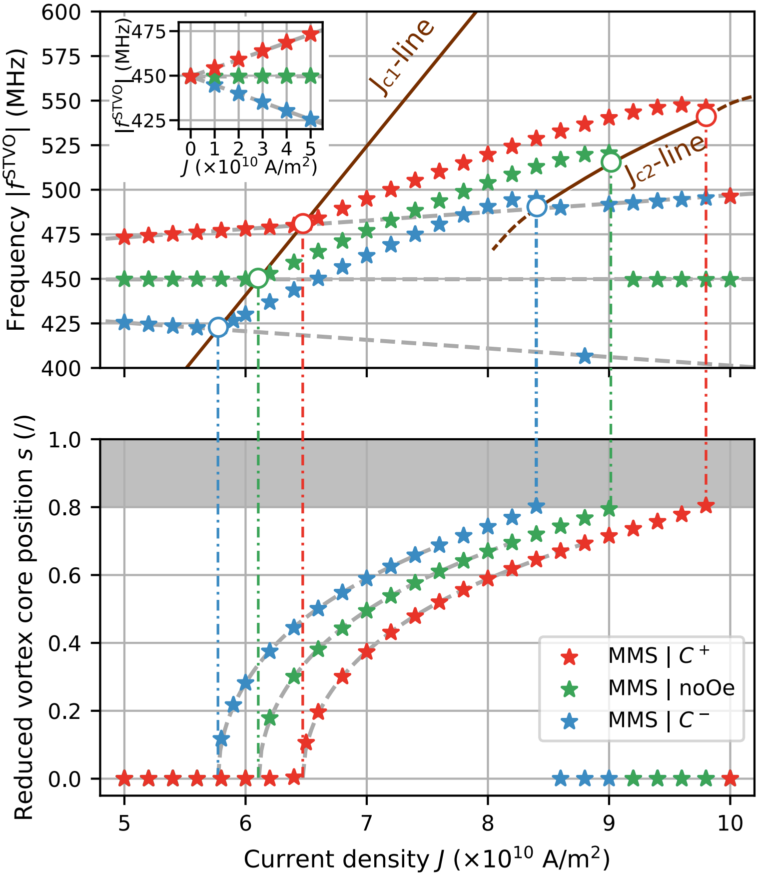

Figure 2.3: Vortex dynamical properties *versus* the dc current excitation. (top) The absolute value of the vortex gyrotropic frequency $\left|f^{STVO}\right|$ and (bottom) the reduced vortex core position s as a function of the dc current density J. The frequency is fitted with a linear function of J in the first resonant regime ($J < J_{c1}$), for each configuration (gray dashed lines). The critical current J_{c1} is extracted from $s(J)$, which gives rise to the brown J_{c1}-line. The latter represents the transition between the first resonant regime and the steady-state oscillating regime. The J_{c1}-line links the $f^{STVO}(J_{c1})$ points originating from the MMS data and is well approximated by the analytical counterpart $f^{STVO} = J\kappa_{\perp}^{ST}/(2\pi D)$. The J_{c1} and J_{c2} values are plotted across both subfigures by corresponding dashed-dotted line. The J_{c2}-line represents the transition from the steady-state oscillating regime to the second resonant regime, as for $J > J_{c2}$ the vortex polarity switches from $P = -1$ to $P = 1$ and JPp_z becomes positive. Adapted from Ref. [125].

The critical current J_{c1} is the value of the fit for $s = 0$ and is strongly impacted by the Ampère-Oersted field. Indeed, J_{c1} depends on the chirality, as previously shown by Dussaux *et al.* [86], and one can observe that $J_{c1}^{C^-} < J_{c1}^{noOe} < J_{c1}^{C^+}$. The critical current J_{c1}, for both chiralities, is close to the values determined by the TEA, as shown in Table 2.1. The ratio between the critical currents J_{c1} and J_{c2} is about 1.5, as also reported by Guslienko *et al.* [80] and detailed in Table 2.1.

The splitting caused by the AOF can be clearly seen in Figure 2.3, as it has a strong impact on s, J_{c1}, J_{c2}, and f^{STVO}, depending on the vortex chirality. In addition, one can see that on the right of the J_{c2}-line, *i.e.*, for $s > 0.8$, the vortex polarity is reversed. At this orbit, given our geometric parameters, the vortex core reaches the edge of the free layer and collapses onto it, triggering a polarity switch. For larger diameters, this limit should increase since the vortex core occupies a relatively smaller area within the nanodot, as its size is nearly independent of the diameter. The chirality of the vortex, initially at C^-, also switches for all points, except for $J = 8.8 \times 10^{10}$ A/m^2 (see Figure 2.3). Indeed, the AOF favours energetically the chirality leading to an in-plane magnetization parallel to $\mathbf{H}^{Oe}$, *i.e.*, the C^+ chirality in our case. Consequently, beyond J_{c2}, we observe a resonant vortex with a chirality value that minimizes Zeeman energy.

	C^+	noOe	C^-
J_{c1}^{TEA} $\left(\times 10^{10}\text{A/m}^2\right)$	7.40	6.94	6.54
J_{c1}^{MMS} $\left(\times 10^{10}\text{A/m}^2\right)$	6.47	6.11	5.77
J_{c2}^{MMS} $\left(\times 10^{10}\text{A/m}^2\right)$	9.83	9.10	8.43
$J_{c2}^{MMS}/J_{c1}^{MMS}$ (/)	1.52	1.50	1.46

Table 2.1: Comparison of J_{c1} given by Equation (2.12) under TEA and J_{c2} with micromagnetic simulations (MMS) after fitting the J-dependence of s (see Figure 2.3) for the different relative orientations between the AOF and the in-plane vortex magnetization.

To simplify the expression of ω given by Equation (2.8), one can consider that $D \ll G$ and the resonant regime ($J < J_{c1}$), leading to $s = 0$. In this case, ω can be simplified to $\omega \approx -\left(k^{ex} + CJ\kappa^{Oe} + k^{ms}\right)/G$. In this regime, k^{ex}, κ^{Oe}, k^{ms}, and G can all be considered as constant and G can be rewritten as $G = -P|G|$, as all components of G are positive excepted P, which can be either $+1$ or -1. The angular frequency can then be approximated by the following linear equation: $\omega = P\left(2\pi\alpha_J J + \omega_0\right)$, with $2\pi\alpha_J = C\kappa_0^{Oe}/|G|$. As ω_0 is positive because $k_0^{ex} > 0$ and

$k_0^{ms} > 0$, for $\omega_0 \gg |2\pi\alpha_J J|$ the sign of ω is given by the sign of $P\omega_0$, and thus by P. In other words, the polarity P determines the vortex core rotational direction.

From Figure 2.3, $f_0 = \omega_0/(2\pi)$ and α_J are extracted with a linear fit and the results are given in Table 2.2. The frequency $f_0 = \left(k_0^{ex} + k_0^{ms}\right)/(2\pi|G|)$ is comparable for the three configurations, as anticipated because it does not depend on κ_0^{Oe}. Furthermore, the sign of the slope $\alpha_J = C\kappa_0^{Oe}/(2\pi|G|)$ depends on the chirality ($C = \pm 1$) and is close to zero without AOF [99], as expected from the analytical model. These results show the importance of the AOF that must be taken into account to precisely render the STVO dynamics, in the resonant regime as well as in the steady-state regime (here by applying a dc out-of-plane current). In addition, the impact of the AOF on the dynamics depends on the nanopillar properties, including both material and geometry.

	C^+		noOe		C^-	
	TEA	MMS	TEA	MMS	TEA	MMS
f_0 (MHz)	529.90	449.57	529.90	449.51	529.90	449.56
α_J $\left(\text{MHz}/(\text{A/cm}^2)\right)$	4.69	4.74	0	0.03	−4.69	−4.82

Table 2.2: Comparison of f_0 and α_J between the TEA and the linear fit ($|f| = f_0 + \alpha_J J$) obtained from micromagnetic simulations (MMS).

The injected dc current density responsible for the steady-state oscillations and $s > 0$ should be seen as a way to act on and modify the vortex core position. However, the intrinsic properties of the STVO dynamics are rather given by the gyrotropic frequency *versus* the reduced vortex core position s, as shown in Figure 2.4, where only the data from the steady-state oscillating are considered. Indeed, the gyrotropic frequency depends only on s for each configuration as it modifies to total magnetic energy W of the nanodot. In the present study, s depends on J but there are other possible means for modifying the vortex core position, *e.g.* in-plane and out-of-plane field, ac current, and stray field antenna. The splitting is due to the fact that the energy W varies with chirality changes, as shown in Equation (2.2), providing that the dc current direction is kept constant (with the adequate sign to obtain steady-state regime). As illustrated in Figure 2.2, the curling AOF is counterclockwise when $J > 0$, following the right-hand rule.

Figure 2.4 shows the relationship between the reduced vortex core position s and the frequency in the steady-state oscillating regime, extracted from MMS. The latter increases with s, as seen in the study by Dussaux *et al.* [86]. Depending on the applied current, one can tune the frequency on a range of roughly 75 MHz, for each configuration. A maximum appears just before the vortex polarity reversal, happening at $s \approx 0.8$. A clear splitting due to the AOF is exhibited. Its magnitude, evaluated with $\left|f_{C^+} - f_{C^-}\right|$, decreases slightly for increasing s.

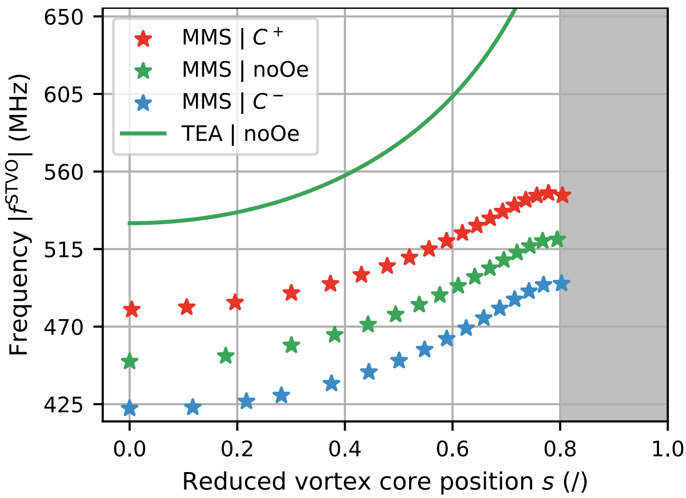

Figure 2.4: Spin-torque vortex oscillator intrinsic property. The gyrotropic frequency $\left|f^{\mathrm{STVO}}\right|$ as a function of the vortex core position s. Only steady-state oscillating regime data from MMS are shown here. An analytical prediction is also given, based on Equation (2.8). Adapted from Ref. [125].

For comparison, we include the analytical prediction for the noOe configuration, using Equation (2.8). As mentioned previously, the resonant regime is satisfactorily described by the improved analytical model. However, the steady-state state oscillating regime, shown in Figure 2.4, is at this stage only qualitatively rendered. As observed, the TEA model consistently overestimates $\left|f^{\mathrm{STVO}}\right|$ across all positions and exhibits asymptotic behavior for large s, due to the exchange stiffness expression. Further work on the s-dependence of the G and D terms and the stiffness is thus needed. As a conclusion, Figure 2.4 shows that, for a given energy configuration of such STVOs where the chirality $C = \pm 1$ is a key parameter, micromagnetic simulations show that the frequency is intrinsically dependent on the vortex core position. The same applies to the resonant regime.

2.2 Quantitative description of the magnetic energy

Despite the improvements brought in Section 2.1 to the Thiele equation approach model, its predictions still lack sufficient quality to claim its quantitative nature. Several plausible reasons may explain the differences between simulations and analytics, including the assumptions made during calculations. In this Section, our efforts are focused on the precise description of the magnetic vortex stiffness, related to the derivative of the energy functional. In particular, the stiffness parameters related to a modification of the magnetic energy terms are investigated. A method is proposed to extract exchange, magnetostatic, and Zeeman stiffness expressions from micromagnetic simulations. These expressions are then compared to the analytical derivations presented in Section 2.1. Furthermore, it is shown that the stiffness parameters depend not only on the vortex core position, but also on the injected current density. This phenomenon is not predicted by commonly used analytical *Ansätze*. We show that these findings result from a deformation of the theoretical magnetic texture caused by the Ampère-Oersted field.

2.2.1 Methods

Any displacement of the vortex core from its original ground state is associated with a modification of the potential magnetic energy W. By analogy to simple harmonic motion, we have seen that one can define a stiffness k related to the system. Keeping all generality, this springlike parameter is actually not constant, but depends on the degree of deformation, *i.e.*, the vortex core position here. Its value allows to calculate the restoring forces acting on the vortex core as

$$\mathbf{F}^{\mathrm{R}} = -\frac{\partial W}{\partial \mathbf{X}} = -k\mathbf{X}. \tag{2.14}$$

If, as in Section 2.1, we neglect magnetocrystalline anisotropy and any external magnetic field, the magnetic potential energy W is composed of the three same terms, namely, the exchange W^{ex}, magnetostatic W^{ms}, and Zeeman W^{Z} (= W^{Oe}) energies, the latter being only associated to the current-induced Ampère-Oersted field (AOF). Based on these hypotheses, the total energy W can be calculated as [62,91]

$$W = \int_V \left[A(\nabla \mathbf{m})^2 - \frac{\mu_0}{2}\mathbf{M}\cdot\mathbf{H}^{\mathrm{ms}} - \mu_0 \mathbf{M}\cdot\mathbf{H}^{\mathrm{Oe}} \right] \mathrm{d}V. \tag{2.15}$$

Using the two-vortex *Ansatz* and Equation (2.15), we have seen in Chapter 1 and Section 2.1 that various developments have been undertaken in the past two decades to obtain expressions of the stiffness parameters k^{ex}, k^{ms}, and κ^{Oe}, related to each energy component, as a function of the reduced orbit radius $s = \|\mathbf{X}\|/R$. In addition to these analytical works, micromagnetic simulations have been extensively used to investigate STVO dynamics. However, despite the fact that the Thiele equation approach derives from the Landau-Lifshitz-Gilbert-Slonczewski formalism, the latter relies on the use of an effective field rather than springlike constants to compute the magnetization evolution in time. Consequently, there is no direct access to stiffness parameters from micromagnetism. However, as the orbit radius s and the energy components are retrievable from most solvers, these parameters can still be calculated by following the procedure described below. As a first step, the energy must be fitted to a chosen expression, as a function of the vortex core position. Then, these functions must be derived according to Equation (2.14) to find the corresponding stiffness parameter. This strategy has already successfully been applied in previous studies [93,99,133], although for a limited s-range.

To carry out the micromagnetic simulations and facilitate comparison, the identical material and geometrical parameters as in Section 2.1 are employed. The only difference are the currents injected into the magnetic tunnel junction. Here, current densities of 2, 4, and 6×10^{10} A/m^2 are imposed into the oscillator, in the positive z-direction, which allows to fulfill one of the two necessary conditions for steady-state precessions, *i.e.*, $JPp_z < 0$. The second criterion is to inject a current exceeding the first critical current density J_{c1}. When $J < J_{c1}$, simulations are initialized with a vortex core translated to $s = 0.9$, which damps back to the center of the dot, *i.e.*, $s = 0$. For $J > J_{c1}$, however, two simulations are required to explore the whole range of s for a given current, as the steady-state orbit is different from zero. Each time, a first simulation is started at $s = 10^{-4}$ and a second one at $s = 0.9$. Both are stopped when the steady-state is reached. This yields $W(t)$ and a transient $s(t)$ across a broad dynamic range, allowing us to retrieve the different energy components as functions of the core position $W(s)$.

It should be noted that the vortex is not at equilibrium at the beginning of the simulations, and that the data acquisition takes place while the vortex core relaxes towards its steady-state position, determined by the value of the imposed current. This allows to capture the stiffness over the entire s-range, for any J. In addition, the three configurations studied in Section 2.1 are again investigated (see Figure 2.2), depending on the relative orientation between the in-plane curling magnetization and the AOF. A first set of simulations is performed without considering $\mathbf{H}^{\mathrm{Oe}}$, then a set with $\mathbf{H}^{\mathrm{Oe}}$ parallel to the curling magnetization, *i.e.*, $C = +1$, and, finally, a set with $\mathbf{H}^{\mathrm{Oe}}$ antiparallel to the curling magnetization, *i.e.*, $C = -1$. The vortex core position s as well as the energy components W^{ex}, W^{ms}, and W^{Oe} are internally computed by mumax^3 between each time step.

The arbitrarily chosen functions for fitting the energy components are even-power polynomials of the 10$^{\mathrm{th}}$-order, preceded by a prefactor that depends on material and geometrical parameters. They have the following form:

$$W^{\mathrm{ex}} = -\pi h A \sum_{i=0}^{5} a_i^{\mathrm{ex}} s^{2i}, \tag{2.16}$$

$$W^{\mathrm{ms}} = \mu_0 M_s^2 h^2 R \sum_{i=0}^{5} a_i^{\mathrm{ms}} s^{2i}, \tag{2.17}$$

$$W^{\mathrm{Oe}} = -\frac{\mu_0}{2} C J M_s R^3 h \sum_{i=0}^{5} a_i^{\mathrm{Oe}} s^{2i}, \tag{2.18}$$

where a_i^{ex}, a_i^{ms}, a_i^{Oe} are the dimensionless coefficients to be fitted relative to each term of the polynomials. Nonlinear least-squares fits are performed for $s \in \left[5 \times 10^{-4}, 0.7\right]$, with the upper value being close to the limit of vortex stability found in Section 2.1. Using an adapted version of Equation (2.14), *i.e.*, $k = (\partial W/\partial s)/\left(sR^2\right)$, one can easily derive the expressions of the springlike stiffness parameters, given as

$$k^{\mathrm{ex}} = -\frac{\pi h A}{R^2} \sum_{i=1}^{5} (2i) a_i^{\mathrm{ex}} s^{2(i-1)}, \tag{2.19}$$

$$k^{\mathrm{ms}} = \frac{\mu_0 M_s^2 h^2}{R} \sum_{i=1}^{5} (2i) a_i^{\mathrm{ms}} s^{2(i-1)}, \tag{2.20}$$

$$\kappa^{\mathrm{Oe}} = -\frac{\mu_0}{2} M_s R h \sum_{i=1}^{5} (2i) a_i^{\mathrm{Oe}} s^{2(i-1)}. \tag{2.21}$$

In addition, a pretreatment is used before fitting. It consists of denoising the raw micromagnetic results thanks to a wavelet transform technique [134]. This allows to obtain more accurate fitting parameters by getting rid of mumax^3 internal computational uncertainties. For every fit, we obtained a relative standard error on the intercept a_0 [see Equations (2.16) - (2.18)] of 0.00%. For the quadratic coefficient a_1 (biquadratic a_2), it is always below 0.02% (2.25%, while being below 1% for most fits). Concerning the higher-order coefficients a_3, a_4, and a_5, the errors were often a bit more important, which can be easily understood. Indeed, as $s < 1$ by definition, these terms contribute only to a limited extent to the total energy value.

2.2.2 Realistic stiffness parameters

Micromagnetic results [see Equations (2.19) - (2.21)] are compared to the analytical expressions previously presented [see Equations (2.3) - (2.5)]. The evolution of the restoring parameters k^{ex}, k^{ms}, and κ^{Oe} with respect to the vortex core position is depicted in Figures 2.5 - 2.7, respectively. Let us start with general observations that are valid for the three energy components.

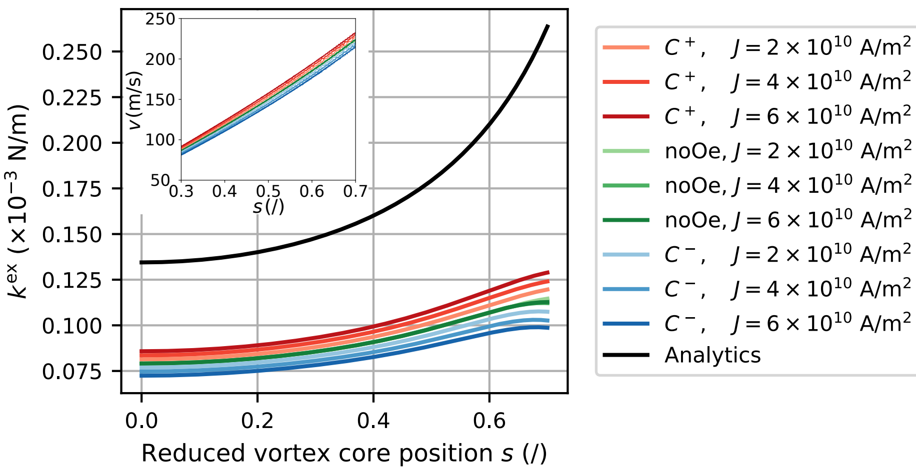

Figure 2.5: Exchange stiffness parameter k^{ex} as a function of the reduced vortex core position s. The analytical expression [black line; see Equation (2.3)] is compared to micromagnetic simulation (MMS) results [colored lines; see Equation (2.19)]. The colors green, red and blue correspond to simulations without AOF (noOe), with AOF and $C = +1$ (C^+), and with AOF and $C = -1$ (C^-), respectively. The applied current densities J were 2, 4, and 6×10^{10} A/m^2. MMS results were obtained after performing a nonlinear least-squares fit on the exchange energy [see Equations (2.16) & (2.19)]. The inset shows the vortex core velocity v as a function of the reduced vortex core position s. Adapted from Ref. [126].

A slight disagreement is noticed between the micromagnetism and TEA, even when the vortex core is at the center of the nanodot. These discrepancies could originate from two main hypotheses performed during TEA calculations. First, the out-of-plane magnetization component m_z is neglected for each derivation [62] due to the small area occupied by the vortex core. This simplification, that is necessary to obtain fully analytical expressions, is applicable as a preliminary approximation. However, even if the vortex core profile contribution is small, it is still different from zero. This is especially true for nanopillars of reduced radius, where the vortex core occupies a significant surface inside the free layer. Second, the magnetization **m** is considered constant along the dot thickness. While appropriate for nanodots presenting a thickness of the order of the exchange length [6,82,135], this assumption is not perfectly confirmed in micromagnetic simulations.

In addition, supplementary deviations arise for an off-centered moving vortex core, partly explaining the TEA imperfect modeling when s is evolving. Indeed, within TVA, the vortex core is simply translated to a greater orbit, while keeping its original shape. Such rigid motion assumption is justified by the fact that this *Ansatz* was originally designed to study small displacements of static vortex cores. However, various groups [84,93,133] have already shown the limitations of such theoretical framework to accurately model dynamic vortices. It has also been shown that a vortex core approaching the dot edge sees a growing trail of opposite magnetization appearing next to it [62,135,136]. Such dip, later responsible for the nucleation of a vortex of reversed polarity [137], induces energy changes [138] not perceived within TEA and will be discussed in Chapter 3.

Furthermore, a current-induced splitting of the stiffness parameters can be observed, as already reported by Choi *et al.* [99]. For increasing currents, the C^- and C^+ curves move further apart from the noOe case. This behavior is not predicted at all by the TEA calculations. These findings result from a modification of the spin distribution **m** caused by the AOF. Spins are tilted under its influence, leading them to deviate from the theoretical TVA magnetization. These effects will be discussed later in this Chapter.

This distortion increases near the dot edges, considering the linear dependence of the AOF amplitude on the radial coordinate r within the free layer. Moreover, the splitting increases with the current density as the AOF amplitude is proportional to the latter. This conclusion is supported by the fact that in the noOe configuration, the stiffness is independent of the current value. Indeed, the mean difference in the simulations at 4 and 6×10^{10} A/m^2 compared with those at 2×10^{10} A/m^2 is less than 0.17% for the exchange stiffness, and less than 0.06% for the magnetostatic stiffness (see green curves in Figures 2.5 & 2.6). Finally, for the exchange contribution, the favored configuration (*i.e.*, C^+) results in a stiffer force parameter, while the opposite is noticed for the other terms. As for now, we lack a robust justification for this phenomenon and further investigations would be needed.

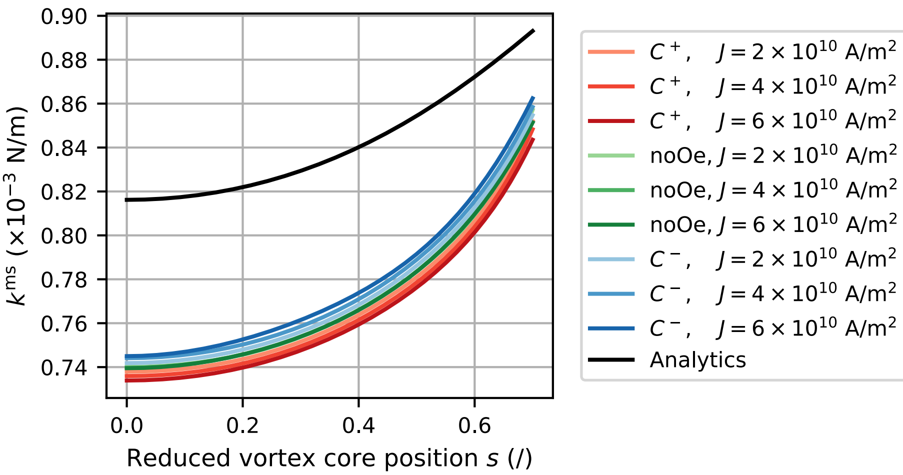

Figure 2.6: Magnetostatic stiffness parameter k^{ms} as a function of the reduced vortex core position s. The analytical expression [black line, see Equation (2.5)] is compared to micromagnetic simulation (MMS) results [colored line; see Equation (2.20)]. The colors green, red and blue correspond to simulations without AOF (noOe), with AOF and $C = +1$ (C^+), and with AOF and $C = -1$ (C^-), respectively. The applied current densities J were 2, 4, and 6×10^{10} A/m^2. MMS results were obtained after performing a nonlinear least-squares fit on the magnetostatic energy [see Equations (2.17) & (2.20)]. Adapted from Ref. [126].

After these preliminary observations, let us now look at each of the confinement contributions in more detail. The TEA exchange stiffness parameter k^{ex} is the term presenting the most imprecise description compared to the simulated behavior (see Figure 2.5). For each s, the analytical value overestimates all MMS results. The predicted evolution is satisfactory for a slightly off-centered vortex, but diverges [5,62] to infinity for $s \to 1$, as expected from Equation (2.3) and the disregard of the vortex core profile in the analytical derivation. This does not reflect the behavior extracted from simulations as a maximum seems to appear at $s \approx 0.7$ (at least for C^- and noOe), followed by a decrease of the k^{ex} value. Various reasons could explain this drop. The most probable ones would be the interaction of the core with the dot edge and the six-neighbor small-angle approximation used by micromagnetic solvers, preventing accurate computation for large excitations. Moreover, a very large impact of the AOF is noticed. For a centered vortex core and $J = 6 \times 10^{10}$ A/m^2, the exchange stiffness in the C^+ configuration is 18% larger than the curve of opposite chirality. This value grows up to 31% at $s = 0.7$. Such considerable influence is linked to the fact that the gradient of magnetization $\nabla \mathbf{m}$ appears in the exchange energy formula, as shown in Equation (2.15). Any slight deviation in the spin directions appearing in the simulations with AOF has therefore a major impact on the stiffness results compared to calculations using the unaffected theoretical distribution.

In addition, the rotational velocity v of the vortex core can give an indication of its degree of deformation (see inset in Figure 2.5), especially when compared with the critical velocity (in cgs units) $v_{\mathrm{cr}} \simeq 1.66\gamma\sqrt{A}$, where γ is the gyromagnetic ratio [139]. The velocities reached at the largest oscillation orbits are gradually approaching $v_{\mathrm{cr}} = 302$ m/s, suggesting a large dip following the vortex core. An impact of the chirality on the velocity was to be expected, given the frequency splitting reported in Section 2.1. However, the impact of the current magnitude on the velocity, for the same chirality and vortex core position, shows its influence on the magnetization dynamics.

In Figure 2.6, one can observe that as expected, the magnetostatic confinement largely dominates both other terms [82,140], at least for the explored range of currents. For dots with wider radii or at very large current densities, the AOF stiffness parameter k^{Oe} should gain relative importance. The analytical expression of k^{ms} overestimates the value extracted from the simulations (for the noOe case) by 10% at $s = 0$. This result is consistent with the overestimation of the first critical current J_{c1} and eigenfrequency ω_0 observed in Section 2.1 when using TEA, as J_{c1} and $\omega_0 \propto k^{\mathrm{ms}}(s = 0)$. As depicted in Figure 2.6, the magnetostatic confinement constantly increases as the core moves towards the edge, for both methods, though the growth is limited, as k^{ms} is only 15% greater at $s = 0.7$ compared to the centered vortex case (for noOe). The analytical function models well the simulated evolution of k^{ms} with respect to s for low vortex displacements. For greater s values, however, discrepancies are observed between the two methods. This difference is partially explained by the difficulty to obtain an analytical expression for the stray field [62]. The AOF seems to have a limited impact on the magnetostatic energy, with all curves being close to the noOe configuration.

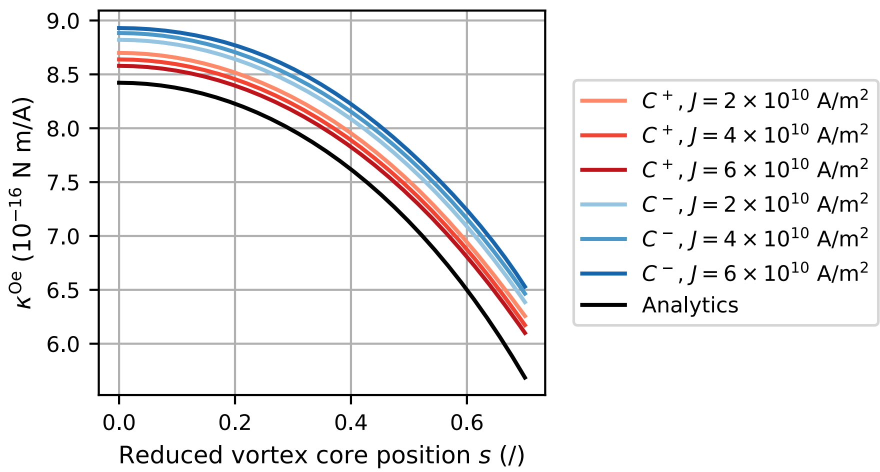

Figure 2.7: Ampère-Oersted field (Zeeman-like) stiffness parameter κ^{Oe} as a function of the reduced vortex core position s. The analytical expression [black line; see Equation (2.4)] is compared to micromagnetic simulation (MMS) results [colored lines; see Equation (2.21)]. The colors red and blue correspond to simulations with AOF and $C = +1$ (C^+) and with AOF and $C = -1$ (C^-), respectively. The applied current densities were 2, 4, and 6×10^{10} A/m^2. MMS results were obtained after performing a nonlinear least-squares fit on the Zeeman energy [see Equations (2.18) & (2.21)]. Adapted from Ref. [126].

Furthermore, the analytical expression of κ^{Oe} underestimates the simulation results (see Figure 2.7), for both C^+ and C^-. However, the predicted behavior finely describes its evolution on the whole s range. Such accuracy was bound to occur given the easier derivation of the Zeeman energy, compared to nonlocal magnetostatic interactions. It may also be due to the higher-order polynomial used in Equation (2.4). More fundamentally, the AOF does not present any out-of-plane component as it appears in a plane perpendicular to the current direction, if edge effects are negligible. Following Equation (2.15), the out-of-plane vortex magnetization m_z thus has a negligible impact on the Zeeman energy. Nevertheless, constantly decreasing curves are obtained, with κ^{Oe} being 40% greater for a centered vortex than in $s = 0.7$. Note that κ^{Oe} differs in units from the other spring-like parameters, as it corresponds to $k^{Oe}/(CJ)$. In addition, a nonnegligible impact of the AOF is again perceived on its own stiffness parameters κ^{Oe}, in the simulations. This result was expected, as we get a modification of the magnetization distribution **M** appearing in Equation (2.15). The splitting stays roughly constant in amplitude, irrespective of the vortex core position.

It seems important to underscore the profound dynamical changes induced by the Ampère-Oersted field. Beyond expected direct impacts, such as the modification of the system Zeeman energy, we highlight here significant second-order effects that the AOF imposes on the other energy components.

2.2.3 Deformation of the magnetic texture

Finally, let us look at the magnetic texture and the influence of the AOF on it. In Figure 2.8, we define the mean angular deviation as $\overline{\delta} = \sum_i^N |\delta_i|/N$, where δ_i is the angle between the planar magnetization vector $\left(m_x, m_y\right)$ predicted by the TVA [see Equations (1.20) & (1.21)] and the one retrieved from simulations, for a given micromagnetic cell, and N is the total number of cells. In other words, we seek to compute the signed angles δ_i between the planar angles ϕ^{MMS} retrieved from simulations in each cell and the angles ϕ^{TVA} describing the planar magnetization predicted by TVA in the corresponding cells, for every vortex core position. The effects of the core deformation will be discussed afterwards.

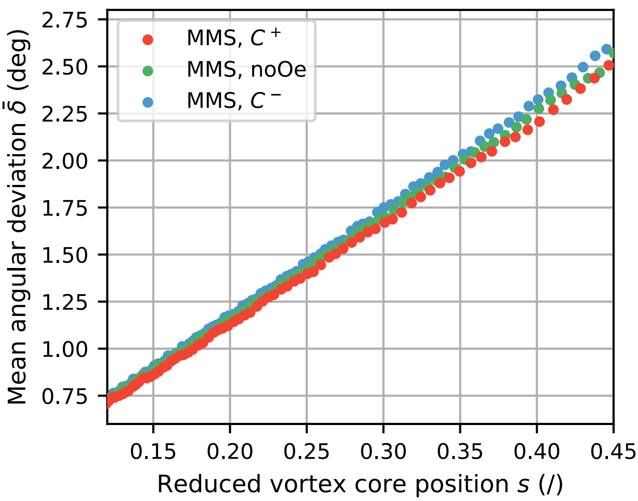

Figure 2.8: Mean angular deviation between the planar magnetization vector predicted by the two-vortex *Ansatz* and the one retrieved from simulations, as a function of the reduced vortex core position ($J = 4 \times 10^{10}$ A/m^2). Adapted from Ref. [126].

The mean deviation is close to zero for low s values and increases the further the vortex core is located from the center, as expected given that the TVA was designed for statics. What is more useful here is to use the TVA as a reference to compare the three configurations that we are examining. As already suggested by the inset in Figure 2.5, the deformation of the magnetic texture depends on the relative orientation between the in-plane swirling spins and the AOF. In addition, the splitting of the angular deviation widens as the core approaches the edge of the magnetic disk.

To better understand these results, an out-of-plane snapshot of the angular deviation for each cell of the disk during a simulation is illustrated in Figure 2.9. As anticipated, the regions that deviate most from the TVA predictions are those close to the core (*i.e.*, the dip) and at the edges of the disk. As the core moves towards the center, the deviations gradually become smaller.

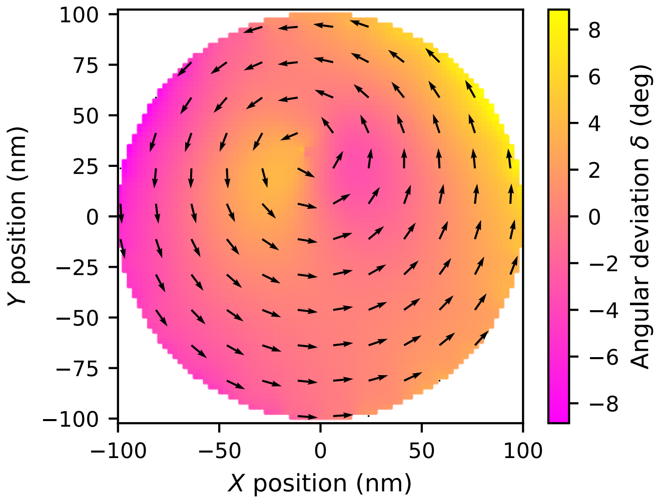

Figure 2.9: Out-of-plane snapshot of the angular deviation between the two-vortex *Ansatz* and simulations for a dynamic off-centered vortex core, in each cell of the free layer ($J = 4 \times 10^{10}$ A/m^2). Adapted from Ref. [126].

In Figure 2.10, one can observe the deformation of the core profile for a centered vortex. To do so, we compare the out-of-plane magnetization components of two free layers under the same current, but containing vortices of opposite chiralities. A more stringent cell size of $0.5 \times 0.5 \times 2.5$ nm^3 was used for a finer precision. As $\|\mathbf{m}\| = 1$, we plot $m_z^{C^+} - m_z^{C^-}$ to highlight any variation in the planar magnetization components. At exactly $(0, 0)$, there is no difference between both situations as the amplitude of the AOF is zero at these coordinates. In every other point of the vortex core, though, the magnetization is confined in the plane by the AOF, modifying the values of m_x and m_y. By conservation of the norm, the value of m_z changes by an amount that depends on the relative orientation between the planar magnetization and the magnetic field. Such effect is comparable to what was reported by de Loubens *et al.* [95] and Dussaux *et al.* [86] for a perpendicular magnetic field, *i.e.*, $m_z = H_\perp/H_s$ (with H_s the saturation field), where part of the magnetization was imposed outside the vortex core by the addition of an external field. In our case, however, little effect is visible outside of the vortex core. In fact, as the magnetization is planar for both chiralities in this region, m_z (which is nearly zero) is not impacted by the confinement. For reference, the half width at half maximum of the vortex core profile is ~ 7 nm.

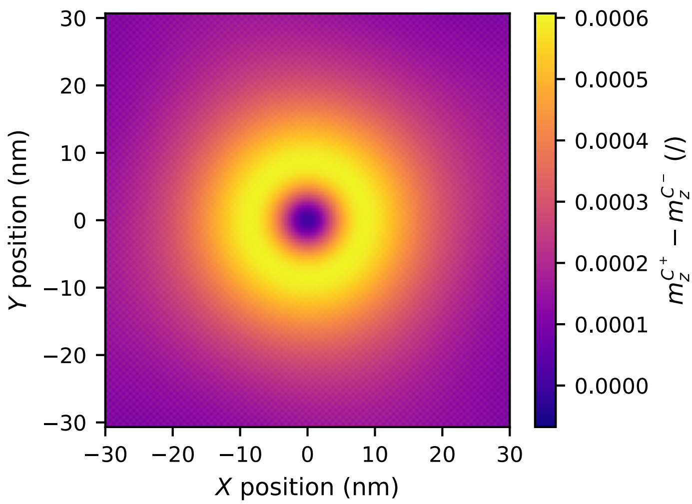

Figure 2.10: Comparison between the out-of-plane magnetization components for two centered vortices of opposite chiralities, under the same applied current of $J = 4 \times 10^{10}$ A/m^2. Adapted from Ref. [126].

As depicted in Figure 2.11, the maximum deformation depends quasilinearly on the amplitude of the current. This effect is a direct evidence of the influence of J, and therefore of the AOF, on the magnetic texture. The choice of working at $s = 0$ was made to ensure that the core is at exactly the same location regardless of the chirality, even if the deformation is fairly small at this position. One last important thing to note is that part of this distortion originates from the spin-transfer torque. However, the further the core is from the center, the greater the relative contribution of the field to the deformation, as its amplitude increases with the position. Moreover, the value of the energy at $s = 0$ is of little importance for the stiffness parameters since those are rather linked to the shape of the potential well.

To put the results presented in this work into perspective, we believe that our restoring parameter expressions could be integrated into existing TEA models, to replace analytical expressions. Following such a data-driven approach, *i.e.*, deriving k^{ex}, k^{ms}, and κ^{Oe} from a limited set of micromagnetic simulations, one could obtain more reliable results from TEA compared to micromagnetism and, by extension, to experimental results. On the other hand, these parameters would only be valid for a given geometry and material parameters. Moreover, to obtain expressions that are valid for a continuous range of currents, one should proceed to an interpolation between a few curves that are cleverly selected, as the splitting increases with J.

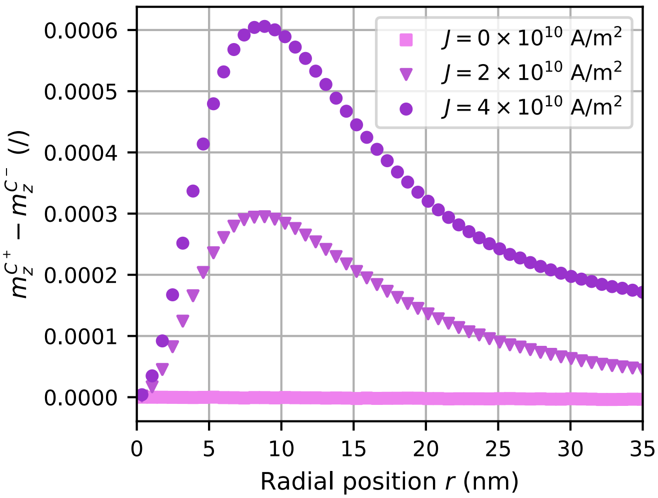

Figure 2.11: Cross-section of the difference in m_z profiles, *i.e.*, $m_z^{C^+} - m_z^{C^-}$, at the center of the disk as shown in Figure 2.10, at various current densities J. Adapted from Ref. [126].

Nevertheless, this constitutes an alternative solution for a more accurate analytical model describing STVO dynamics. For instance, in a noOe configuration, substituting the analytical expressions of k_0^{ex} and k_0^{ms} with the values derived from MMS enables recalculating the f_0 and J_{c1} values given in Section 2.1. This substantial improvement reduces the relative error, compared to simulation results, from 17.9% to 1.5% for the resonance frequency and from 13.6% to 2.1% for the first critical current.

Although the influence of the temperature was not taken into account in this study, one may still discuss its potential effect on the restoring forces. It is well known that a magnetic tunnel junction powered by large current densities sees its temperature rise [141,142,143], by up to several tens of degrees [144]. This Joule heating is especially important close to the tunnel barrier (typically made of MgO and spatially adjacent to the free layer hosting the magnetic vortex) as its resistance is orders of magnitude higher than that of the metallic layers. More importantly, the temperature that is reached depends on the magnitude of the current [144]. This means that the splitting phenomenon of the restoring forces, only caused by the current-induced Ampère-Oersted field in the present study (as $T = 0$ K), could be enhanced by the larger temperature increase for higher currents. Indeed, any local random fluctuation of the spin texture **m** due to thermal effects directly impacts the value of the energy components, following Equation (2.15). It is clear that these effects, as well as the impact of the temperature on the different material parameters, could be considered in future works to further improve the validity of TEA-based models.

2.3 Conclusion

The aim of Section 2.1 was to introduce energy terms into the Thiele equation valid over a wider range of vortex core positions, and to render precisely the impact of the Ampère-Oersted field on the dynamics. We have observed a splitting due to the AOF and that the latter depends on the chirality of the vortex. The improved analytical model, which is valid for $0 \leq s \leq 0.8$ thanks to corrections of the magnetostatic and AOF contributions, is coherent with the micromagnetic simulation results for J_{c1} and ω in the resonant regime. This shows the importance of the AOF for understanding the complex nonlinear dynamics of vortex-based nano-oscillators. The splitting shown and modeled here represents a supplementary degree of freedom of such oscillators with potentially a high impact on future applications. For instance, we believe that our analytical model is among the first steps towards making a fast model for the simulation of STVOs in the framework of reservoir computing [112] and building complex hardware-based neuromorphic computing devices. Although the updated model produces promising results in the resonant regime, the nonlinear oscillating regime is not described quantitatively. The objective of Section 2.2 was therefore to understand the differences in the magnetic energy landscape between the TEA and MMS.

Restoring forces appearing in off-centered magnetic vortex states were then examined theoretically. Exchange, magnetostatic, and Zeeman stiffness parameters were obtained from simulations and compared to the analytical expressions presented in Section 2.1. To do so, the energy components were directly extracted from mumax^3, then fitted to high-order polynomials. The derivatives of these functions allowed us to calculate the stiffness parameters, analogously to what is done for classical springs under deformation. Discrepancies between the Thiele equation approach results and micromagnetic simulations were observed for each term, such as shifts of the curves and disagreeing behavior for large relative core position values. These differences were expected given the assumptions used for the theoretical derivations. More importantly, a chirality-dependent splitting was observed in the stiffness value, with a deviation depending on the input current intensity. We have provided evidence that this phenomenon is the result of a modification of the spin distribution caused by the current-induced Ampère-Oersted field. This hypothesis is supported by the fact that the stiffness was independent of the current imposed when the AOF was not taken into account. Finally, we believe that the expressions we derived from the simulations could be implemented into existing STVO models to better render experimental results.

Chapter's take-home message

- A **chirality-dependent splitting** of the dynamics is attributed to the impact of the **Ampère-Oersted field** on the vortex energy.
- An **improved analytical model**, based on the Thiele equation, renders properly the **resonant regime dynamics**, but lacks accuracy for describing the **nonlinear oscillating regime**.
- A **method** has been developed **to extract stiffness parameters from micromagnetic simulations**, revealing **significant deviations** from analytical derivations caused by the Thiele equation assumptions.
- The combination of these outcomes provides **elements for enhanced STVO operation**, particularly through the chirality, and marks a step towards an **improved modeling of vortex dynamics** considering second-order impacts of the AOF on the vortex texture.

3

Data-driven Thiele equation approach

As highlighted in Chapter 2, there is an inherent difficulty in obtaining quantitative results from a purely analytical model, notably due to the assumptions required for the derivations which do not account for the complexity of vortex dynamics. In addition to the discrepancies pointed out in the vortex stiffness, a significant problem in the model employed up to now lies in the fact that the gyrotropic and damping terms are considered constant, which is a significant oversimplification. For various reasons, it is challenging to extract their s -dependence analytically. We therefore propose an alternative solution, which consists of performing micromagnetic simulations to then force our model, becoming semi-analytical, to yield the same results. We will see that, in addition to unanticipated accuracy, especially in the transient regime, this method allows considering signals of realistic duration for applications.

In Section 3.1.1, the gyrotropic and damping terms of the TEA are refined using data-driven corrections, starting from the fully analytical model presented in Section 2.1. This adapted model accurately predicts both the transient and steady-state regimes of the STVO to any dc current within the vortex stability range. Moreover, the computation time is reduced by approximately six orders of magnitude compared to state-of-the-art MMS. Beyond these results, we offer in Section 3.1.2 another model that is around 100 times faster than the first one, at the cost of becoming phenomenological. Finally, while tuning our model for wider diameters, we came across a particular dynamic regime, where the vortex core remains confined due to successive polarity reversals. Our data-driven method, developed primarily with Dr. Chloé Chopin and Prof. Flavio Abreu Araujo, is detailed in two preprints; one addressing the s-dependence of $G(s)$ and $D(s)$ [145], and another presenting our fastest model [146]. Additionally, Anatole Moureaux, another member of the Neuromorphic Engineering Group integrated these results into artificial neural network for pattern recognition purposes [146,147]. Separately, we recently published in *Scientific Reports* the periodic polarity reversal results [148].

3.1 Fast and accurate modeling of the STVO dynamics

Micromagnetic simulations, despite their accuracy compared to experimental measurements [149], suffer from high computational costs and lengthy execution times, rendering them impractical for realistic signal processing. Analytical models offer faster alternatives for describing the vortex trajectory. Simple models, such as exponential decay [112], have been used to approximate the transient vortex core dynamics, while the Thiele equation, extensively introduced in this thesis, is more commonly examined. However, it has yielded only qualitative results due to complex mathematical derivations involved for vortex topologies. This Section presents a novel hybrid method, *i.e.*, semi-analytical, which is both fast and accurate for describing vortex core precessions. By adapting the gyro- and damping terms in the Thiele equation using a small set of MMS, our approach captures the STVO response to arbitrary current waveforms in both transient and steady-state regimes. We show that this technique accelerates computation by several orders of magnitude compared to MMS, while maintaining precision.

3.1.1 Nonlinear gyrotropic and damping terms

In our fully analytical TEA model, presented in Section 2.1, we assumed that the gyrotropic and damping constants were independent of the vortex core position, with $G = -2\pi P M_s h/\gamma_G \equiv G_0$ for the gyroconstant and $D = -\alpha_G \eta |G| \equiv D_0$ for the damping term. This assumption led to consistent predictions in the resonant regime, *i.e.*, $s = 0$, but lacks accuracy for nonlinear auto-oscillations. In the present Section, we propose to take into account the s-dependence of $G(s)$ and $D(s)$. As the calculation of the latter is an impractical task [80,86,87,127,150], notably because it needs to include the deformation of the vortex core under excitation, no convincing expression exists in the literature to describe their evolution with respect to the vortex core position, to the best of our knowledge. Thence, we chose a more convenient approach, consisting in modeling $G(s)$ as $G_0\delta_G f_G(s)$ and $D(s)$ as $D_0\delta_D f_D(s)$, where δ_G and δ_D are global correction factors, while $f_G(s)$ and $f_D(s)$ are functions of s that need to be determined. The functions $f_G(s)$ and $f_D(s)$ should allow to retrieve $f_G(0) = 1$ and $f_D(0) = 1$, so that $G_0\delta_G$ and $D_0\delta_D$ can be used as data-driven corrected gyro- and damping constants, respectively. Using the matrix $\bar{\bar{\mathbf{\Omega}}}$, presented in Equation (2.7), the following system can be derived:

$$\begin{cases} D(s)\Gamma - G(s)\omega = k^{\text{ex}} + k^{\text{ms}} + k^{\text{Oe}} \\ D(s)\omega + G(s)\Gamma = J\kappa_{\perp}^{\text{ST}} \end{cases} . \tag{3.1}$$

As $\Gamma = 0$ in steady-state oscillating regime, one finds that

$$\delta_G f_G(s) = -\frac{k^{\mathrm{ex}}(s) + k^{\mathrm{ms}}(s) + CJ\kappa^{\mathrm{Oe}}(s)}{G_0\omega(s)}, \tag{3.2}$$

$$\delta_D f_D(s) = \frac{J\kappa_\perp^{\mathrm{ST}}}{D_0\omega(s)}, \tag{3.3}$$

where k^{ex}, k^{ms}, κ^{Oe}, and $\kappa_\perp^{\mathrm{ST}}$ are the analytical expressions introduced in Section 2.1. While MMS-derived stiffness expressions, presented in Section 2.2, may be more accurate, we keep using the analytical forms for simplicity, as a numerical fitting is required in any case to calculate $G(s)$ and $D(s)$. We note that the global correction factors δ_G and δ_D thus aim at absorbing any inaccuracy in the fully analytical TEA model, even at $s = 0$. As discussed in Section 2.2, these discrepancies may arise from the analytical expressions of G_0 and D_0, but also from the other terms at $s = 0$, notably the vortex stiffness and the spin-transfer forces. It is also possible that the inertial mass term of the Thiele equation, neglected in our analytical model, is partially accounted for in these adjustments.

The sole parameter still unknown in Equations (3.2) & (3.3) is the pulsation $\omega(s)$. Yet, it can be easily extracted from MMS that have reached steady-state, *via* $\omega(s) = 2\pi f^{\mathrm{STVO}}(s)$. Therefore, one can calculate $G(s)$ and $D(s)$ by performing a fit on several simulation results, which will considerably improve the model predictions for $s \geq 0$. Let us precise that the input parameter of micromagnetic solvers is the injected current, involving a substitution to get $\omega(s)$ from $s(J)$ and $\omega(J)$. After testing multiple options, our final choices for the fitting functions $f_G(s)$ and $f_D(s)$ are

$$\delta_G f_G(s) = \frac{\delta_G}{\left(1 - \frac{\delta_G}{a_G}\right)e^{-(b_G s + c_G s^7)} + \frac{\delta_G}{a_G}}, \tag{3.4}$$

$$\delta_D f_D(s) = \delta_D\left(1 + a_D s + b_D s^2 + c_D s^3 + d_D s^4\right), \tag{3.5}$$

where the parameters δ_G, a_G, b_G, c_G, δ_D, a_D, b_D, c_D, and d_D are to be calculated. It is noteworthy that our fitting function selection is not unique, and various alternative expressions could have been considered.

Keeping the same system as in the previous Chapter, *i.e.*, a $(R,h) = (100,10)$ nm permalloy free layer, the intrinsic gyrotropic frequency $f^{\mathrm{STVO}}(s) = \omega(s)/(2\pi)$ with respect to the reduced orbit radius s, has already been presented in Figure 2.4. As a reminder, these data were derived from steady-state mumax^3 simulations ($s \in]0.0, 0.8]$). A cubic interpolation is then performed to increase the amount of available fitting data points. As expected, different sets of fitting parameters are derived depending on the configuration (C^+, C^-, or noOe). In addition, the boundaries used to perform fitting are chosen to remain in the nonlinear oscillating regime. This condition translates to data points starting from 5.8, 6.2, and 6.5×10^{10} A/m^2 and ending at 8.4, 9.0, and 9.8×10^{10} A/m^2, for C^-, noOe, and C^+, respectively. These current densities are therefore spread out between the first and the second critical currents, J_{c1} and J_{c2}.

Since the angular frequency $\omega(s)$ is known from MMS, the right hand side of Equation (3.2) can be determined for any s value. A nonlinear least-squares method is then used to fit the function proposed in Equation (3.4). The obtained coefficients are reported in Table 3.1.

	δ_G	a_G	b_G	c_G	max(|err|) (%)
C^+	1.1670	1.1638	−4.3837	−2.1972	0.22
noOe	1.1785	1.1754	−4.4929	−2.0772	0.21
C^-	1.1926	1.1892	−4.4139	−2.1898	0.24

Table 3.1: Coefficients of the fitting function given in Equation (3.4), for each configuration. Those are calculated from Equation (3.2) by a least-squares non-linear fit, after a cubic interpolation on steady-state MMS data. The maximum relative error between fit and simulation is also indicated.

As previously stated, a global correction factor δ_G is introduced to take into account any discrepancies between the fully analytical model and the MMS results, even in resonant regime, *i.e.*, $s = 0$. One can observe that δ_G is greater than 1 for the three configurations, which originates from the overestimation of the vortex stiffness, presented in Section 2.2, or could also indicate an underestimation of the gyroconstant G_0. The evolution of $\delta_G f_G(s)$ with respect to the vortex core position is depicted in Figure 3.1. The counterbalance of the theoretical exchange term could especially become dominant for high currents, as it diverges for $s \to 1$ [see Equation (2.3)]. A strong splitting between the three configurations is noticed, validating once more the results presented in Chapter 2.

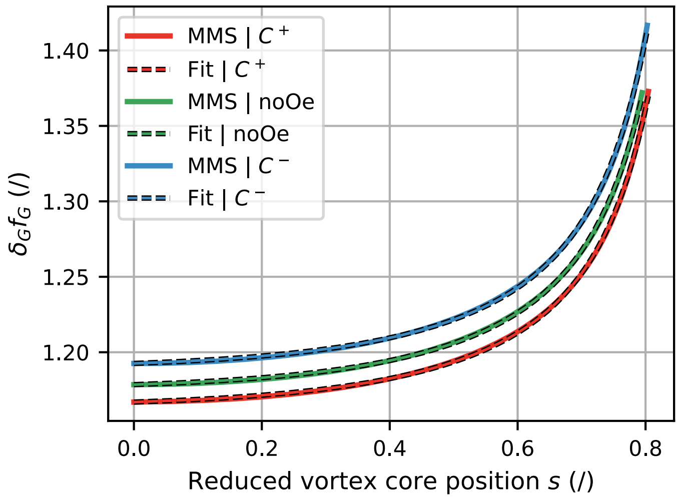

Figure 3.1: Value of $\delta_G f_G$ as a function of the vortex core position s, for each configuration C^+, noOe, and C^-, identified with red, green, and blue colors, respectively. The results calculated from Equation (3.2) (colored lines) are obtained after performing a cubic interpolation on steady-state MMS data, presented in Figure 2.4. The corresponding polynomial fits [see Equation (3.4)] are presented by dashed lines, using the same colors.

An identical methodology is used to extract the s-dependence of the damping term. Knowing $\omega(s)$, the right hand side of Equation (3.3) can be calculated. Once fitted to the polynomial function given in Equation (3.5), the coefficients reported in Table 3.2 are obtained. Similarly to the gyrotropic term, one can observe that the global correction factor δ_D is greater than 1, reporting either a too large spin-torque parameter, or an underestimated damping constant D_0 for a centered vortex core.

	δ_D	a_D	b_D	c_D	d_D	max(|err|) (%)
C^+	1.0284	−0.0367	0.6002	−0.6678	0.7648	0.04
noOe	1.0367	−0.0342	0.5078	−0.5267	0.6098	0.04
C^-	1.0446	−0.0396	0.4942	−0.5545	0.5782	0.02

Table 3.2: Coefficients of the fitting function given in Equation (3.5), for each configuration. Those are calculated from Equation (3.3) by a least-squares non-linear fit, after a cubic interpolation on steady-state MMS data. The maximum relative error between fit and simulation is also indicated.

The value of $\delta_D f_D(s)$ as a function of s is given on Figure 3.2. A more monotonous evolution is reported, compared to $\delta_G f_G(s)$. Again, a clear splitting between the three configurations is noticed. Here, one can assume that the s-dependence of the $f_D(s)$ function is closer to the theoretical damping term $D(s)$, compared to the $G(s)$ situation, given that the spin-transfer term is implemented in similar ways between MMS and TEA.

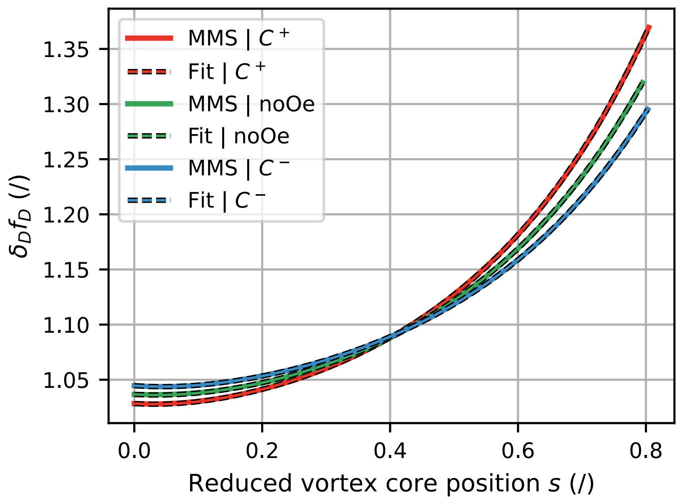

Figure 3.2: Value of $\delta_D f_D$ as a function of the vortex core position s, for each configuration C^+, noOe, and C^-, identified with red, green, and blue colors, respectively. The results calculated from Equation (3.3) (colored lines) are obtained after performing a cubic interpolation on steady-state MMS data, presented in Figure 2.4. The corresponding polynomial fits [see Equation (3.5)] are presented by dashed lines, using the same colors.

As data-driven corrections have been added to the TEA model, *i.e.*, $G(s)$ and $D(s)$, we can now employ it to predict the STVO dynamics with any current density value by simply solving the harmonic oscillator system given in Equation (2.7). A comparison between mumax^3 simulations and our data-driven Thiele equation approach (DD-TEA) model, for the reduced vortex core position $s(t)$ and instantaneous frequency $f(t)$ as a function of time, is given on Figure 3.3 (in the noOe configuration). The input currents are chosen to stay between the two critical currents J_{c1} and J_{c2}. As expected, the steady-state core position values completely overlap for both methods, even for 9.00×10^{10} A/m^2, which leads to $s \approx 0.8$, *i.e.*, the limit of validity of the model. In steady-state regime, the relative error in position prediction is less than 0.2% for the three current densities tested. This value may vary according to the error tolerance in the numerical solver.

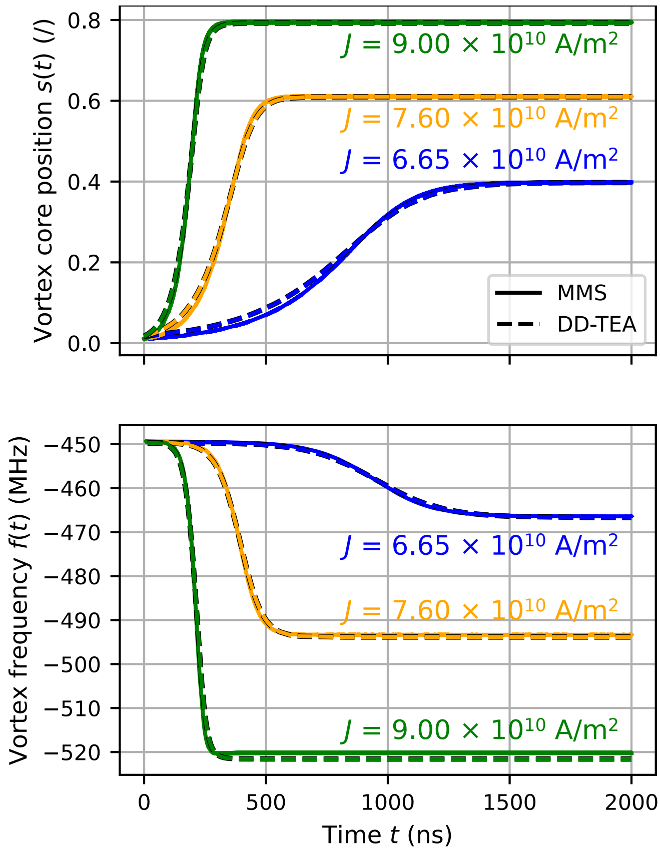

Figure 3.3: Transient regime calculations using micromagnetic simulations (MMS - continuous lines) and the data-driven Thiele equation approach (DD-TEA - dashed lines) for (top) the reduced vortex core position $s(t)$ and (bottom) the gyrotropic frequency $f(t)$. The different input current densities are 6.65, 7.60, 9.00×10^{10} A/m^2 (in blue, orange, and green, respectively). The Ampère-Oersted field is not taken into account (noOe configuration). All simulations were started at $s = 0.01$. Adapted from Ref. [145].

Regarding the frequency, all curves start at $|f| \approx 449$ MHz. This frequency corresponds to a vortex core position of $s = 0.01$ (see Figure 2.4), the starting point of the simulations. As this orbit is close to $s = 0$, the frequency is almost equal to $\omega_0/(2\pi)$. As time passes, the frequency evolves to the steady-state value corresponding to the current imposed. Various works [62,86,100] propose TEA-based predictions of the steady-state orbit and/or the oscillation frequency, but rarely with quantitative agreement due to the lack of consideration of high-order terms. As far as the transient regime is concerned, only Guslienko *et al.* [80] proposed a suitable expression, to the best of our knowledge. In the present study, a close match between MMS and TEA is obtained. Relaxation time are also consistent with simulations. This is not straightforward as only steady-state results were used to calibrate the coefficients of the model. Only negligible shift between both methods is noticed in the transient regime, for the lowest current curves. In steady-state regime, the relative error on the frequency prediction is 0.26%, for the worst case (*i.e.*, $J = 9.00 \times 10^{10}$ A/m^2).

Numerical integration of the STVO dynamics using mumax^3 overs 2 µs requires approximately three hours on an NVIDIA Tesla A100 GPU. Employing our DD-TEA model reduces this computation time to roughly 10 ms; a speedup of six orders of magnitude. For comparison purposes, Chen *et al.* [11] reported a 200 acceleration factor for solving similar problems recently, using a neural ODE technique, although their method is more versatile. This substantial speedup arises from a significant reduction in the number of equations to be solved. Mumax^3 solves the LLGS equation in each cell, for each timestep, across the three spatial directions, totalling around 30k equations per timestep for the system under study. In contrast, DD-TEA only requires two equations, governing the in-plane coordinates (X, Y) of the vortex core, treated as a quasiparticle. Additionally, larger radius dots are expected to yield even greater speedup due to the quadratic scaling ($\propto R^2$) of cell number with radius for constant unit cell dimensions. Preliminary tests on a 500 nm radius nanodot (with thickness $h =$ 9 nm) demonstrated an acceleration factor of more than 2M times.

3.1.2 Ultrafast toy-model

Although the results presented in the previous Section look promising, several concerns inherent to the numerical solving of ordinary differential equations remain. Even though a major acceleration is achieved compared to micromagnetic simulations, ODEs remain quite slow to solve numerically. Depending on the numerical scheme used, stability problems are furthermore common, impairing the physical relevance of the obtained results. Since ODE solving relies on an iterative process, if the data varies rapidly, as it is the case for the in-plane coordinates of the vortex core, the time step must be very small to prevent from propagating errors. In order to overcome these limitations, our goal for the next Section will be to find an analytical formula that allows predicting the evolution of the vortex core orbit.

Let us restart from Equation (2.10), found in Chapter 2, describing the vortex core dynamics within the Thiele equation framework:

$$\begin{bmatrix} X(t) \\ Y(t) \end{bmatrix} = \|\mathbf{X}\|\, e^{\Gamma t} \begin{bmatrix} \sin(\omega t) \\ -\cos(\omega t) \end{bmatrix}. \tag{3.6}$$

As a reminder, this solution to the harmonic oscillator system was obtained assuming that ω stays constant and that $\Gamma \to 0$, *i.e.*, a steady-state regime. If one focuses solely on the amplitude of the oscillations $s(t) = \sqrt{X(t)^2 + Y(t)^2}/R$, and not on the Cartesian coordinates varying rapidly with time, the previous equation can be simplified to

$$s(t) = s_\infty e^{\Gamma t}, \tag{3.7}$$

where s_∞ is the final reduced vortex core position, *i.e.*, when complete steady-state is reached ($t \to \infty$). In all generality, the Γ parameter depends on s, and thus also on time. Consequently, a more rigorous form of Equation (3.7) can be written as

$$s(t) = s_\infty e^{\int_0^t \Gamma(s(t'))\mathrm{d}t'}. \tag{3.8}$$

From the previous equations, we can easily find that

$$\dot{s}(t) = \Gamma(s(t))s(t), \tag{3.9}$$

which is an ordinary differential equation linking the variation of s with time and s, through the Γ parameter. We presented the complete analytical expressions of $\Gamma(s)$ in Equation (2.9), based on the TEA. However, for the sake of simplicity in following calculations, we will propose a truncation of Γ to the second-order, which gives

$$\Gamma(s) = \alpha + \beta s^2, \tag{3.10}$$

where α and β are parameters that depend on the current density. We propose linear expressions $\alpha(J) = a_J J + a$ and $\beta(J) = b_J J + b$, although other choices could have been made. In practice, the constants a_J, a, b_J, and b will be fitted from MMS results, as done in Section 3.1.1. As a matter of facts, a slightly different technique can be used to gather micromagnetic simulation data. Previously, we have used steady-state simulation results, meaning that a large number of MMS were required for a reliable fit, and that a supplementary interpolation step was mandatory. In Figure 3.4, we show a simpler and faster method. We propose to work with only two simulations, where the current varies with time rather than remaining constant. Starting at mid-dynamics ($s \approx 0.5$), one simulation decreases below J_{c1}, whereas the other increases to J_{c2}. Slow current ramps ensure that $s(t)$ closely approximates s_∞, enabling the exploration of the whole dynamical range, yielding data of comparable quality as with the other method. A single simulation approach, starting below J_{c1}, was discarded due to metastability at $s = 0$, which could compromise the $s(J)$ correspondence.

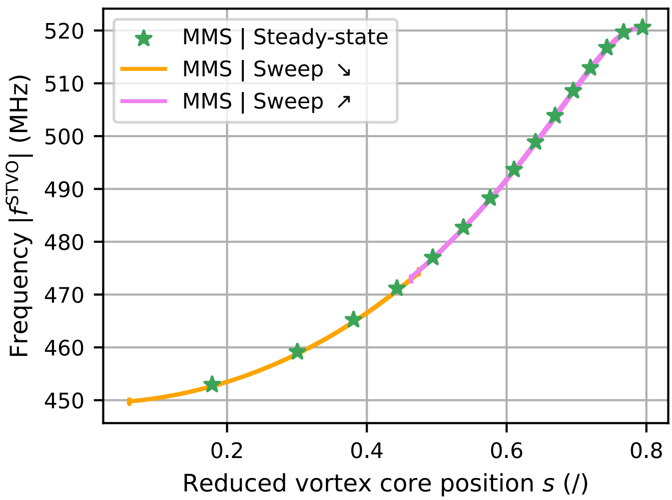

Figure 3.4: Vortex gyrotropic frequency $\left|f^{\mathrm{STVO}}\right|$ with respect to the vortex core position s, in the noOe configuration. Comparison between several simulations that reached steady-state for different constant currents (green stars), with two simulations in which the current is swept slowly over time to correspond to steady-state results ($s(t) \approx s_\infty$). In the first simulation (orange line) the current decreases with time to J_{c1}, whereas it increases to J_{c2} in the second one (pink line).

By substituting Equation (3.10) into Equation (3.9), one finds

$$\dot{s}(t) = \alpha s(t) + \beta s(t)^3, \tag{3.11}$$

which is a Bernoulli-type differential equation of third-order. This equation accepts a solution (see Appendix B for details) of the following type:

$$s(t) = \frac{s_i}{\sqrt{\left(1 + \frac{s_i^2}{\alpha/\beta}\right) e^{-2\alpha t} - \frac{s_i^2}{\alpha/\beta}}}, \tag{3.12}$$

where s_i is the initial position of the vortex core at $t = 0$. Guslienko *et al.* [80] have derived a similar transient regime expression for vortex dynamics using an alternative method.

We will see later in this Section that the simulations performed using this low-order truncated model are more than two orders of magnitude faster than those presented in Section 3.1.1, as no ODE needs to be solved in this model. As introduced before, $\alpha(J)$ and $\beta(J)$ are extracted from MMS, following once more a data-driven approach to fit these parameters. This hybrid model thus accurately describes both transient and steady-state regimes, combining analytical foundations with simulation results. In fact, let us note that this approach can be generalized to any higher-order, to better capture the nonlinearities of the dynamics, compared to the second-order truncation proposed in Equation (3.10). Since equations of the Bernoulli type can involve any real order, one can modify the Equation (3.12) to an order n, which gives

$$s(t) = \frac{s_i}{\left(\left(1 + \frac{s_i^n}{\alpha/\beta}\right)e^{-n\alpha t} - \frac{s_i^n}{\alpha/\beta}\right)^{\frac{1}{n}}}, \tag{3.13}$$

where $n(J)$ is also a function of the current density that can be fitted, simultaneously with α and β, using micromagnetic simulation results. This higher-order model is more accurate than the second-order one, at the cost of an additional fitted parameter, the model then approaching a black box behavior.

One effective approach to validate our model involves subjecting it to an arbitrary waveform, over an extended duration (5 µs in this case). Figure 3.5 (top) illustrates an example of such signal, injected into the STVO, including various waveforms, *e.g.*, ramps, squares, sines, and stair-like currents. In the bottom of Figure 3.5, we present the vortex response, initially investigated with mumax^3 (in orange), which displays expected transient and relaxation behaviors. Conversely, our truncated second-order model, as given in Equation (3.12), may also be used to predict the oscillator behavior under such current, as shown in the same Figure. Before calculating this curve, the α and β parameters were calibrated using MMS data, analogous to the what was done for the model in Section 3.1.1. Remarkably, the data-driven approach exhibits strong concordance with mumax^3 results. The vortex core position is forecasted with a nanometer accuracy, while the steepness of relaxation and excitation dynamics is replicated with high fidelity. It is worth noting that these results were obtained for a configuration where the Ampère-Oersted field is not taking into account.

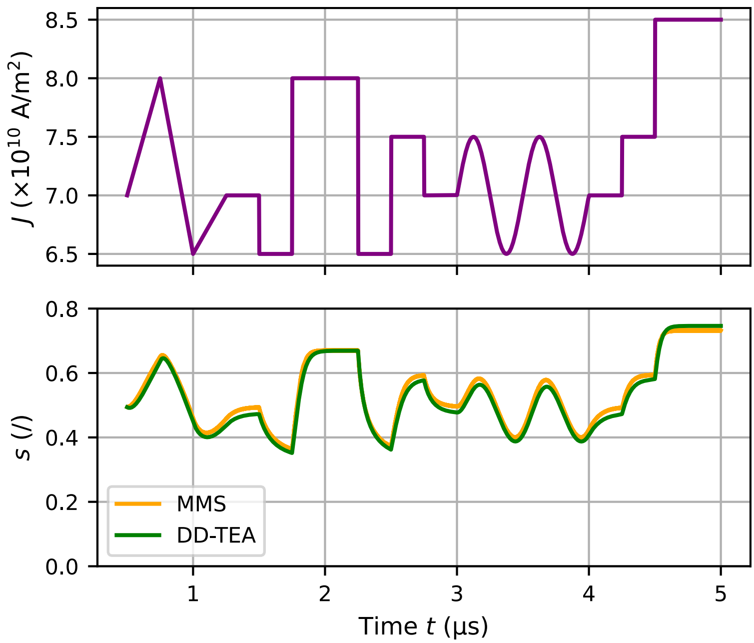

Figure 3.5: Evolution of the reduced vortex core position s, when the STVO is subjected to an arbitrary waveform current density J, as a function of time. Comparison between the results of micromagnetic simulations (MMS, in orange) and the predictions of our low-order data-driven Thiele equation approach (DD-TEA, in green), presented at Equation (3.12).

The true value of our model becomes clear when comparing the time required to obtain the results shown in Figure 3.5. The micromagnetic simulation was performed on an NVIDIA A100 card, one of the most powerful GPUs available, for a simulation time of approximately 11 hours. In comparison, the results obtained using Equation (3.12) require only 400 μs of computation on a simple laptop CPU. This translates to an acceleration of approximately eight orders of magnitude, with virtually equivalent accuracy. Undeniably, these results depend on the number of points calculated, as well as the size of the simulated system, and other parameters like the CPU and GPU models. Nevertheless, such an acceleration factor unlocks the use of these simulation tools in applications for which input signals last several seconds, which would be impossible in a reasonable amount of time with MMS.

We were therefore able to show that the models presented in the Equations (3.12) & (3.13) are reliable representations of the vortex dynamics, at least from a theoretical point of view. Building on these results, Anatole Moureaux was able to show that these models can be used as nonlinear activation functions in artificial neural networks [146,147], in the framework of reservoir computing [112]. Inspired by the pioneering works carried out in Grollier's group [19,20], he was able to confirm, together with our group at UCLouvain, the interest of using STVO digital twins for recognition tasks, which would have been unfeasible through micromagnetic simulations. Although our model combines analytical rigor with computational efficiency, we should not ignore its current limitations.

Preliminary, the fitted coefficients in the $G(s)$ and $D(s)$ expressions are calculated for specific geometries and materials. However, this issue is mitigated by our fitting procedure, enabling rapid (within hours) recalibration *via* a couple of micromagnetic simulations. This becomes even more relevant upon comparison with experimental devices, since the latter will never change in size or materials once fabricated. The critical shortcoming lies in the omission of magnetic fields, which can dynamically influence the vortex behavior. Planar fields offset the vortex core [5] and perturb its circular motion, while OOP fields modify strongly the magnetization distribution [86], consequently altering the Thiele equation terms. Future work must address these field-induced effects, likely also necessitating data-driven corrections. Finally, we are currently working on obtaining semi-analytical models of $G(s)$ and $D(s)$ using different means than the ones presented in this thesis. These are constructed from the mathematical definition of $G(s)$ and $D(s)$, one proposing an analytical *Ansatz* which takes into account the deformation of the vortex core with velocity, and the other method directly integrating the magnetization vector field from MMS, to obtain an expression of $G(s)$ and $D(s)$ that is not influenced by the errors in the other terms of the TEA. These results, developed by Colin Ducarme during his master thesis, will be the subject of a future publication [151].

3.2 Periodic double-polarity reversals

After obtaining the results presented in the previous Section using the same geometry as in Chapter 2, *i.e.*, $(R, h) = (100, 10)$ nm, the next question was whether other aspect ratios could be investigated. For larger diameters, vortex dynamics differ because the confinement weakens, the core occupies a smaller relative area, and the amplitude of the AOF grows with the radius of the structure. To validate the generalization of our data-driven approach to free layers with larger diameters, we thus conducted simulations to calibrate the Thiele equation terms, as described in Section 3.1. At low currents, the new geometry exhibited expected behavior. However, upon increasing the current density, we encountered an unusual regime, wherein the vortex core becomes trapped between two orbits due to polarity reversals. These findings are reported in the following Section.

In the previous Chapter, we have seen that the vortex core gyrotropic motion is intrinsically linked to its polarity and chirality, with the polarity determining the sense of gyration [54], while the chirality induces a splitting of the dynamical properties [99]. Moreover, the polarity reversal process has attracted considerable interest from several research groups, that have proposed various methods for controlling it. The vortex polarity can be reversed through the application of various magnetic fields, including static [152,153], pulsed [137,154,155,156], or oscillating OOP fields [157,158,159], as well as oscillating [160] or rotating [161] in-plane fields. Additionally, spin-polarized currents, such as in-plane ac [162,163] or pulsed currents [164] and OOP dc currents [165], can also trigger polarity reversals. Depending on the excitation mechanism employed, multiple polarity reversals may occur [137,162,164], as observed in nanocontacts where a periodic polarity reversal is driven by an input dc current [166,167]. These reversals manifest as self-sustained oscillations that can evolve into chaotic dynamics, presenting potential applications in secure communications [166].

Within a nanocontact geometry, the Ampère-Oersted field promotes the formation of a magnetic vortex, causing its chirality to align parallel to the AOF. However, in an STVO, the initial chirality can be deterministically set [98], enabling the study of its influence on the periodic reversal process. In Chapter 2, we concluded that two distinct regimes [79] arise based on the vortex chirality and polarity, the polarizer orientation, and the input current density, following the conditions $JPp_z < 0$ and $|J| \geq |J_{c1}|$. Those are the resonant regime, where the vortex core damps back to the magnetic dot center, and the auto-oscillating regime, in which the vortex reaches a stable orbit [see Figure 3.6 a)]. In this Section, we present a third prospective regime [166], illustrated in Figure 3.6 b) & c). When the vortex core reaches an upper threshold orbit, it undergoes a polarity reversal process. This initial polarity switch is promptly followed by a second reversal, leaving the vortex core at a lower orbit s_{min}, transitioning back to the auto-oscillating regime. As this double-reversal process is both periodic and sustained, the vortex core becomes confined between these two boundary orbits. We show that this third regime, termed the "confinement regime", is exclusively triggered for a vortex exhibiting negative chirality. For a positive chirality, we will see that the lower angular frequency of the vortex core prevents it from reaching a critical velocity before collapsing on the edge of the free layer, thus preventing confinement.

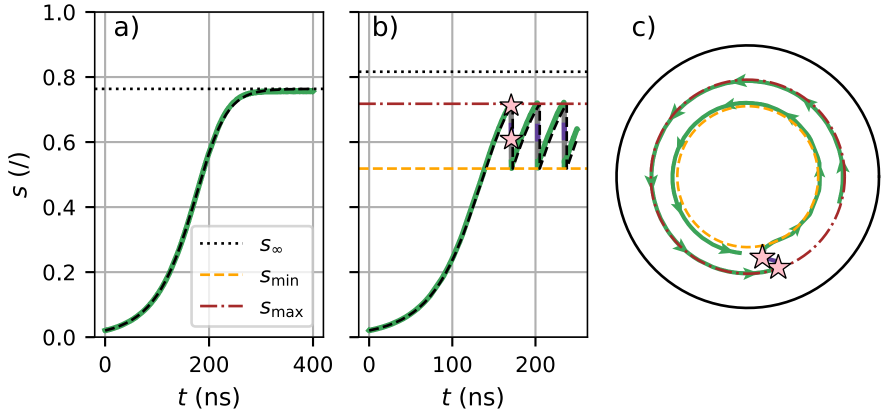

Figure 3.6: a) Evolution of the reduced vortex core position $s(t)$ in the steady-state regime saturating at s_∞ for $J = -5.0 \times 10^{10}$ A/m^2. The dashed line is the prediction using Equation (3.14). b) Evolution of $s(t)$ in the confinement regime with $J = -6.0 \times 10^{10}$ A/m^2. The trajectory is plotted in green (purple) for a positive (negative) polarity. The black dashed line is the estimation of $s(t)$ using Equation (3.16). Pink stars indicate polarity reversals. c) Trajectory of the vortex core inside the magnetic dot while in the confinement regime. The vortex core motion direction is represented by arrows. When the polarity is negative, the gyration sense is reversed. Adapted from Ref. [148].

3.2.1 Methods

As already done, the vortex dynamics are investigated using micromagnetic simulations, using mumax^3. The free layer, with radius $R = 500$ nm and thickness $h = 9$ nm, is discretized into cells of $2.5 \times 2.5 \times 4.5$ nm^3. This specific geometry was selected because our partners at INL (Braga, Portugal), specialized in fabricating STVOs, had obtained spin-diode curves for these wide vortices, data we could help interpret using our models [168]. Apart from these changes, the material and polarizer parameters are the same as in Chapter 2, and MMS are still conducted at $T = 0$ K, without applied external magnetic field. Here, however, the vortex polarity is set to $P = +1$. A negative input current density is then applied, ranging from 0 to -10×10^{10} A/m^2, with the Ampère-Oersted field generated by the current incorporated as an external magnetic field. For such system, the STVO frequency is between 60 MHz and 120 MHz, depending in the vortex chirality C and the current density J. The reduced vortex core position $s(t) = \|\mathbf{X}\|/R$, where

X is the vortex core position, was extracted from MMS in the auto-oscillating regime and fitted using the toy-model presented in Section 3.1:

$$s(t) = \frac{s_i}{\sqrt{\left(1 + \frac{s_i^2}{\alpha/\beta}\right) e^{-2\alpha t} - \frac{s_i^2}{\alpha/\beta}}}, \tag{3.14}$$

with s_i the initial vortex core position and the two parameters α and β that are functions of the input current density J. To predict $s(t)$ for a given J, the parameters $\alpha(J)$ and $\beta(J)$ are linearly fitted as $\alpha(J) = a_J J + a$ and $\beta(J) = b_J J + b$ when the vortex core is in the auto-oscillating regime (see Table 3.3). Additionally, the stable orbit s_∞ is defined by

$$s_\infty = \sqrt{-\frac{\alpha(J)}{\beta(J)}}, \tag{3.15}$$

as derived from Equation (3.14) for $t \to \infty$.

Constant	C^+	C^-
a_J $\left(\times 10^{-4}\text{ Hz m}^2/\text{A}\right)$	−12.49	−6.26
b_J $\left(\times 10^{-4}\text{ Hz m}^2/\text{A}\right)$	8.81	5.42
a (MHz)	−13.47	−12.75
b (MHz)	3.00	−4.74

Table 3.3: Dynamical parameters of the considered system [see Equation (3.14)], for both C^+ and C^- configurations.

To predict the $s(t)$ evolution in the resonant regime, the values of s_{min} and s_{max} are required, along with the four following hypotheses:

1. The vortex polarity is reversed if $s \geq s_{\text{max}}$,
2. A second polarity reversal always follows,
3. The double reversal process is instantaneous,
4. Post-reversals, $s = s_{\text{min}}$.

Combining Equation (3.14), these assumptions, and the J-dependent expressions of α, β, s_{min}, and s_{max} enables the prediction of $s(t)$ for any current density, as shown in Figure 3.6 b). It gives the following recursive equation:

$$s_n = \begin{cases} \dfrac{s_{n-1}}{\sqrt{(1+\frac{s_{n-1}^2}{\alpha/\beta})e^{-2\alpha\Delta t}-\frac{s_{n-1}^2}{\alpha/\beta}}}, & \text{if } s_{n-1} < s_{\max}, \\ s_{\min}, & \text{if } s_{n-1} \geq s_{\max}, \end{cases} \tag{3.16}$$

where Δt is the time step, and s_n and s_{n-1} are the current and previously calculated vortex core position, respectively.

3.2.2 Leaky integrate-and-fire behavior

Both chiralities C^+ and C^- configurations are studied (see Figure 3.7), while taking into account the Ampère-Oersted field $\mathbf{H}^{\mathrm{Oe}}$. The chirality-dependent evolution of the stable orbit s_∞ with respect to the current density J is predicted using Equation (3.14). The first critical current J_{c1} is determined by $\alpha(J_{c1}) = 0$, resulting in $J_{c1} = -a/a_J$. This yields $J_{c1,C^+} = -1.08 \times 10^{10}$ A/m^2 for positive chirality, and $J_{c1,C^-} = -2.04 \times 10^{10}$ A/m^2 for negative chirality.

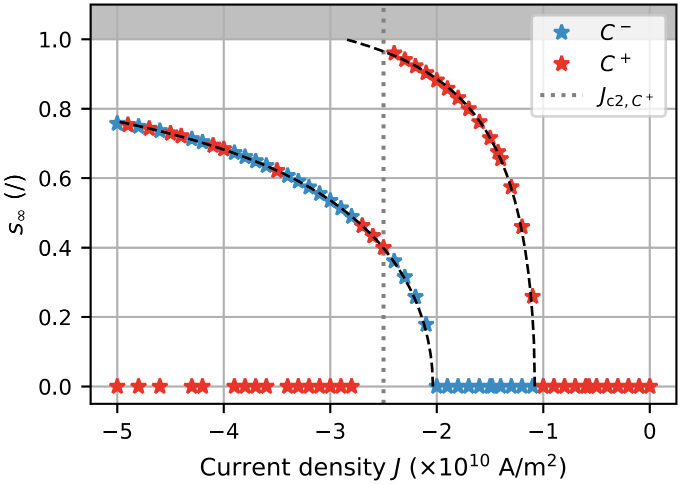

Figure 3.7: Stable orbit s_∞ with respect to the current density J, for an initial negative (blue stars) or positive (red stars) chirality. The second critical current J_{c2,C^+} is indicated by a dashed gray line. For an initial positive chirality, the vortex core reaches the magnetic dot edges for $|J| \geq |J_{c2,C^+}|$, with $J_{c2,C^+} \approx -2.5 \times 10^{10}$ A/m^2. Its chirality is then reversed to $C = -1$ and the vortex core polarity is either unchanged, leading to a steady-state regime similar to the one of a vortex with an initial negative chirality, or reversed, resulting in a resonant regime. The black dashed lines are the predictions of $s_\infty(J)$, from Equation (3.15). Adapted from Ref. [148].

For $|J_{c1}| \leq |J| \leq |J_{c2}|$, where J_{c1} and J_{c2} are the first and second critical currents, respectively, the vortex lies in the steady-state regime. The confinement regime is uniquely observed for vortices presenting a negative chirality C^-. For an initial positive chirality C^+, if $|J| > |J_{c2,C^+}|$, the vortex chirality reverses to C^- upon core expulsion from the nanodot, aligning parallel to the Ampère-Oersted field induced by the current.

Consequently, the dynamics of the resulting vortex mimic those of an initially C^- one, leading to overlapping final orbits s_∞, similarly to what was presented in Section 2.1. However, a polarity reversal may also come along the chirality switch, violating the $JPp_z < 0$ condition and causing a transition back to the resonant regime. In such event, the vortex core relaxes towards the center of the nanodot, to reach $s_\infty = 0$.

For a vortex with a negative chirality, when $|J| \geq |J_{conf}|$, with $J_{conf} \approx -5.1 \times 10^{10}$ A/m^2, the vortex reaches its critical velocity at the orbit radius $s = s_{max}$. This triggers a polarity reversal process through the well-established mechanism involving the creating and annihilation of a vortex-antivortex pair [135,165]. Indeed, as the core velocity increases, it undergoes deformation, developing a dip of opposite out-of-plane magnetization (see Figure 3.8).

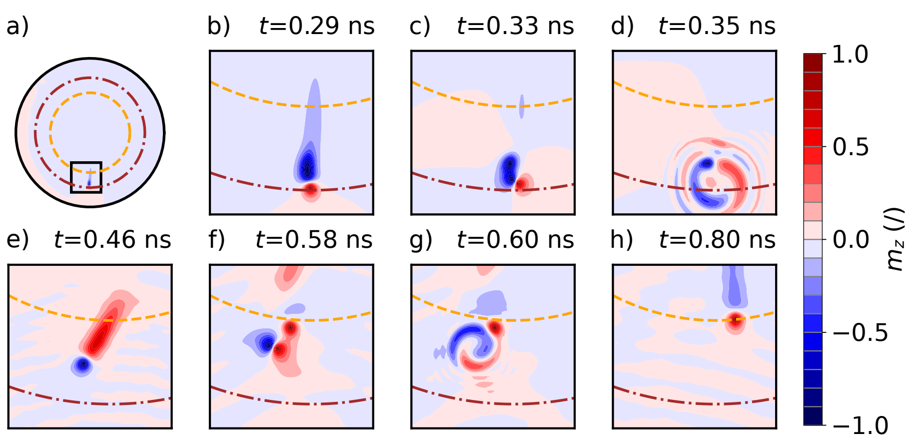

Figure 3.8: a)-h) Evolution over time of the out-of-plane magnetization component m_z during a double polarity reversal. a) View of the entire magnetic dot, with the boundary orbits s_{min} and s_{max} represented by the dashed orange line and the dashed-dotted brown line, respectively. b)-h) Enlarged view of the area close to the vortex core, outlined by the black box in a). Adapted from Ref. [148].

At s_{max}, the vortex core reaches a velocity of 285 m/s, which aligns with the theoretical critical velocity [139,169] (in cgs units) $v_{cr} = \nu\gamma\sqrt{A} = 302 \pm 32$ m/s, with $\nu = 1.66 \pm 0.18$ and γ the gyromagnetic ratio. At the critical velocity [139], the dip amplitude matches that of the vortex core, facilitating polarity reversal *via* vortex-antivortex pair dynamics (see Figure 3.8). The excess of exchange energy is subsequently dissipated through spin-wave (SW) generation [170]. Following this first reversal, the vortex polarity becomes negative. The latter enters thus the resonant regime and relaxes towards its equilibrium position. A second polarity reversal is then observed as the new dip again reaches the same amplitude as the vortex core, followed by further spin-wave generation. We acknowledge that the physical origin of this second reversal remains unclear, as the critical velocity is not attained in this case. We suspect that spin-waves emitted after the first reversal might interact with the core, inducing another switch. Further investigations are needed to confirm this hypothesis. Despite this uncertainty, the phenomenon is robust, even in simulations (not shown here) with a tilted polarization direction and thermal noise. At the end of this second reversal, the vortex core is located at s_{min} and enters again in the auto-oscillating regime. This double reversal process occurs periodically, leading to a sustained confinement regime characterized by s_{min} and s_{max}, that define the lower and upper limits of the vortex core position, respectively, as well as the frequency f^{conf} at which the double polarity reversals occur (see Figure 3.9).

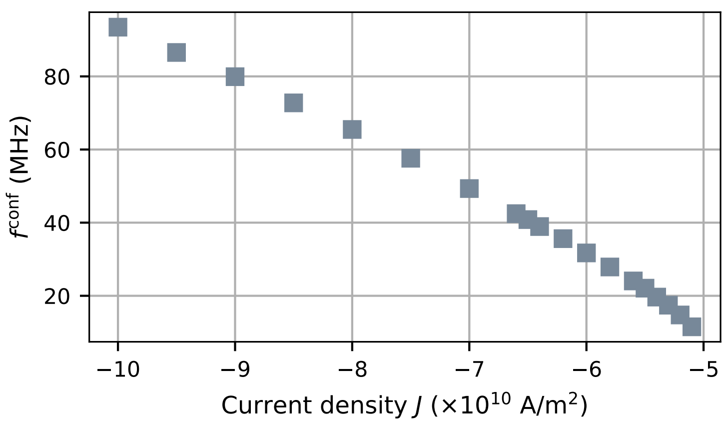

Figure 3.9: Confinement frequency f^{conf}, *i.e.*, the inverse of the period between double-polarity reversals, with respect to the current density J. Adapted from Ref. [148].

The s_{min} and s_{max} orbits decrease as the amplitude of J increases, as shown in Figure 3.10. Indeed, the dip reaches the same amplitude as the vortex core at a lower orbit when $|J|$ increases. The elapsed time between successive double-reversals is extracted and the corresponding confinement frequency f^{conf} is displayed in Figure 3.9. This frequency increases with $|J|$, meaning that the latter can be controlled by the input dc current, with confinement frequencies ranging from 11.5 MHz at -5.1×10^{10} A/m^2, up to 93.5 MHz at -10.0×10^{10} A/m^2. Since spin-waves are generated at each reversal, the period between SW generation can also be tuned by J.

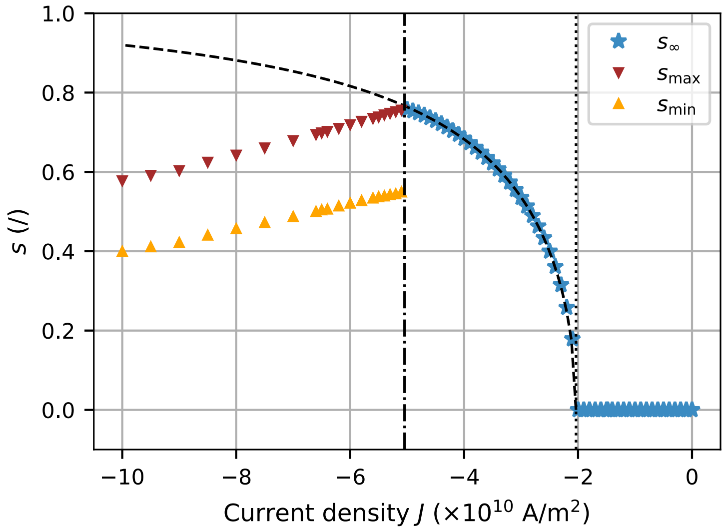

Figure 3.10: Evolution of the stable orbit s_∞, threshold orbit s_{max}, and reset orbit s_{min} with respect to the current density J. The black dashed line is the prediction of $s_\infty(J)$, from Equation (3.15). The dotted and dashed-dotted lines are J_{c1} and J_{conf}, respectively. Adapted from Ref. [148].

Apart from sending simple dc currents into the STVO, more complex waveforms, such as pulse trains, can be fed into it to obtain richer dynamics. Upon injecting a train of 30 ns current pulses of magnitude $J = -6.5 \times 10^{10}$ A/m^2, instead of a constant current into the STVO, the vortex core is progressively excited to a larger oscillating orbit s (see Figure 3.11).

If the interpulse interval remains large, the vortex core relaxes during the off-periods of the duty cycle, preventing any significant event. Conversely, when the pulses are temporally close, the vortex core reaches the threshold orbit s_{max}, triggering a firing event after leaking and integration, as in a biological neurons (see Chapter 1). Subsequently, the system resets to a lower orbit s_{min}, and the process reiterates. However, the reset step in this system is imperfect, as the vortex core position returns only to s_{min} rather than $s = 0$. To address this, a bias current can be introduced such that $s(J_{\mathrm{bias}}) = s_{\mathrm{min}}$, with additional current pulses modulating the dynamics range between s_{min} and s_{max}. However, this approach would render the system continuously active, substantially increasing its power consumption. Additionally, it should be noted that the leaking time constant during current-free periods in the cycle is directly linked to the Γ-parameter introduced in Section 2.1 and can thus be tuned accordingly.

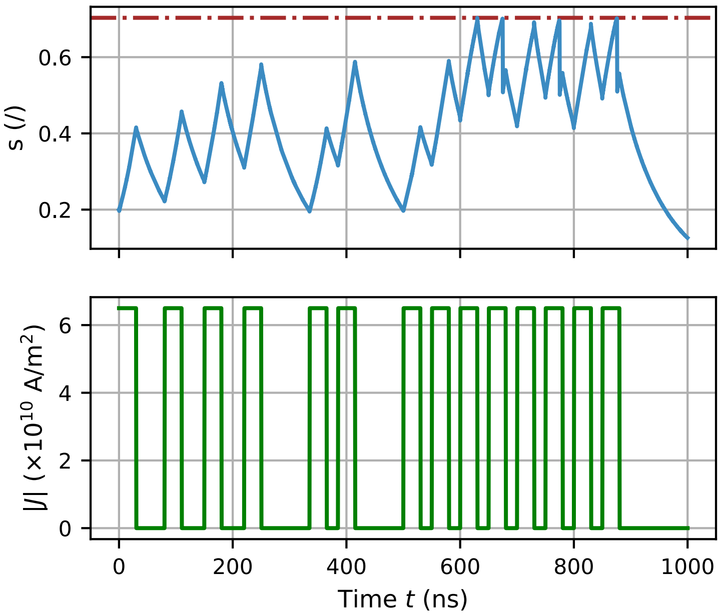

Figure 3.11: Leaky integrate-and-fire behavior in an STVO. When current pulses are spaced apart in time, the vortex core is excited to a larger orbit $s(t)$ (*integration*) and relaxes during the off periods of the duty cycle (*leaking*). If the pulses are injected close enough however, the vortex core reaches s_{max} (brown dashed-dotted line) and a double-polarity reversal is triggered (*firing event*), with the vortex returning to the s_{min} position.

Typically, achieving this type of LIF behavior with conventional CMOS technologies requires adding a capacitor to the circuit, which is often of significant size [171]. In our case, a single compact component performs nearly all the functions required for a LIF circuit, offering potential advantages. To date, however, no experimental evidence supports the emergence of a confinement regime in nanopillar STVOs. If our hypothesis that the second polarity reversal arises due to spin-wave generation after the first reversal is confirmed, we believe that low-temperature experimental conditions would be beneficial to observe it, due to reduced thermal noise.

3.3 Conclusion

In Section 3.1, we have enhanced the Thiele equation model proposed in Section 2.1 with data-driven corrections to the gyrotropic and damping terms. These adjustments were derived by fitting our model predictions to mumax^3 results. The resulting hybrid DD-TEA accurately computes STVO dynamics for abritrary current inputs, demonstrating strong agreement with micromagnetic simulations in both transient and steady-state regimes. Moreover, our novel method exhibits approximately a six orders of magnitude acceleration over MMS. In its fastest version, our second-order truncated toy-model, this factor is increased by another 100 times, at the cost of additional assumptions. These advancements enable practical long-duration signal simulations, facilitating functionalization of STVOs for prospective applications. Furthermore, we believe that our data-driven approach is generalizable to other magnetic textures (*e.g.*, skyrmions) or oscillators, provided their dynamics can be described by the Thiele equation and experimental data or simulation results can be gathered to refine certain analytical terms.

In Section 3.2, while we aimed at applying our method to larger diameter vortices, we found a particular regime in which the vortex core stays confined between boundary orbits due to successive reversals of the vortex core polarity. We have shown that the vortex core dynamics in both auto-oscillating and confinement regime can be analytically described by fitting MMS results. The emergence of the confinement regime depends on the chirality and the magnitude of J. By modulating the latter, one can control the parameters of the confinement regime, specifically s_{min}, s_{max}, and f^{conf}, offering the potential to fine-tune the properties of the confinement regime as well as the spin-wave generation. Notably, the confinement regime exhibits nonlinear and periodic dynamics, making it potentially valuable for neuromorphic computing applications [111]. In this context, the vortex remains in a transient state, never achieving a stable orbit, which is similar to a leaky integrate-and-fire neuronal behavior. Here, the integration and leaking properties are controlled by the input current density, while the firing events correspond to the vortex core polarity reversals.

Chapter's take-home message

- Both the **Thiele equation approach** (TEA) and **micromagnetic simulations** (MMS) present **shortcomings**, either in terms of **accuracy or computational resources**, respectively.
- We propose the **data-driven Thiele equation approach**, a semi-analytical model **calibrated by micromagnetic simulation** results, to improve the gyrotropic and damping terms in auto-oscillating regime.
- In its fastest form, this method is up to **eight orders of magnitude faster than MMS**, while providing **equivalent accuracy** in frequency and orbit of precession predictions, enabling its use for practical applications.
- By applying our method to nanopillars of larger radii, **periodic double-polarity reversals** were observed, when simply applying a **dc current without any external magnetic field**.
- This behavior is similar to the **leaky integrate-and-fire** model of biological neurons, or could also be used as a **periodic and tunable source of spin-waves** through vortex-antivortex annihilation.

4

Towards close-packed oscillator systems

In previous Chapters, we have considered a system consisting of a single oscillator isolated from external influences. However, for practical implementations and prospective applications, such as rf signal processing [18,172], neuromorphic computing [19,20], or solving optimization problems through Ising machines [21,173,174], inter-STVO communication could be beneficial to increase transmission power and spectral purity for instance. One of the ultimate milestones in the field would be to fabricate dense oscillator networks coupled through their emitted dipolar fields without requiring internode electrical connections. These networks would exploit these emitted fields without requiring an intricate nanofabrication of all-to-all metallic contacts. However, existing studies overlook the Ampère-Oersted field radiated by these nanopillars, which becomes influential for their neighbors at high current densities and close proximity, as detailed hereafter. As mentioned in Chapter 2 for the internal contribution of the AOF, the latter inevitably comes along the OOP current used to trigger the gyrotropic motion, thus necessitating its careful consideration for accurate modeling.

In Section 4.1, we detail thoroughly the impact of an irradiated Ampère-Oersted field on a closely positioned STVO. Although we make significant assumptions to analytically describe its influence, we show that our Zeeman contribution term is readily integrable into Thiele equation-based models. Additionally, the simulations performed in this Chapter validate consistently our analytical calculations, but also provide supplementary insights to prior works on vortices under in-plane magnetic fields. This work, carried out within the Neuromorphic Engineering Group in collaboration with Prof. Flavio Abreu Araujo and Anatole Moureaux, also results from discussions with Dr. Tristan da Câmara Santa Clara Gomes (INESC-MN, Portugal), as well as Dr. Chloé Chopin and Dr. Ursula Ebels (SPINTEC, France). A manuscript related to these outcomes is in preparation.

4.1 Adjacent Ampère-Oersted field

Among the methods facilitating interactions between STVOs, simple electrical connections emerged as widely preferred due to their straightforward implementation. This approach eased the study of various synchronization phenomena [20,175,176,177,178,179,180,181], notably valuable for probing the physics of exceptional points [182,183]. Furthermore, following the efforts to construct dense arrays of oscillators for prospective on-chip implementations, significant attention has been dedicated to exploring magneto-dipolar interactions between STVOs positioned at sub-micrometer distances, both theoretically [85,91,120,127,184,185,186,187] and experimentally [121,188]. With advancements in nanofabrication techniques, the placement of oscillators in close proximity (< 200 nm) while ensuring individual top contacts has become achievable, thereby allowing for the selective manipulation of their dynamics [127,188]. In any case, at such close distances, the influence exerted by one oscillator upon its neighbors becomes important.

Presently, research efforts have focused on investigating dipole-dipole interactions between vortices. In this study, we aim at exploring the effects of an external Ampère-Oersted field on the dynamics of an oscillator. This investigation builds upon the first Chapters of this thesis and other past reports [99,100] dealing with the impact of the internal Ampère-Oersted field generated when a current is injected into STVOs or in nanocontact geometries [107], which influences their dynamics and deforms the magnetic texture. Although rf field lines exploiting Ampère's law have been positioned above STVOs in previous works [183], a thorough description of the influence of the Ampère-Oersted field generated by an oscillator on its nearby neighbors has yet to be given, to the best of our knowledge. In the present study, we aim at deriving an analytical expression for the Zeeman energy associated with the Ampère-Oersted field coming from an external source. Subsequently, we will compare these results to micromagnetic simulations, clarifying valuable phenomena crucial for developing future applications involving STVO lattices.

4.1.1 Methods

The basic building block for studying close-range interactions between adjacent oscillators is a pair of two magnetic tunnel junctions, as depicted in Figure 4.1. The latter are separated by a distance d and are considered to be perfectly circular cylinders of radii R_1 and R_2. Using individual top contacts, these devices can be driven by independent current densities J_1 and J_2. To simplify our analysis, two major assumptions are made. The latter are allowed because the combination of multiple magnetic fields fulfills the principle of superposition. Firstly, one of the STVOs (the one on the right in Figure 4.1) is considered to be a simple conducting nanowire of infinite length emitting an Ampère-Oersted field, meaning that its magnetization is completely neglected. Then, the Ampère-Oersted field emitted by the STVO that is actually considered is not taken into account, while its gyrotropic mode of dynamic oscillations of the vortex core, orbiting at an in-plane position $\mathbf{X} = (X, Y)$, or (ρ, φ) in polar coordinates, is indeed excited by a current density J_1.

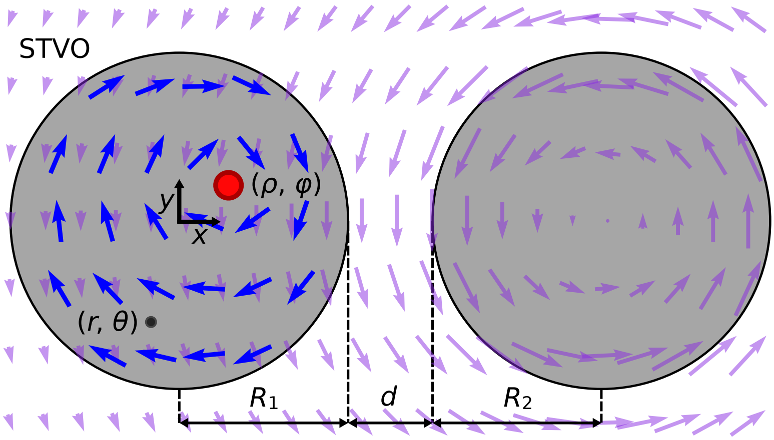

Figure 4.1: Schematic top view of a pair of oscillators, separated by a distance d. The in-plane vortex magnetization field $\mathbf{M}$ of the STVO on the left (with radius R_1) is depicted by the blue arrows, while the Ampère-Oersted field $\mathbf{H}^{\mathrm{Oe}}_{\mathrm{ext}}$ emitted by the adjacent STVO (with radius R_2), which is simplified as a simple metallic nanopillar, under a current density J_2 is indicated by the purple arrows. As a spin-polarized current J_1 is injected into the STVO, the vortex core (highlighted in red) gyrates at a position (ρ, φ), in polar coordinates. All points in the plane (in dark gray) are denoted using a vector $\mathbf{r} = (r, \theta)$.

Hence, the Zeeman contribution to the total magnetic energy of the STVO is given as

$$W^{\mathrm{Oe}}_{\mathrm{ext}} = -\mu_0 \int_V \mathbf{M} \cdot \mathbf{H}^{\mathrm{Oe}}_{\mathrm{ext}} \mathrm{d}V, \tag{4.1}$$

where $\mathbf{M}$ is the vortex magnetization field, $\mathbf{H}^{\mathrm{Oe}}_{\mathrm{ext}}$ the Ampère-Oersted field generated by the metallic line, and V the volume of the STVO free layer. To proceed with the calculations, mathematical descriptions of both the magnetization and magnetic fields are needed. We use the two-vortex *Ansatz* for the magnetization distribution $\mathbf{M} = M_s\left(m_x, m_y, m_z\right)$. On the other hand, the expression for the Ampère-Oersted field can be derived from Ampère's law. While the metallic nanopillar is crossed by a uniform current density J_2, the magnitude of the generated field at any point in space $\mathbf{r} = r(\cos(\theta), \sin(\theta))$ outside the field-emitting nanopillar is given as

$$H_{\text{ext}}^{\text{Oe}}(\mathbf{r}) = \frac{|J_2|}{2} R_2^2 \frac{1}{\|\mathbf{r} - \mathbf{D}\|}, \tag{4.2}$$

where $\mathbf{D} = \left(R_1 + d + R_2, 0\right)$ is the center position of the field line. Thus, the Ampère-Oersted magnetic vector field is $\mathbf{H}_{\text{ext}}^{\text{Oe}} = H_{\text{ext}}^{\text{Oe}}(\mathbf{r})(\cos(\phi), \sin(\phi))$, where the angle ϕ corresponds to

$$\phi = \frac{\pi}{2}(1 + \sigma) + \arctan\left(\frac{\zeta - \eta\cos(\theta)}{\eta\sin(\theta)}\right). \tag{4.3}$$

In this equation, σ indicates the sign of J_2, informing on whether the current flows towards $\pm z$. Additionally, the dimensionless variables ζ and η are equal to $\left(R_1 + d + R_2\right)/R_1$ and r/R_1, respectively. While converting Equation (4.1) into cylindrical coordinates and assuming a uniform vortex magnetization along the z-direction, which is valid for thin free layers [78], we obtain

$$\begin{aligned} W_{\text{ext}}^{\text{Oe}} = &-\frac{\mu_0}{2}|J_2| M_s h_1 R_1 R_2^2 \\ &\times \int_0^{2\pi}\int_0^1 \eta \frac{m_x\cos(\phi) + m_y\sin(\phi)}{\sqrt{\zeta^2 - 2\zeta\eta\cos(\theta) + \eta^2}} \mathrm{d}\eta\mathrm{d}\theta, \end{aligned} \tag{4.4}$$

where the integration is performed over the cross-section of the STVO free layer. Regrettably, this complex integral lacks a direct analytical solution. In the context of vortex dynamics, two common approaches are employed in such case, *i.e.*, a numerical integration is performed or a McLaurin series is used prior integration to derive an approximate analytical solution [78,125]. We will carry out both methods to compare their outcomes.

Let us first process with the purely analytical series expansion method. As stated, since the expressions of m_x and m_y depend on the reduced position of the vortex core [see Equations (1.20) & (1.21)], *i.e.*, $s(\cos(\varphi), \sin(\varphi))$, the integrand must be expanded into a McLaurin series around a centered vortex core position to solve it (see Appendix C for details). After performing this first step, one can integrate the resulting polynomial expression for each point **r** contained in the STVO free layer, where $\eta \in [0, 1]$ and $\theta \in [0, 2\pi]$. Therefore, the fully analytical expression for the Zeeman energy attributed to the Ampère-Oersted field induced by an oscillator, *i.e.*, the metallic nanowire in this case, on its neighbor is given by

$$\begin{aligned}
W^{\mathrm{Oe}}_{\mathrm{ext,theo}} = -\frac{\mu_0}{2} C J_2 h_1 M_\mathrm{s} R_1 R_2^2 \pi
&\times \Bigg(\left(\frac{2}{3}\frac{s}{\zeta} - \frac{2}{15}\frac{s^3}{\zeta} - \frac{2}{105}\frac{s^5}{\zeta} - \frac{2}{315}\frac{s^7}{\zeta} \right) \cos(\varphi) \\
&+ \left(\frac{4}{15}\frac{s^2}{\zeta^2} - \frac{8}{105}\frac{s^4}{\zeta^2} - \frac{4}{315}\frac{s^6}{\zeta^2} \right) \cos(2\varphi) \\
&+ \left(\frac{16}{105}\frac{s^3}{\zeta^3} - \frac{16}{315}\frac{s^5}{\zeta^3} - \frac{32}{3465}\frac{s^7}{\zeta^3} \right) \cos(3\varphi) \\
&+ \left(\frac{32}{315}\frac{s^4}{\zeta^4} - \frac{128}{3465}\frac{s^6}{\zeta^4} \right) \cos(4\varphi) \\
&+ \left(\frac{256}{3465}\frac{s^5}{\zeta^5} - \frac{256}{9009}\frac{s^7}{\zeta^5} \right) \cos(5\varphi) \\
&+ \frac{512}{9009}\frac{s^6}{\zeta^6} \cos(6\varphi) + \frac{2048}{45045}\frac{s^7}{\zeta^7} \cos(7\varphi) + O\left(s^8\right) \Bigg). \qquad (4.5)
\end{aligned}$$

Notably, the parameter σ no longer appears explicitly in the expression since $\sigma |J_2| = J_2$. As $(s/\zeta)^n \ll 1$ for large n since $s < 1$, it should be noted that high-order terms contribute minimally to the Zeeman energy.

A more direct approach involves a numerical integration of Equation (4.4), for various s and φ values. Subsequently, one can fit these results $W^{\mathrm{Oe}}_{\mathrm{ext,num}}$ to an expression similar to Equation (4.5), which gives

$$\begin{aligned}
W^{\mathrm{Oe}}_{\mathrm{ext,fit}} = -\frac{\mu_0}{2} C J_2 h_1 M_\mathrm{s} R_1 R_2^2 \pi
&\times \Bigg(\left(0.669\frac{s}{\zeta} - 0.151\frac{s^3}{\zeta} \right) \cos(\varphi) \\
&+ \left(0.269\frac{s^2}{\zeta^2} - 0.090\frac{s^4}{\zeta^2} \right) \cos(2\varphi)
\end{aligned}$$

$$+0.124\frac{s^3}{\zeta^3}\cos(3\varphi)+0.080\frac{s^4}{\zeta^4}\cos(4\varphi)\Bigg). \tag{4.6}$$

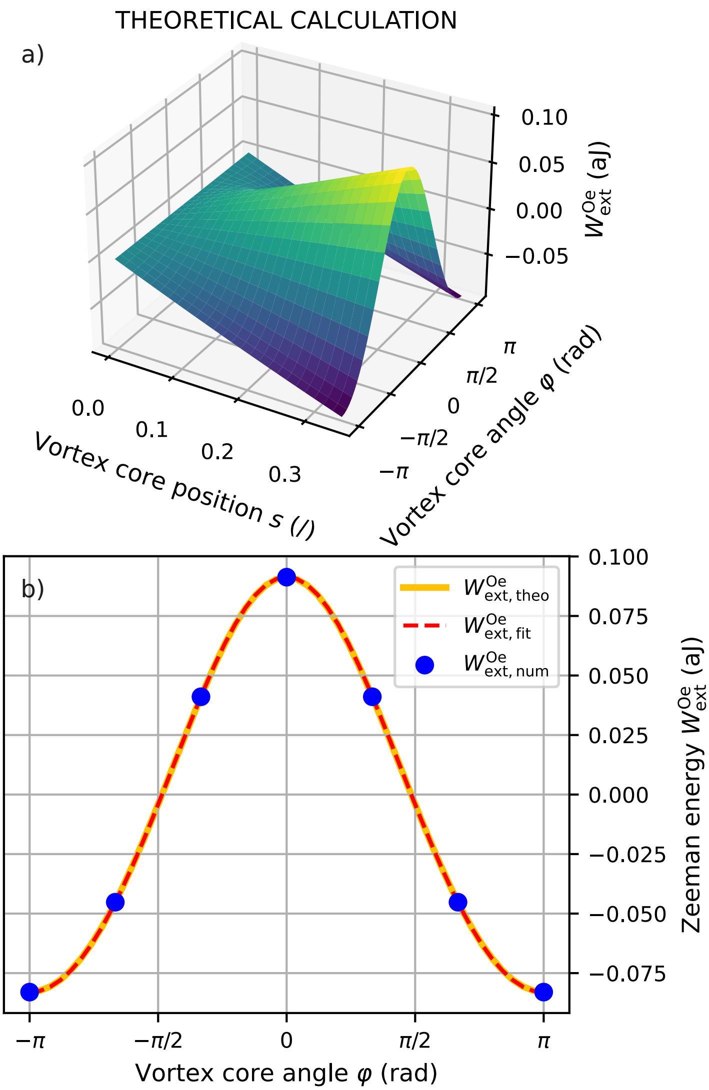

Figure 4.2: Zeeman energy calculated for the same simulation parameters as those given in Section 4.1.2. a) Numerical integral $W_{\text{ext,num}}^{\text{Oe}}$ as a function of the vortex core position s and angle φ, calculated from Equation (4.1). b) Comparison between values predicted by the numerical integral $W_{\text{ext,num}}^{\text{Oe}}$ and the analytical formulae $W_{\text{ext,theo}}^{\text{Oe}}$ and $W_{\text{ext,fit}}^{\text{Oe}}$ (see Equations (4.5) & (4.6), respectively), at an orbit $s = 0.3$.

A strong agreement between the analytical and numerical coefficients is observed. Such concordance was expected, within the margin given by the error term in the McLaurin series and the slightly simpler form proposed for the fitting expression, *i.e.*, limited to the fourth-order. Plots of the integrals are depicted in Figure 4.2 a) & b), up to a moderate vortex core excitation. Only seven data points are shown (in blue) in Figure 4.2 b), for the sake of clarity, while the fit is performed on a 51×51 grid. Due to symmetry considerations, it was expected that the energy $W_{\text{ext}}^{\text{Oe}}$ is zero if $s = 0$, as evidenced by the absence of constant term in Equation (4.5). Moreover, the shape of the potential well suggests that the position of lowest energy does not correspond to a vortex core located at the center of the free layer. As elaborated below, it appears that the Zeeman energy falls below its value for a centered core, *i.e.*, $W_{\text{ext}}^{\text{Oe}} = 0$, for a range of angular values φ.

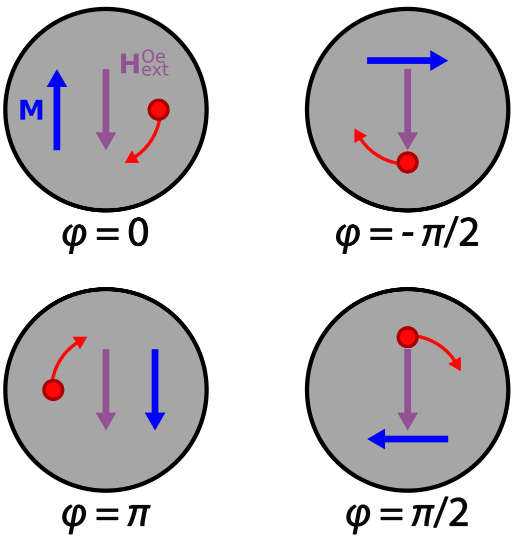

Figure 4.3: Schematic depiction of the mean magnetization **M** (in blue) and mean Ampère-Oersted field $\mathbf{H}_{\text{ext}}^{\text{Oe}}$ (in purple) in the STVO at various vortex core positions. The mean magnetization direction is perpendicular to the displacement of the vortex core from the center of the free layer. In this specific scenario, the chirality as well as the polarity of the vortex are negative, and the current J_2 injected to generate the Ampère-Oersted field follows the $+z$-direction. In steady-state, while excited by a spin-polarized current J_1, the vortex core (in red) gyrates in the clockwise direction and successively crosses the positions $(s, 0)$, $\left(s, -\frac{\pi}{2}\right)$, (s, π), $\left(s, \frac{\pi}{2}\right)$, modifying the value of the Zeeman energy $W_{\text{ext}}^{\text{Oe}}$ accordingly.

As per Equations (4.5) & (4.6), the Zeeman energy is near-zero when the vortex core intersects the $x = 0$ line, corresponding to $\varphi = \pm\pi/2$. Conversely, when φ attains 0 or π, the energy reaches its maximum absolute value for each specific orbit s. At these points, the distinction between a minimum and a maximum of energy is determined by the chirality and rotational direction of the external Ampère-Oersted field, given by the factor $-J_2C$, every other parameters being positive. These observations can be understood through a macrospin approximation for a displaced vortex core. Indeed, one should recall that the vortex core is in a dynamic oscillation regime due to the injection of a spin-polarized current into the MTJ. The situation is shown on Figure 4.3, illustrating the four angles of interest. Here, we consider the Ampère-Oersted field intercepted by the STVO as quasi-uniform to facilitate understanding. When the vortex core is located at $\pm\pi/2$, the average magnetization $\langle \mathbf{m}(\mathbf{r}) \rangle_V = -2/3C\big(\mathbf{e}_z \times \mathbf{X}\big)/R$ solely exhibits a component along the x-direction [88]. Since the Ampère-Oersted field aligns with the y-axis, the scalar product between the two vectors of Equation (4.1) becomes null. Conversely, when the vortex core is situated on the $y = 0$ line, the scalar product attains its maximum absolute value, following a similar rationale. Once more, it is worth noting that the sign of this product is contingent uniquely upon the factor $-C\sigma$.

4.1.2 Stationary field and offset equilibrium

Once again, the micromagnetic simulations are carried out with mumax^3. A pair of similar adjacent nanopillars of radii $R_1 = R_2 = 100$ nm, separated by a distance $d = 50$ nm, are investigated in this study. Achieving such a close edge-to-edge distance has been previously demonstrated experimentally [189]. The STVO, presenting a thickness $h_1 = 10$ nm, is actually simulated, whereas the nanowire is represented solely by the Ampère-Oersted field it emits. As introduced previously, this approach aims at isolating the impact of the field, disregarding the dipole-dipole interactions already studied in previous works [85,91,120,127,186,187]. In the STVO, a current is injected for a total duration of 2 µs. Initially, its magnitude stands at 6.6×10^{10} A/m^2 and linearly decreases over time to reach 5.0×10^{10} A/m^2. Such progressive reduction in current density enables the exploration of a wide range of vortex core positions. Meanwhile, a constant current density of 7.0×10^{10} A/m^2 is applied into the nanowire. Both currents are injected in the positive z-direction. All other simulation parameters are identical to those employed in the other Chapters.

Since mumax^3 internally computes the position of the vortex core and the corresponding Zeeman energy over time, constructing a plot of $W^{\mathrm{Oe}}_{\mathrm{ext,simu}}$ as a function of the core position is straightforward, as given in Figure 4.4 a). The shape of the energy landscape is consistent with the theoretical predictions outlined by Equations (4.5) & (4.6) and Figure 4.2 a).

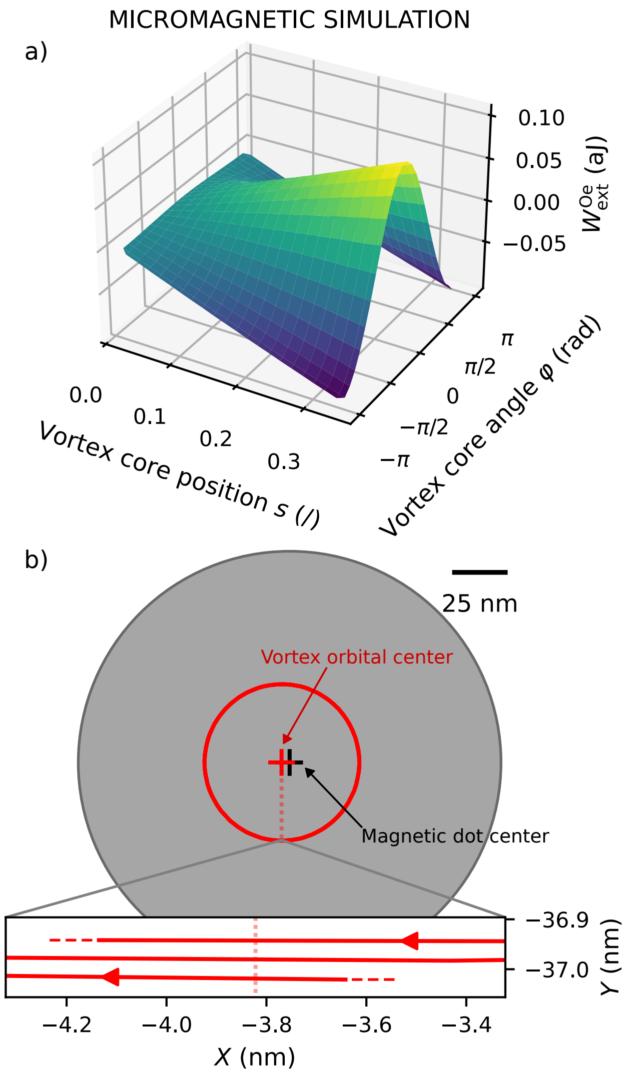

Figure 4.4: a) Zeeman energy $W_{ext,simu}^{Oe}$ as a function of the vortex core position s and angle φ, extracted from micromagnetic simulations. b) Top view of the circular magnetic dot (STVO) of radius $R_1 = 100$ nm, its center being represented by the black cross. The trajectory (X, Y) of the vortex core is shown in red, for $t \in [400, 404]$ ns. The red cross corresponds to the final coordinates $(X_f, Y_f) \approx (-3.8, 0)$ nm of the vortex core, when there is no longer any current J_1. The inset shows a zoom on the decreasing amplitude of the vortex core trajectory over two oscillations, as the current density decreases linearly with time.

In fact, upon comparing the theoretical forecasts with MMS outcomes, remarkable agreement is observed. Numerically calculating a relative error value between simulations and theory is challenging, due to the fact that the curves pass through zero. Hence a dimensionless absolute error, defined as

$$\mathrm{err} = \left| \frac{W^{\mathrm{Oe}}_{\mathrm{ext,simu}} - W^{\mathrm{Oe}}_{\mathrm{ext,theo}}}{-\frac{\mu_0}{2} J_2 C M_s h_1 R_1 R_2^2 \pi} \right|, \tag{4.7}$$

was adopted. The error across simulation points ranges from 8×10^{-8} and 1×10^{-2} and averages 4×10^{-3}. Histograms (not shown here) reveal that the error is generally minimized when the vortex core angle approaches π, while the theoretical predictions tend to deviate the most at an angle of $\pi/2$. The observed discrepancies between simulations and theory are attributed to the simplifications made for analytical derivations, notably the OOP magnetization omission in the vortex core, and the deformation of the magnetic texture induced by the Ampère-Oersted field, as discussed in Section 2.2. Additionally, it is intriguing to observe the sparsity of simulation data at $s = 0$ [see Figure 4.4 a)], even for low injected currents. As a matter of facts, the available points showcasing $s = 0$ correspond solely to a φ angle close to zero. This phenomenon is corroborated by Figure 4.4 b), illustrating the vortex core trajectory $\mathbf{X} = (X, Y)$. It is apparent that the final core position does not align with the geometric center of the dot, but instead settles at $X = -3.8$ nm. In other terms, this outcome suggests that the equilibrium position of the vortex core is not at $s = 0$, but rather that the latter orbits around $(-3.8, 0)$ nm.

Notably, this result reproduces the behavior observed when a uniform in-plane field is applied to an STVO such as in hysteresis loops [5,190,191]. This phenomenon can be understood through the Thiele equation approach. We introduced in previous Chapters that one of the forces acting on the vortex core originates from the derivative of the magnetic energy. Typically, these restoring forces are directed exclusively towards the geometrical center of the free layer, as seen in Section 2.2. In other words, the stiffness parameters associated with other sources of magnetic energy, *e.g.*, exchange, magnetostatic, depend solely on the oscillation radius s and are independent from the phase φ. In our case, the axisymmetry is broken due to the external Ampère-Oersted field, resulting in a force vector $\mathbf{F}^{\mathrm{Oe}}_{\mathrm{ext}}$ oriented towards the negative x-direction (for the parameters utilized in our simulation). This force, derived from Equation (4.5) as

$$\mathbf{F}_{\mathrm{ext}}^{\mathrm{Oe}} = -\frac{\partial W_{\mathrm{ext}}^{\mathrm{Oe}}}{\partial \mathbf{X}}, \tag{4.8}$$

explains why, at the end of the simulation, even if the current injected into the STVO is insufficient to generate auto-oscillations, the equilibrium position of the vortex core is displaced from the geometrical center of the free layer. Finally, this force derivation can be easily compared, at the first-order at least, to the expression obtained for a uniform in-plane magnetic field, given as $\mathbf{F}^{\mathrm{Z}} = \mu(\mathbf{e}_z \times \mathbf{H})$, with $\mu = 2\pi/3\mu_0 C h_1 M_s R_1$ [88].

From Equation (4.8), we can estimate the final vortex core position, considering an equilibrium of forces between the AOF and the restoring forces generated by the other magnetic energy contributions. At first-order, this yields the linearized equation:

$$X_{\mathrm{f}} \approx \frac{\frac{\mu_0}{2} C J_2 h_1 M_s R_2^2 \frac{2\pi}{3\zeta}}{k_0^{\mathrm{ex}} + k_0^{\mathrm{ms}}}, \tag{4.9}$$

resulting in $X_{\mathrm{f}} \approx -3.1$ nm for the parameters given previously, a value consistent with simulation results. Its underestimation probably arises from the discrepancies between analytical magnetic stiffness and simulation results, discussed in Section 2.2. In fact, if we rather use the stiffness parameters k_0^{ex} and k_0^{ms} retrieved from MMS, we find $X_{\mathrm{f}} \approx -3.6$ nm.

4.1.3 Core trajectory in ferromagnetic resonance

This displacement of the vortex core induced by the Ampère-Oersted field, even in the absence of a sufficient injected current in the STVO to generate excitation, prompts consideration of other conceivable cases where the generated field is no longer static but alternating, similarly to ferromagnetic resonance experiments [82,83,88,96,192,193]. Such a field can be easily achieved by injecting an ac current into the field line. We will examine two different situations. Firstly, an ac field whose frequency increases linearly with time will be imposed, allowing us to showcase resonance phenomena. Then, sinusoidal magnetic fields of constant amplitude and frequency will be considered to gain insight into the trajectory of the vortex core. In both cases, no current is injected into the STVO, which operates in a passive manner. All other simulation parameters remain consistent with those previously reported. As introduced above, a field with a time-varying frequency can be examined. In this case, the current density injected into the metallic nanowire is given as

$$\begin{aligned} J_2 &= J_{\mathrm{rf}} \sin\left(2\pi f^{\mathrm{rf}}(t)t\right) \\ &= J_{\mathrm{rf}} \sin\left(2\pi \frac{900\times 10^6}{20\times 10^{-6}}\frac{t^2}{2}\right), \end{aligned} \tag{4.10}$$

which corresponds to a linear evolution of frequency from 0 to 900 MHz over 20 µs. Implementing such a demanding frequency slew rate experimentally with existing signal generators would inevitably be challenging. The aim here is to maintain a reasonable simulation time, while ensuring that the frequency sweep is slower than the intrinsic dynamics.

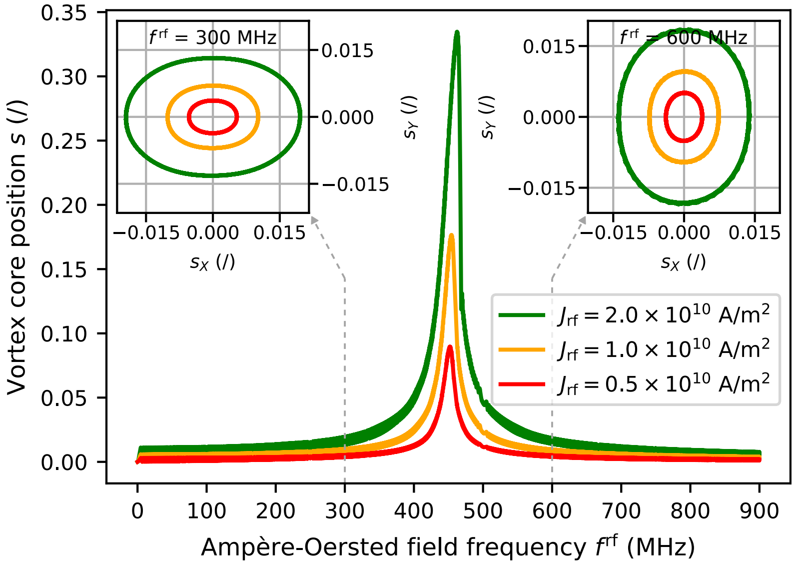

Figure 4.5: Vortex core position s in the STVO with respect to the frequency f^{rf} of the input Ampère-Oersted field, for different values of current injected into the field line. The insets display the elliptical in-plane trajectories of the vortex core $(s_X, s_Y) = (X, Y)/R$ at those same currents, for additional micromagnetic simulations where the frequency stays fixed at 300 and 600 MHz. No current is injected into the STVO, which operates passively in resonance.

Figure 4.5 illustrates the evolution of the amplitude of dynamic oscillations relative to the origin in the STVO over time, referred to here as the vortex core position to simplify, at different currents $J_{\mathrm{rf}} = 0.5,\ 1.0,$ and 2.0×10^{10} A/m^2. A resonance peak can be identified, reaching $s \approx 0.34$ for the largest current imposed. Notably, the instantaneous frequency of the magnetic field at this juncture, *i.e.*, 450 MHz, aligns with the eigenfrequency of this oscillator, as we reported in Section 2.1 (using the same simulation parameters, without magnetic field). However, it is worth noting that the orbit attained for a sinusoidal field at the resonance frequency is considerably larger than the static displacement under a given field value [see Figure 4.4 b)], despite the lower amplitude of the ac current in the nanowire compared to the former dc excitation. If the magnetic field amplitude was further increased, the vortex core could be expelled [139,194]. At the lowest frequencies, the magnetic field is quasistationary. Consequently, we revert to a situation similar to that in Section 4.1.2, where the vortex core is displaced by a quasi-uniform planar field, with the amplitude of this field determining the extent of the displacement. Finally, we observe a broadening of the core position signal, *i.e.*, $s = \|\mathbf{X}\|/R$, due to the elliptical trajectories, which imply that the amplitude of the orbit can vary even in steady-state.

Additionally, the frequency of the input signal can be regarded as a method for adjusting the ellipticity of the vortex core trajectory [96], as extensively studied by Lee & Kim (for linearly and circularly polarized oscillating magnetic fields) [195,196]. At the lowest frequencies, the regime is quasistationary, analogously to the behavior observed in a hysteresis curve. In other words, the vortex core moves linearly along a straight line perpendicular to the field direction. At intermediate frequencies, the trajectory becomes elliptical (see inset of Figure 4.5), with the minor axis of the ellipse expanding as the resonant frequency is approached. Lee & Kim attribute the elliptical trajectory observed under linearly polarized oscillating fields to the superposition of two circular eigenmotions, one clockwise and the other counterclockwise, presenting asymmetric amplitudes [196]. The relative phase between these eigenmodes, notably determined by the magnetic field frequency, accounts for the elliptical motion and explains the elongation reversal of the ellipse. Upon reaching the resonance frequency, circular gyrotropic behavior is reinstated, and the oscillation amplitude reaches its maximum. However, in our case, the trajectory is not perfectly circular, as the magnetic field is not uniform. It should also be noted that, as already described in detail in other studies [192,197], the asymmetry of the resonance curves increases with the amplitude of the excitation, due to nonlinear effects.

Finally, one should observe that the gyration frequency of the vortex core remains perfectly synchronized with the input signal across the entire explored frequency range, as evidenced by a Fourier spectrum (FFT) of the vortex core trajectory in Figure 4.6. As expected, a linear frequency evolution is observed, matching with the excitation signal used. Partial harmonic synchronizations are also evident [195,198], albeit with significantly lower power spectral density. Additionally, resonance is distinctly identifiable halfway through the simulation, as a broadband response can be observed. These additional peaks are caused by the transient motion of the vortex core before reaching steady-state regime, and higher-order effects [195]. It corresponds to an AOF frequency of approximately 450 MHz, which is consistent with the eigenfrequency obtained in Chapter 2.

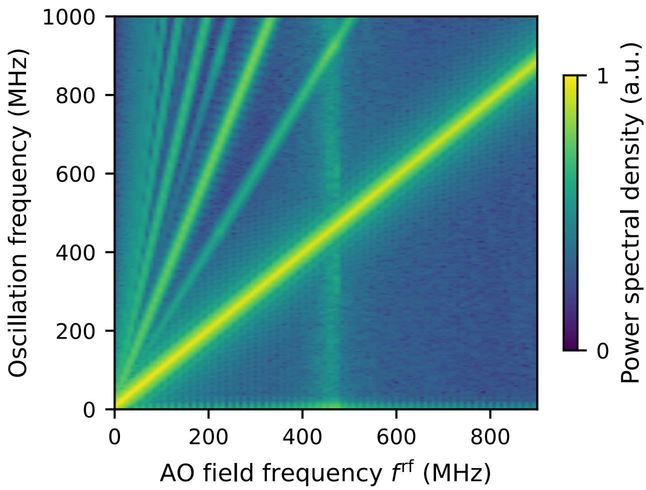

Figure 4.6: Fourier spectrum of the vortex core coordinate signal $\mathbf{X} = (X, Y)$. The magnetic vortex in the STVO is excited by the rf Ampère-Oersted (AO) field generated by the metallic nanowire ($J_2 = 2 \times 10^{10}$ A/m^2), with a frequency f^{rf} linearly increasing from 0 to 900 MHz over 20 µs.

4.2 Discussions and conclusion

So far, our analysis has been limited to a single STVO-metallic wire pair. To extend our findings to a chain [127,187], or an array [91,180] of STVOs, it should be reminded that magnetic fields obey the principle of superposition. Depending on the relative positioning of the STVOs in pairs, the Equations (4.5) & (4.6) can be modified to account for different situations. In practice, this entails introducing a phase shift to the angle φ. These analytical terms would be of particular interest when considering arrays of oscillators interacting at short distances (< 200 nm) without electrical interconnections, relying instead on their emitted fields. Using common top and bottom contacts to ease fabrication, the STVOs could be positioned even closer to one another, forming networks made up of a large number of electrically-tunable magnets in architectures similar to spin-glass systems. Furthermore, our results could also elucidate the emergence of small-amplitude oscillations in the orbit signal when considering a chain of three oscillators [127]. This effect could be attributed to a decentering of the gyrotropic motion, similar to the phenomenon discussed in Section 4.1.2. Additionally, Section 4.1.3 explores resonance behaviors which could hold promise for applications involving extremely localized-scale microwave frequency recognition [18,113]. Indeed, the voltage measured across the STVO is contingent upon the average magnetization within its free layer, which in turn is influenced by the orientation of the elliptical path of the vortex core dictated by the frequency of the input signal.

Furthermore, it seems important to emphasize that the dipolar interaction between the vortices was neglected for reasons discussed earlier. In practice, this dipolar field should dominate the interaction and synchronization phenomena [199]. However, it is worth noting that the Ampère-Oersted field is not negligible, as the dipolar field H^{dip} scales with d^{-3}, whereas the Ampère-Oersted field H^{Oe} is inversely proportional to d. This could make the Ampère-Oersted field relatively significant for intermediate distances. For instance, for the parameters given in Section 4.1.2, the amplitude of the Ampère-Oersted field emitted is of 4.40 mT at the edge of the metallic nanowire, 1.76 mT at the center of the STVO free layer, and still showcases a value of 0.88 mT at 500 nm of the nanowire center. In comparison, the exact value of the stray dipolar field emitted by a ferromagnetic disk depends on the displacement of the vortex core relative to the nanodot center [199]. This means that, for a relatively low current J_1 (typically if J_1 is below the first critical current for sustained auto-oscillations, and therefore $s \ll 1$), the Ampère-Oersted and dipolar fields could be of the same order of magnitude.

It is also worth mentioning that our simplified configuration, even if it has limited applicability without a dipolar field induced by a second vortex for practical devices, could prove useful for future applications to replace the rf antenna that is usually placed on top of the oscillators [113,183,198]. Such alternative could provide a number of advantages, including the fact that the generated field is completely contained in the plane, or for imaging the free layer using techniques such as MOKE or X-ray microscopy [200,201,202,203]. Lastly, it is crucial to note that our study has exclusively focused on homogeneous currents. In more realistic cases or experiments, geometry and fabrication imperfections often lead to inhomogeneous current distributions within the free layer [17,203,204]. Consequently, the Ampère-Oersted field induced by these currents deviates from the idealized, simplified case. It should also be mentioned that the Ampère-Oersted field could perhaps be used to induce synchronization between oscillators, provided that its amplitude is large enough. These aspects warrant further investigation in future studies.

In summary, the influence of a local external Ampère-Oersted field emitted by a simple conducting nanowire on an adjacent STVO has been thoroughly investigated. An analytical expression for the Zeeman energy associated with this field has been derived and validated through simulations. Subsequently, the effect of an oscillating Ampère-Oersted field was explored, revealing resonance phenomena and illustrating the impact of the excitation field frequency on the trajectory of the vortex core. These findings hold potential for future applications involving dense oscillator networks, such as neuromorphic computation, frequency detection, or rf signal generation.

Chapter's take-home message

- For prospective on-chip integration, investigating **dense oscillator networks** is necessary. **Prior studies** have predominantly focused on the close-range **dipolar interactions** between STVOs, neglecting their irradiated Ampère-Oersted field.
- We derive analytically the **Zeeman energy related to an adjacent Ampère-Oersted field** undergone by an STVO, making the strong assumption that it is generated by a simple metallic nanowire.
- The derived expression is **validated through micromagnetic simulations**, revealing an oscillation orbit **offset from the geometrical center** of the nanopillar when dc currents are applied, as for uniform in-plane fields.
- The **passive operation** of the STVO under a **time-varying AOF** highlights vortex core **resonance** phenomena, which adopts a **distorted elliptical trajectory** whose aspect ratio depends on the field frequency.

Conclusion and perspectives

DESPITE extensive analytical, micromagnetic, and experimental research in past decades, the dynamics of spin-torque vortex oscillators remain a challenging open field of study. Their strongly nonlinear behavior is particularly difficult to predict, due to the numerous influencing parameters and the intrinsic complexity of nonuniform magnetic textures, such as vortices. This theoretical thesis focuses on the precise refining of analytical models based on the Thiele equation for magnetic vortex dynamics. Through analytical calculations, consistently validated through micromagnetic simulations, we provide a comprehensive analysis of some terms of these models, including the Ampère-Oersted field induced by the current injected into the STVO.

Specific findings

In Chapter 2, we developed a fully analytical model based on the Thiele equation approach, improving both the magnetostatic and Zeeman-like Ampère-Oersted terms commonly found in existing literature. This model, analogous to a Gilbert-damped harmonic oscillator driven by spin-transfer, revealed a clear chirality-dependent splitting of the dynamics, in both resonant and steady-state regimes, arising from the relative orientation between the vortex in-plane magnetization and the Ampère-Oersted field induced by the current. These findings were validated through micromagnetic simulations. However, while the model provides accurate predictions in the resonant regime, its applicability remains only qualitative in the auto-oscillating steady-state regime. Building on these limitations, we provided a method to extract vortex stiffness parameters from simulations, using the magnetic energy terms, displaying significant deviations between analytical and numerical results. These discrepancies partially account for the challenge to achieve quantitative accuracy with the TEA model. Furthermore, our analysis demonstrated that the vortex stiffness varies with the applied current amplitude, even for the exchange and magnetostatic contributions. Such behavior is attributed to a distortion of the vortex magnetization by the Ampère-Oersted field, which consequently impacts the dynamics.

Another limitation of the fully analytical TEA model lies in the assumption that the gyrotropic and damping terms remain constant, independently of the vortex core position. Given the challenge of calculating these terms purely analytically, we adopted an alternative approach in Chapter 3. By using steady-state micromagnetic results, we adjusted these terms to achieve quantitative accuracy in the auto-oscillating regime, even for the transient dynamics. This data-driven Thiele equation approach combines the computational efficiency of an analytical model, requiring only two equations per time step, while matching the accuracy of MMS. Through mathematical optimizations, we developed a second model that is approximately eight orders of magnitude faster than MMS and eliminates the need to solve ordinary differential equations for calculating the dynamics. We demonstrated that this model accurately predicts the vortex core position, even under arbitrary waveforms injections. When applying our method to larger radius free layers, we discovered an intriguing oscillation regime where the vortex stays confined between two orbits due to successive double-polarity reversals. Remarkably, the vortex behavior in this regime aligns with the leaky integrate-and-fire model, a simple framework describing biological neuron dynamics.

While the first two Chapters considered isolated oscillators, the final Chapter explored a scenario where STVOs are placed in close proximity. Existing theoretical and experimental studies on interactions between pairs of oscillators primarily focus on synchronization through dipolar coupling. However, the influence of the Ampère-Oersted generated by an STVO on its neighbor is often overlooked. Chapter 4 thus investigated this Zeeman term in detail, considering a simplified case where one of the oscillators is replaced by a nonmagnetic metallic nanowire. We derived an analytical expression for the Zeeman magnetic energy and validated it through micromagnetic simulations, demonstrating strong agreement. Furthermore, we showed that the Ampère-Oersted field shifts the equilibrium position of the vortex core, akin to the effect of a uniform in-plane field. Finally, when the STVO operates passively in resonance, we confirmed that its elliptical trajectory can be tuned by adjusting the frequency of the ac current injected into the field line, despite a spatial gradient in magnetic field amplitude.

Limitations and perspectives

Certainly, every theoretical work relies on assumptions that distance it from experimental results, and this thesis is no exception. Furthermore, we solely relied on mumax^3 simulations. Cross-validating our results against alternative micromagnetic solvers under identical parameter sets could further enhance confidence in our findings. In any case, hardware systems are far more complex thant the simplified cases studied here. For instance, spin-torque nano-oscillator stacks actually consist of more than just three layers [188], and their geometry is imperfect due to nanofabrication constraints. Additionally, the considered perpendicular polarizer direction, though facilitating gyrotropic excitation of the vortex core, is impractical in experiments because it generates almost no TMR signal. A different polarization direction would have required adding terms in the model [86], which could shift equilibrium position. Furthermore, other sources of nonidealities such as the fringing field from the polarizer [59], defects and pinning sites [190,191,205,206,207,208], or temperature and thermal noise significantly influence the dynamics. Given the strong nonlinearity of magnetic vortices, we chose to vary parameters individually to avoid complicated multi-factorial interpretations. The goal was not a perfectly complete model, but rather to propose keys to understanding experimental results, one step at a time.

Another aspect of my work is the systematic integration of the Ampère-Oersted field into models and simulations, based on two main hypotheses; first, that it behaves as generated from an infinite and perfect cylinder (though real nanopillars are finite and slightly conical), and second, that the current density is uniform across the pillar. However, since we are dealing with a tunnel junction where the free layer presents a nonuniform vortex magnetization, electron scattering could actually vary depending on the precise location inside the dot, leading to nonuniform current densities [209]. This, as well as skin effects and tunneling hotspots, could induce field oscillations worth exploring in future works. Additionally, as mentioned in Chapter 3, this thesis does not account for bias magnetic fields, either in-plane [5] or out-of-plane [86], which play a crucial role in experiments. The same rationale holds for dipolar interactions when STVOs are placed in close proximity, as their stray fields influence adjacent elements.

Furthermore, we propose that future experimental setups could be designed to help validate the results of each individual Chapters of this thesis, particularly those in Chapter 4, which were disregarded until now, hidden by dipolar effects. Another promising direction for future works would be developing a data-driven model based on experimental rather than MMS data, to achieve more realistic results. Prospective strategies include linking TMR signals directly to vortex core positions, although no quantitative equation exists for this purpose, or using Kerr microscopy and X-ray techniques to observe in real-time the free layer magnetization [210]. This would, though, require advanced experimental developments, notably regarding the electrical contact design.

Clearly, the dynamics of magnetic vortices within free layers of magnetic tunnel junctions remain incompletely understood, offering vast theoretical and experimental opportunities for future works. Moreover, we strongly believe that the data-driven techniques developed in this thesis for predicting the nonlinear magnetization dynamics are applicable to other types of oscillators or magnetic solitons.

Appendices

A The harmonic oscillator equation

OUR harmonic oscillator dynamics is described by the following homogeneous system of first-order differential equations

$$\dot{\mathbf{X}} = \bar{\bar{\mathbf{\Omega}}}\mathbf{X}, \tag{A.1}$$

where the matrix $\bar{\bar{\mathbf{\Omega}}}$ is given as

$$\bar{\bar{\mathbf{\Omega}}} = \begin{bmatrix} \Gamma & -\omega \\ \omega & \Gamma \end{bmatrix}. \tag{A.2}$$

Assuming Γ and ω to be constant in time, one can derive time-dependent solutions for the vortex core position $\mathbf{X} = (X(t), Y(t))$. Such assumption is verified in a steady-state regime of oscillations. The eigenvalues $\lambda_{1,2}$ of the system are calculated from its characteristic equation

$$\lambda^2 - 2\Gamma\lambda + \left(\Gamma^2 + \omega^2\right) = 0, \tag{A.3}$$

the latter being obtained from $\det\left(\bar{\bar{\mathbf{\Omega}}} - \lambda\mathbb{I}\right) = 0$. The two solutions of Equation (A.3) are $\lambda_{1,2} = \Gamma \pm i\omega$. Using Euler's formula, one can prove that the coordinates of the vortex core are given as

$$X(t) = e^{\Gamma t}\left[\left(C_1 + C_2\right)\cos(\omega t) + i\left(C_1 - C_2\right)\sin(\omega t)\right], \tag{A.4}$$

$$Y(t) = e^{\Gamma t}\left[-i\left(C_1 - C_2\right)\cos(\omega t) + \left(C_1 + C_2\right)\sin(\omega t)\right]. \tag{A.5}$$

If the two constants are fixed as $C_1 = -C_2 = -\frac{i}{2}\|\mathbf{X}\|$, one finally obtains

$$\begin{bmatrix} X(t) \\ Y(t) \end{bmatrix} = \|\mathbf{X}\| \, e^{\Gamma t} \begin{bmatrix} \sin(\omega t) \\ -\cos(\omega t) \end{bmatrix}. \tag{A.6}$$

B Bernoulli differential equation

THE Equation (3.11) is an ordinary differential equation of the Bernoulli type. As a reminder, it is written as follows:

$$\dot{s}(t) = \alpha s(t) + \beta s(t)^3. \tag{B.1}$$

One can easily separate the variables s and t on each side of the equation, before integrating them both,

$$\int \frac{1}{\alpha s + \beta s^3} \mathrm{d}s = \int \mathrm{d}t, \tag{B.2}$$

which gives, assuming that $\alpha + \beta s^2$ is positive,

$$\frac{\ln(s)}{\alpha} - \frac{\ln\left(\alpha + \beta s^2\right)}{2\alpha} = t + C_1, \tag{B.3}$$

where we introduced C_1, a constant of integration. If we combine the logarithms together, we can simplify this expression to

$$\ln\left(\frac{s}{\sqrt{\alpha + \beta s^2}}\right) = \alpha\left(t + C_1\right), \tag{B.4}$$

where both sides of the equation can be raised to exponentials and then squared, to give

$$\frac{s^2}{\alpha + \beta s^2} = C_2^2 e^{2\alpha t}, \tag{B.5}$$

in which we have introduced a new constant $C_2 = e^{\alpha C_1}$. A general solution to this equation is

$$s(t) = \sqrt{\frac{\alpha C_2^2 e^{2\alpha t}}{1 - \beta C_2^2 e^{2\alpha t}}}, \tag{B.6}$$

the negative one being excluded since $s > 0$ by definition. Here, one can use the particular solution to this equation when $t = 0$, where a value s_i can be set as the initial orbit. Substituting into the previous equation, we obtain

$$s_i = \sqrt{\frac{\alpha C_2^2}{1 - \beta C_2^2}}, \tag{B.7}$$

which allows to calculate the value of the constant C_2^2:

$$C_2^2 = \frac{s_i^2}{\alpha + \beta s_i^2}. \tag{B.8}$$

Finally, if one plugs this constant into the Equation (B.6), we find the expression that describes the evolution of s with t, after some simplification steps:

$$s(t) = \frac{s_i}{\sqrt{\left(1 + \frac{s_i^2}{\alpha/\beta}\right) e^{-2\alpha t} - \frac{s_i^2}{\alpha/\beta}}}. \tag{B.9}$$

C External Ampère-Oersted field Zeeman energy

LET us resume from Equation (4.4), which gives the Zeeman energy for a magnetic vortex, contained in a free layer of radius R_1 and thickness h_1, intercepting an Ampère-Oersted field emitted by a nearby metallic nanowire of radius R_2 crossed by an OOP current density J_2:

$$W_{\text{ext}}^{\text{Oe}} = -\frac{\mu_0}{2}|J_2|M_s h_1 R_1 R_2^2 \times \int_0^{2\pi}\int_0^1 \eta \underbrace{\frac{m_x \cos(\phi) + m_y \sin(\phi)}{\sqrt{\zeta^2 - 2\zeta\eta\cos(\theta) + \eta^2}}}_{\Psi} \mathrm{d}\eta\mathrm{d}\theta. \tag{C.1}$$

Even if one neglects the OOP magnetization of the vortex core and considers the in-plane magnetization $\left(m_x, m_y\right)$ defined by the two-vortex *Ansatz* [see Equations (1.20) & (1.21)], this integral presents no analytical solution. As explained in Chapter 4, one way to solve this issue is to compute a McLaurin series of the expression Ψ for a vortex core close to the geometric center of the free layer, *i.e.*, a Taylor expansion around $s = 0$. Such a series, developed arbitrarily up to order 8, is given as

$$\Psi = \sum_{n=0}^{7} K_n s^n + O\left(s^8\right), \tag{C.2}$$

where the coefficients K_n must be determined to perform the integration. Since the integral of K_0 equals zero, let us proceed with an example using K_1 to illustrate the method, the latter being the same for higher-order terms, with more complicated expressions. The first-order coefficient K_1 is

$$K_1 = \frac{\Psi^{(1)}(s=0)}{1!} = -\frac{C\zeta\left(\eta^2 - 1\right)\sigma\sin(\theta)\sin(\theta - \varphi)}{\eta(\zeta^2 + \eta^2 - 2\zeta\eta\cos(\theta))}. \tag{C.3}$$

For reasons of mathematical stability in $\eta = 0$, the use of Cartesian coordinates is actually preferable to polar coordinates. By transforming $(\eta, \theta) \to \left(\eta_x, \eta_y\right)$ and simplifying, we obtain

$$K_1 = \frac{C\zeta\sigma\eta_y\left(\sin(\varphi)\eta_x - \cos(\varphi)\eta_y\right)\left(\eta_x^2 + \eta_y^2 - 1\right)}{\left((\zeta - \eta_x)^2 + \eta_y^2\right)\left(\eta_x^2 + \eta_y^2\right)^{\frac{3}{2}}}. \tag{C.4}$$

Since s is a parameter of Ψ and not a variable, it leaves only the integral of K_1 to solve, which presents the following analytical solution:

$$s\int_{-1}^{1}\int_{-\sqrt{1-\eta_x^2}}^{+\sqrt{1-\eta_x^2}} K_1 \mathrm{d}\eta_y \mathrm{d}\eta_x = \frac{2}{3}\frac{s}{\zeta} C\sigma\pi\cos(\varphi) \tag{C.5}$$

We therefore conclude that, at the first-order, the Zeeman energy is equal to

$$W_{\mathrm{ext}}^{\mathrm{Oe}} = -\frac{\mu_0}{2} C J_2 M_{\mathrm{s}} h_1 R_1 R_2^2 \pi \left(\frac{2}{3} \frac{s}{\zeta} \cos(\varphi) + O\left(s^2\right) \right), \tag{C.6}$$

where we simplified $\sigma \left| J_2 \right| = J_2$, as σ indicates the direction of the current. To obtain the higher-order coefficients K_n, the exact same procedure can be applied. The full resulting expression is given in Equation (4.5).

Bibliography

[1] S. Dinicola, F. D'Anselmi, A. Pasqualato, S. Proietti, E. Lisi, A. Cucina, and M. Bizzarri, *A systems biology approach to cancer: fractals, attractors, and nonlinear dynamics*, *OMICS: A Journal of Integrative Biology* **15**, 93-104 (2011).

[2] L. Brus, *Quantum crystallites and nonlinear optics*, *Applied Physics A* **53**, 465-474 (1991).

[3] Y. Ming, and V. Ramaswamy, *Nonlinear climate and hydrological responses to aerosol effects*, *Journal of Climate* **22**, 1329-1339 (2009).

[4] W.-M. Liu, B. Wu, and Q. Niu, *Nonlinear effects in interference of Bose-Einstein condensates*, *Physical Review Letters* **84**, 2294 (2000).

[5] K. Y. Guslienko, V. Novosad, Y. Otani, H. Shima, and K. Fukamichi, *Field evolution of magnetic vortex state in ferromagnetic disks*, *Applied Physics Letters* **78**, 3848-3850 (2001).

[6] K. L. Metlov, and K. Y. Guslienko, *Stability of magnetic vortex in soft magnetic nano-sized circular cylinder*, *Journal of Magnetism and Magnetic Materials* 1015-1017 (2002).

[7] R. Hertel, *Vortex states à la carte*, *Nature Nanotechnology* **8**, 318-320 (2013).

[8] A. Vansteenkiste, J. Leliaert, M. Dvornik, M. Helsen, F. Garcia-Sanchez, and B. Van Waeyenberge, *The design and verification of MuMax3*, *AIP Advances* **4**, 107133 (2014).

[9] A. A. Thiele, *Steady-State Motion of Magnetic Domains*, *Physical Review Letters* **30**, 230-233 (1973).

[10] A. A. Thiele, *Applications of the gyrocoupling vector and dissipation dyadic in the dynamics of magnetic domains*, *Journal of Applied Physics* **45**, 377-393 (1974).

[11] X. Chen, F. Abreu Araujo, M. Riou, J. Torrejon, D. Ravelosona, W. Kang, W. Zhao, J. Grollier, and D. Querlioz, *Forecasting the outcome of spintronic experiments with Neural Ordinary Differential Equations*, *Nature Communications* **13**, 1016 (2022).

[12] J. A. Katine, F. J. Albert, R. A. Buhrman, E. B. Myers, and D. C. Ralph, *Current-driven magnetization reversal and spin-wave excitations in Co/Cu/Co pillars*, *Physical Review Letters* **84**, 3149 (2000).

[13] S. I. Kiselev, J. C. Sankey, I. N. Krivorotov, N. C. Emley, R. J. Schoelkopf, R. A. Buhrman, and D. C. Ralph, *Microwave oscillations of a nanomagnet driven by a spin-polarized current*, *Nature* **425**, 380-383 (2003).

[14] A. N. Slavin, and V. S. Tiberkevich, *Nonlinear Auto-Oscillator Theory of Microwave Generation by Spin-Polarized Current*, *IEEE Transactions on Magnetics* **45**, 1875-1918 (2009).

[15] Z. Zeng, G. Finocchio, B. Zhang, P. K. Amiri, J. A. Katine, I. N. Krivorotov, Y. Huai, J. Langer, B. Azzerboni, K. L. Wang, and H. Jiang, *Ultralow-current-density and bias-field-free spin-transfer nano-oscillator*, *Scientific Reports* **3**, (2013).

[16] V. S. Pribiag, I. N. Krivorotov, G. D. Fuchs, P. M. Braganca, O. Ozatay, J. C. Sankey, D. C. Ralph, and R. A. Buhrman, *Magnetic vortex oscillator driven by d.c. spin-polarized current*, *Nature Physics* **3**, 498-503 (2007).

[17] V. Sluka, A. Kákay, A. Deac, D. Bürgler, C. Schneider, and R. Hertel, *Spin-torque-induced dynamics at fine-split frequencies in nano-oscillators with two stacked vortices*, *Nature Communications* **6**, 6409 (2015).

[18] A. S. Jenkins, R. Lebrun, E. Grimaldi, S. Tsunegi, P. Bortolotti, H. Kubota, K. Yakushiji, A. Fukushima, G. de Loubens, O. Klein, S. Yuasa, and V. Cros, *Spin-torque resonant expulsion of the vortex core for an efficient radiofrequency detection scheme*, *Nature Nanotechnology* **11**, 360-364 (2016).

[19] J. Torrejon, M. Riou, F. Abreu Araujo, S. Tsunegi, G. Khalsa, D. Querlioz, P. Bortolotti, V. Cros, K. Yakushiji, A. Fukushima, H. Kubota, S. Yuasa, M. D. Stiles, and J. Grollier, *Neuromorphic computing with nanoscale spintronic oscillators*, *Nature* **547**, 428-431 (2017).

[20] M. Romera, P. Talatchian, S. Tsunegi, F. Abreu Araujo, V. Cros, P. Bortolotti, J. Trastoy, K. Yakushiji, A. Fukushima, H. Kubota, S. Yuasa, M. Ernoult, D. Vodenicarevic, T. Hirtzlin, N. Locatelli, D. Querlioz, and J. Grollier, *Vowel recognition with four coupled spin-torque nano-oscillators*, *Nature* **563**, 230-234 (2018).

[21] A. Grimaldi, L. Sánchez-Tejerina, N. Anjum Aadit, S. Chiappini, M. Carpentieri, K. Camsari, and G. Finocchio, *Spintronics-compatible approach to solving maximum-satisfiability problems with probabilistic computing, invertible logic, and parallel tempering*, *Physical Review Applied* **17**, 024052 (2022).

[22] E. C. Stoner, *Collective electron ferromagnetism*, *Proceedings of the Royal Society of London. Series A - Mathematical and Physical Sciences* **165**, 372-414 (1938).

[23] N. F. Mott, *The electrical conductivity of transition metals*, *Proceedings of the Royal Society of London. Series A - Mathematical and Physical Sciences* **153**, 699-717 (1936).

[24] A. P. Guimarães, *Principles of Nanomagnetism* (NanoScience and Technology, 2009).

[25] M. N. Baibich, J. M. Broto, A. Fert, F. Nguyen Van Dau, F. Petroff, P. Etienne, G. Creuzet, A. Friederich, and J. Chazelas, *Giant Magnetoresis-*

tance of (001)Fe/(001)Cr Magnetic Superlattices, Physical Review Letters **61**, 2472-2475 (1988).

[26] G. Binasch, P. Grünberg, F. Saurenbach, and W. Zinn, *Enhanced magnetoresistance in layered magnetic structures with antiferromagnetic interlayer exchange*, Physical Review B **39**, 4828-4830 (1989).

[27] S. S. P. Parkin, N. More, and K. P. Roche, *Oscillations in exchange coupling and magnetoresistance in metallic superlattice structures: Co/Ru, Co/Cr, and Fe/Cr*, Physical Review Letters **64**, 2304-2307 (1990).

[28] M. Jullière, *Tunneling between ferromagnetic films*, Physics Letters A **54**, 225-226 (1975).

[29] T. Miyazaki, and N. Tezuka, *Giant magnetic tunneling effect in Fe/Al2O3/Fe junction*, Journal of Magnetism and Magnetic Materials **139**, 3 (1995).

[30] J. S. Moodera, L. R. Kinder, T. M. Wong, and R. Meservey, *Large Magnetoresistance at Room Temperature in Ferromagnetic Thin Film Tunnel Junctions*, Physical Review Letters **74**, 3273-3276 (1995).

[31] S. Yuasa, and D. D. Djayaprawira, *Giant tunnel magnetoresistance in magnetic tunnel junctions with a crystalline MgO(001) barrier*, Journal of Physics D: Applied Physics **40**, R337 (2007).

[32] S. Ikeda, J. Hayakawa, Y. Ashizawa, Y. M. Lee, K. Miura, H. Hasegawa, M. Tsunoda, F. Matsukura, and H. Ohno, *Tunnel magnetoresistance of 604% at 300K by suppression of Ta diffusion in CoFeB/MgO/CoFeB pseudo-spin-valves annealed at high temperature*, Applied Physics Letters **93**, 82508 (2008).

[33] J. C. Slonczewski, *Current-driven excitation of magnetic multilayers*, Journal of Magnetism and Magnetic Materials **159**, (1996).

[34] F. J. Albert, J. A. Katine, R. A. Buhrman, and D. C. Ralph, *Spin-polarized current switching of a Co thin film nanomagnet*, Applied Physics Letters **77**, 3809-3811 (2000).

[35] J. Grollier, V. Cros, A. Hamzic, J.-M. George, H. Jaffres, A. Fert, G. Faini, J. Ben Youssef, and H. Legall, *Spin-polarized current induced switching in Co/Cu/Co pillars*, Applied Physics Letters **78**, 3663-3665 (2001).

[36] C. Chappert, A. Fert, and F. Nguyen Van Dau, *The emergence of spin electronics in data storage*, Nature Materials **6**, 813-823 (2007).

[37] D. C. Ralph, and M. D. Stiles, *Spin transfer torques*, Journal of Magnetism and Magnetic Materials **320**, 1190-1216 (2008).

[38] W. F. Brown, *Theory of the Approach to Magnetic Saturation*, Physical Review **58**, 736-743 (1940).

[39] C. Kittel, *Physical Theory of Ferromagnetic Domains*, Reviews of Modern Physics **21**, 541-583 (1949).

[40] J. Urrestarazu Larrañaga, N. Sisodia, R. Guedas, V. T. Pham, I. Di Manici, A. Masseboeuf, K. Garello, F. Disdier, B. Fernandez, S. Wintz, M. Weigand,

M. Belmeguenai, S. Pizzini, R. C. Sousa, L. D. Buda-Prejbeanu, G. Gaudin, and O. Boulle, *Electrical detection and nucleation of a magnetic skyrmion in a magnetic tunnel junction observed via operando magnetic microscopy*, *Nano Letters* **24**, 3557-3565 (2024).

[41] M. Lakshmanan, *The fascinating world of the Landau-Lifshitz-Gilbert equation: an overview*, *Philosophical Transactions of the Royal Society A: Mathematical, Physical and Engineering Sciences* **369**, 1280-1300 (2011).

[42] C. Abert, *Micromagnetics and spintronics: models and numerical methods*, *The European Physical Journal B* **92**, 120 (2019).

[43] L. Landau, and E. Lifshits, *On the Theory of the Dispersion of Magnetic Permeability in Ferromagnetic Bodies*, *Physikalische Zeitschrift der Sowjetunion* **8**, 153-169 (1935).

[44] T. L. Gilbert, *A phenomenological theory of damping in ferromagnetic materials*, *IEEE Transactions on Magnetics* **40**, 3443-3449 (2004).

[45] L. Berger, *Emission of spin waves by a magnetic multilayer traversed by a current*, *Physical Review B* **54**, 9353-9358 (1996).

[46] Z. Li, and S. Zhang, *Magnetization dynamics with a spin-transfer torque*, *Physical Review B* **68**, 24404 (2003).

[47] S. Zhang, and Z. Li, *Roles of Nonequilibrium Conduction Electrons on the Magnetization Dynamics of Ferromagnets*, *Physical Review Letters* **93**, 127204 (2004).

[48] M. J. Donahue, and D. G. Porter, *Object Oriented MicroMagnetic Framework (OOMMF)*, *National Institue of Standards and Technology* (September 29, 2023).

[49] J. J. Joos, P. Bassirian, P. Gypens, J. Mulkers, K. Litzius, B. Van Waeyenberge, and J. Leliaert, *Tutorial: Simulating modern magnetic material systems in mumax3*, *Journal of Applied Physics* **134**, 173903 (2023).

[50] L. Moreels, I. Lateur, D. De Gusem, J. Mulkers, J. Maes, M. V. Milošević, J. Leliaert, and B. Van Waeyenberge, *mumax+: extensible GPU-accelerated micromagnetics and beyond*, *arXiv:2411.18194v3* (2024).

[51] T. Fischbacher, M. Franchin, G. Bordignon, and H. Fangohr, *A Systematic Approach to Multiphysics Extensions of Finite-Element-Based Micromagnetic Simulations: Nmag*, *IEEE Transactions on Magnetics* **43**, 2896-2898 (2007).

[52] G. S. Abo, Y.-K. Hong, J. Park, J. Lee, W. Lee, and B.-C. Choi, *Definition of Magnetic Exchange Length*, *IEEE Transactions on Magnetics* **49**, 4937-4939 (2013).

[53] T. Shinjo, T. Okuno, R. Hassdorf, K. Shigeto, and T. Ono, *Magnetic Vortex Core Observation in Circular Dots of Permalloy*, *Science* **289**, 930-932 (2000).

[54] S.-B. Choe, Y. Acremann, A. Scholl, A. Bauer, A. Doran, J. Stöhr, and H. A. Padmore, *Vortex Core-Driven Magnetization Dynamics*, *Science* **304**, 420-422 (2004).

[55] W. Scholz, K. Y. Guslienko, V. Novosad, D. Suess, T. Schrefl, R. W. Chantrell, and J. Fidler, *Transition from single-domain to vortex state in soft magnetic cylindrical nanodots*, *Journal of Magnetism and Magnetic Materials* **266**, 155-163 (2003).

[56] S.-H. Chung, R. D. McMichael, D. T. Pierce, and J. Unguris, *Phase diagram of magnetic nanodisks measured by scanning electron microscopy with polarization analysis*, *Physical Review B* **81**, 024410 (2010).

[57] M. Goiriena-Goikoetxea, K. Y. Guslienko, M. Rouco, I. Orue, E. Berganza, M. Jaafar, A. Asenjo, M. Fernández-Gubieda, L. Fernández Barquín, and A. García-Arribas, *Magnetization reversal in circular vortex dots of small radius*, *Nanoscale* **9**, 11269-11278 (2017).

[58] D. Vodenicarevic, N. Locatelli, A. Mizrahi, J. S. Friedman, A. F. Vincent, M. Romera, A. Fukushima, K. Yakushiji, H. Kubota, S. Yuasa, S. Tiwari, J. Grollier, and D. Querlioz, *Low-energy truly random number generation with superparamagnetic tunnel junctions for unconventional computing*, *Physical Review Applied* **8**, 054045 (2017).

[59] L. Soumah, L. Desplat, N.-T. Phan, A. S. E. Valli, A. Madhavan, F. Disdier, S. Auffret, R. C. Sousa, U. Ebels, M. D. Stiles, and P. Talatchian, *Entropy-assisted nanosecond stochastic operation in perpendicular superparamagnetic tunnel junctions*, *Physical Review Applied* **24**, L011002 (2025).

[60] K. Y. Guslienko, V. Novosad, Y. Otani, H. Shima, and K. Fukamichi, *Magnetization reversal due to vortex nucleation, displacement, and annihilation in submicron ferromagnetic dot arrays*, *Physical Review B* **65**, 2 (2001).

[61] K. Y. Guslienko, B. A. Ivanov, V. Novosad, Y. Otani, H. Shima, and K. Fukamichi, *Eigenfrequencies of vortex state excitations in magnetic submicron-size disks*, *Journal of Applied Physics* **91**, 8037-8039 (2002).

[62] Y. Gaididei, V. P. Kravchuk, and D. D. Sheka, *Magnetic vortex dynamics induced by an electrical current*, *International Journal of Quantum Chemistry* **110**, 83-97 (2010).

[63] N. A. Usov, and S. E. Peschany, *Magnetization curling in a fine cylindrical particle*, *Journal of Magnetism and Magnetic Materials* **118**, 3 (1993).

[64] E. Feldtkeller, and H. Thomas, *Struktur und Energie von Blochlinien in dünnen ferromagnetischen Schichten*, *Zeitschrift für Physik B: Condensed Matter* **4**, 1 (1965).

[65] R. Höllinger, A. Killinger, and U. Krey, *Statics and fast dynamics of nanomagnets with vortex structure*, *Journal of Magnetism and Magnetic Materials* **261**, 178-189 (2003).

[66] D. L. Huber, *Dynamics of spin vortices in two-dimensional planar magnets*, *Physical Review B* **26**, 3758-3765 (1982).

[67] A. P. Malozemoff, and J. C. Slonczewski, *Magnetic Domain Walls in Bubble Materials* (Elsevier, 1979).

[68] J. Shibata, Y. Nakatani, G. Tatara, H. Kohno, and Y. Otani, *Current-induced magnetic vortex motion by spin-transfer torque*, *Physical Review B* **73**, 2 (2006).

[69] A. R. Völkel, G. M. Wysin, F. G. Mertens, A. R. Bishop, and H. J. Schnitzer, *Collective-variable approach to the dynamics of nonlinear magnetic excitations with application to vortices*, *Physical Review B* **50**, 12711 (1994).

[70] G. M. Wysin, *Magnetic vortex mass in two-dimensional easy-plane magnets*, *Physical Review B* **54**, 15156 (1996).

[71] F. G. Mertens, H. J. Schnitzer, and A. R. Bishop, *Hierarchy of equations of motion for nonlinear coherent excitations applied to magnetic vortices*, *Physical Review B* **56**, 2510 (1997).

[72] B. A. Ivanov, H. J. Schnitzer, F. G. Mertens, and G. M. Wysin, *Magnon modes and magnon-vortex scattering in two-dimensional easy-plane ferromagnets*, *Physical Review B* **58**, 8464 (1998).

[73] D. D. Sheka, B. A. Ivanov, and F. G. Mertens, *Internal modes and magnon scattering on topological solitons in two-dimensional easy-axis ferromagnets*, *Physical Review B* **64**, 024432 (2001).

[74] D. D. Sheka, C. Schuster, B. A. Ivanov, and F. G. Mertens, *Dynamics of topological solitons in two-dimensional ferromagnets*, *The European Physical Journal B* **50**, 393-402 (2006).

[75] K. Y. Guslienko, G. N. Kakazei, J. Ding, X. M. Liu, and A. O. Adeyeye, *Giant moving vortex mass in thick magnetic nanodots*, *Scientific Reports* **5**, 13881 (2015).

[76] M.-W. Yoo, F. Mineo, and J.-V. Kim, *Analytical model of the deformation-induced inertial dynamics of a magnetic vortex*, *Journal of Applied Physics* **129**, 053903 (2021).

[77] Z. Gareeva, and K. Guslienko, *Nutation excitations in the gyrotropic vortex dynamics in a circular magnetic nanodot*, *Nanomaterials* **13**, 461 (2023).

[78] K. Y. Guslienko, *Magnetic Vortex Core String Gyrotropic Oscillations in Thick Cylindrical Dots*, *Magnetism* **2**, 239-250 (2022).

[79] K. Y. Guslienko, G. R. Aranda, and J. Gonzalez, *Spin torque and critical currents for magnetic vortex nano-oscillator in nanopillars*, *Journal of Physics: Conference Series* **292**, 1742-6596 (2011).

[80] K. Y. Guslienko, O. V. Sukhostavets, and D. V. Berkov, *Nonlinear magnetic vortex dynamics in a circular nanodot excited by spin-polarized current*, *Nanoscale Research Letters* 386 (2014).

[81] A. Dussaux, B. Georges, J. Grollier, V. Cros, A. V. Khvalkovskiy, A. Fukushima, M. Konoto, H. Kubota, K. Yakushiji, S. Yuasa, K. A. Zvezdin, K. Ando, and A. Fert, *Large microwave generation from current-driven magnetic vortex oscillators in magnetic tunnel junctions*, *Nature Communications* **1**, 8 (2010).

[82] K. Y. Guslienko, X. F. Han, D. J. Keavney, R. Divan, and S. D. Bader, *Magnetic Vortex Core Dynamics in Cylindrical Ferromagnetic Dots*, *Physical Review Letters* **96**, 67205 (2006).

[83] Y. Imai, S. Tsunegi, K. Nakajima, and T. Taniguchi, *Noise-induced synchronization of spin-torque oscillators*, *Physical Review B* **105**, 224407 (2022).

[84] A. V. Khvalkovskiy, J. Grollier, A. Dussaux, K. A. Zvezdin, and V. Cros, *Vortex oscillations induced by spin-polarized current in a magnetic nanopillar: Analytical versus micromagnetic calculations*, *Physical Review B* **80**, 140401 (2009).

[85] F. Abreu Araujo, A. D. Belanovsky, P. N. Skirdkov, K. A. Zvezdin, A. K. Zvezdin, N. Locatelli, R. Lebrun, J. Grollier, V. Cros, G. de Loubens, and O. Klein, *Optimizing magnetodipolar interactions for synchronizing vortex based spin-torque nano-oscillators*, *Physical Review B* **92**, 45419 (2015).

[86] A. Dussaux, A. V. Khvalkovskiy, P. Bortolotti, J. Grollier, V. Cros, and A. Fert, *Field dependence of spin-transfer-induced vortex dynamics in the nonlinear regime*, *Physical Review B* **86**, 14402 (2012).

[87] E. Grimaldi, A. Dussaux, P. Bortolotti, J. Grollier, G. Pillet, A. Fukushima, H. Kubota, K. Yakushiji, S. Yuasa, and V. Cros, *Response to noise of a vortex based spin transfer nano-oscillator*, *Physical Review B* **89**, 10 (2014).

[88] K. Y. Guslienko, *Low-frequency vortex dynamic susceptibility and relaxation in mesoscopic ferromagnetic dots*, *Applied Physics Letters* **89**, 22510 (2006).

[89] A. V. Khvalkovskiy, A. N. Slavin, J. Grollier, K. A. Zvezdin, and K. Y. Guslienko, *Critical velocity for the vortex core reversal in perpendicular bias magnetic field*, *Applied Physics Letters* **96**, 22504 (2010).

[90] C. Heiliger, and M. D. Stiles, *Ab initio studies of the spin-transfer torque in magnetic tunnel junctions*, *Physical Review Letters* **100**, 186805 (2008).

[91] K. Y. Guslienko, V. Novosad, Y. Otani, H. Shima, and K. Fukamichi, *Magnetization reversal due to vortex nucleation, displacement, and annihilation in submicron ferromagnetic dot arrays*, *Physical Review B* **65**, 024414 (2001).

[92] K. Y. Guslienko, and K. L. Metlov, *Evolution and stability of a magnetic vortex in a small cylindrical ferromagnetic particle under applied field*, *Physical Review B* **63**, 100403 (2001).

[93] J. P. Fried, and P. J. Metaxas, *Localized magnetic fields enhance the field sensitivity of the gyrotropic resonance frequency of a magnetic vortex*, *Physical Review B* **93**, 064422 (2016).

[94] J. P. Fried, H. Fangohr, M. Kostylev, and P. J. Metaxas, *Exchange-mediated, nonlinear, out-of-plane magnetic field dependence of the ferromagnetic vortex gyrotropic mode frequency driven by core deformation*, *Physical Review B* **94**, 224407 (2016).

[95] G. de Loubens, A. Riegler, B. Pigeau, F. Lochner, F. Boust, K. Y. Guslienko, H. Hurdequint, L. W. Molenkamp, G. Schmidt, A. N. Slavin, V. S. Tiberkevich, N. Vukadinovic, and O. Klein, *Bistability of Vortex Core Dynamics in a Single Perpendicularly Magnetized Nanodisk*, *Physical Review Letters* **102**, 177602 (2009).

[96] B. Krüger, A. Drews, M. Bolte, U. Merkt, D. Pfannkuche, and G. Meier, *Harmonic oscillator model for current- and field-driven magnetic vortices*, *Physical Review B* **76**, 224426 (2007).

[97] S. Urazhdin, C. L. Chien, K. Y. Guslienko, and L. Novozhilova, *Effects of current on the magnetic states of permalloy nanodiscs*, *Physical Review B* **73**, 5 (2006).

[98] A. S. Jenkins, E. Grimaldi, P. Bortolotti, R. Lebrun, H. Kubota, K. Yakushiji, A. Fukushima, G. de Loubens, O. Klein, S. Yuasa, and V. Cros, *Controlling the chirality and polarity of vortices in magnetic tunnel junctions*, *Applied Physics Letters* **105**, 17 (2014).

[99] Y.-S. Choi, S.-K. Kim, K.-S. Lee, and Y.-S. Yu, *Understanding eigenfrequency shifts observed in vortex gyrotropic motions in a magnetic nanodot driven by spin-polarized out-of-plane dc current*, *Applied Physics Letters* **93**, 182508 (2008).

[100] Y.-S. Choi, K.-S. Lee, and S.-K. Kim, *Quantitative understanding of magnetic vortex oscillations driven by spin-polarized out-of-plane dc current: Analytical and micromagnetic numerical study*, *Physical Review B* **79**, 184424 (2009).

[101] A. Kumar, A. K. Chaurasiya, V. H. González, N. Behera, A. Alemán, R. Khymyn, A. A. Awad, and J. Åkerman, *Spin-wave-mediated mutual synchronization and phase tuning in spin Hall nano-oscillators*, *Nature Physics* **21**, 245-252 (2025).

[102] J.-R. Chen, A. Smith, E. A. Montoya, J. G. Lu, and I. N. Krivorotov, *Spin-orbit torque nano-oscillator with giant magnetoresistance readout*, *Communications Physics* **3**, 187 (2020).

[103] W. H. Rippard, M. R. Pufall, S. Kaka, S. E. Russek, and T. J. Silva, *Direct-current induced dynamics in Co90Fe10/Ni80Fe20 point contacts*, *Physical Review Letters* **92**, 027201 (2004).

[104] I. N. Krivorotov, N. C. Emley, J. C. Sankey, S. I. Kiselev, D. C. Ralph, and R. A. Buhrman, *Time-domain measurements of nanomagnet dynamics driven by spin-transfer torques*, *Science* **307**, 228-231 (2005).

[105] A. M. Deac, A. Fukushima, H. Kubota, H. Maehara, Y. Suzuki, S. Yuasa, Y. Nagamine, K. Tsunekawa, D. D. Djayaprawira, and N. Watanabe, *Bias-driven high-power microwave emission from MgO-based tunnel magnetoresistance devices*, *Nature Physics* **4**, 803-809 (2008).

[106] Q. Mistral, M. van Kampen, G. Hrkac, J.-V. Kim, T. Devolder, P. Crozat, C. Chappert, L. Lagae, and T. Schrefl, *Current-Driven Vortex Oscillations in Metallic Nanocontacts*, *Physical Review Letters* **100**, 257201 (2008).

[107] D. V. Berkov, and N. L. Gorn, *Spin-torque driven magnetization dynamics in a nanocontact setup for low external fields: Numerical simulation study*, *Physical Review B* **80**, 064409 (2009).

[108] A. A. Tulapurkar, Y. Suzuki, A. Fukushima, H. Kubota, H. Maehara, K. Tsunekawa, D. D. Djayaprawira, N. Watanabe, and S. Yuasa, *Spin-torque diode effect in magnetic tunnel junctions*, *Nature* **438**, 339-342 (2005).

[109] G. A. Kichin, P. N. Skirdkov, and K. A. Zvezdin, *Ultrawide broadband rectification effect in an in-plane magnetic tunnel junction*, *Physical Review Applied* **20**, 044078 (2023).

[110] A. S. Jenkins, L. San Emeterio Alvarez, R. Dutra, R. L. Sommer, P. P. Freitas, and R. Ferreira, *Wideband high-resolution frequency-to-resistance converter based on nonhomogeneous magnetic-state transitions*, *Physical Review Applied* **13**, 014046 (2020).

[111] J. Grollier, D. Querlioz, K. Y. Camsari, K. Everschor-Sitte, S. Fukami, and M. D. Stiles, *Neuromorphic spintronics*, *Nature Electronics* **3**, 360-370 (2020).

[112] F. Abreu Araujo, M. Riou, J. Torrejon, S. Tsunegi, D. Querlioz, K. Yakushiji, A. Fukushima, H. Kubota, S. Yuasa, M. D. Stiles, and J. Grollier, *Role of non-linear data processing on speech recognition task in the framework of reservoir computing*, *Scientific Reports* **10**, 328 (2020).

[113] L. Martins, A. S. Jenkins, L. S. E. Alvarez, J. Borme, T. Böhnert, J. Ventura, P. P. Freitas, and R. Ferreira, *Non-volatile artificial synapse based on a vortex nano-oscillator*, *Scientific Reports* **11**, 16094 (2021).

[114] A. Ross, N. Leroux, A. De Riz, D. Marković, D. Sanz-Hernández, J. Trastoy, P. Bortolotti, D. Querlioz, L. Martins, L. Benetti, M. S. Claro, P. Anacleto, A. Schulman, T. Taris, J.-B. Begueret, S. Saïghi, A. S. Jenkins, R. Ferreira, A. F. Vincent, F. A. Mizrahi, and J. Grollier, *Multilayer spintronic neural networks with radiofrequency connections*, *Nature Nanotechnology* **18**, 1273-1280 (2023).

[115] J. C. Gartside, K. D. Stenning, A. Vanstone, H. H. Holder, D. M. Arroo, T. Dion, F. Caravelli, H. Kurebayashi, and W. R. Branford, *Reconfigurable training and reservoir computing in an artificial spin-vortex ice via spin-wave fingerprinting*, *Nature Nanotechnology* **17**, 460-469 (2022).

[116] L. Körber, C. Heins, T. Hula, J.-V. Kim, S. Thlang, H. Schultheiss, J. Fassbender, and K. Schultheiss, *Pattern recognition in reciprocal space with a magnon-scattering reservoir*, *Nature Communications* **14**, 3954 (2023).

[117] G. Bourianoff, D. Pinna, M. Sitte, and K. Everschor-Sitte, *Potential implementation of reservoir computing models based on magnetic skyrmions*, *AIP Advances* **8**, 5 (2018).

[118] T. da Câmara Santa Clara Gomes, Y. Sassi, D. Sanz-Hernández, S. Krishnia, S. Collin, M.-B. Martin, P. Seneor, V. Cros, J. Grollier, and N. Reyren, *Neuromorphic weighted sums with magnetic skyrmions*, *Nature Electronics* **8**, 204-214 (2025).

[119] D. Wang, R. Tang, H. Lin, L. Liu, N. Xu, Y. Sun, X. Zhao, Z. Wang, D. Wang, Z. Mai, Y. Zhou, N. Gao, C. Song, L. Zhu, T. Wu, M. Liu, and G. Xing, *Spintronic leaky-integrate-fire spiking neurons with self-reset and winner-takes-all for neuromorphic computing*, *Nature Communications* **14**, 1068 (2023).

[120] A. D. Belanovsky, N. Locatelli, P. N. Skirdkov, F. Abreu Araujo, J. Grollier, K. A. Zvezdin, V. Cros, and A. K. Zvezdin, *Phase locking dynamics of dipolarly coupled vortex-based spin transfer oscillators*, *Physical Review B* **85**, 100409 (2012).

[121] N. Locatelli, A. Hamadeh, F. Abreu Araujo, A. D. Belanovsky, P. N. Skirdkov, R. Lebrun, V. V. Naletov, K. A. Zvezdin, M. Muñoz, J. Grollier, O. Klein, V. Cros, and G. de Loubens, *Efficient Synchronization of Dipolarly Coupled Vortex-Based Spin Transfer Nano-Oscillators*, *Scientific Reports* **5**, 17039 (2015).

[122] P. N. Skirdkov, A. F. Popkov, and K. A. Zvezdin, *Vortex spin-torque diode: The impact of DC bias*, *Applied Physics Letters* **113**, 24 (2018).

[123] M. Carpentieri, G. Finocchio, B. Azzerboni, L. Torres, L. Lopez-Diaz, and E. Martinez, *Effect of the classical ampere field in micromagnetic computations of spin polarized current-driven magnetization processes*, *Journal of Applied Physics* **97**, 103903 (2005).

[124] K.-J. Lee, A. Deac, O. Redon, J.-P. Nozieres, and B. Dieny, *Excitations of incoherent spin-waves due to spin-transfer torque*, *Nature Materials* **3**, 877-881 (2004).

[125] F. Abreu Araujo, C. Chopin, and **S. de Wergifosse**, *Ampère-Oersted field splitting of the nonlinear spin-torque vortex oscillator dynamics*, *Scientific Reports* **12**, 10605 (2022).

[126] **S. de Wergifosse**, C. Chopin, and F. Abreu Araujo, *Quantitative and realistic description of the magnetic potential energy of spin-torque vortex oscillators*, *Physical Review B* **108**, 174403 (2023).

[127] F. Abreu Araujo, and J. Grollier, *Controlling the synchronization properties of two dipolarly coupled vortex based spin-torque nano-oscillators by the intermediate of a third one*, *Journal of Applied Physics* **120**, 103903 (2016).

[128] S. Wittrock, P. Talatchian, M. Romera, S. Menshawy, M. Jotta Garcia, M.-C. Cyrille, R. Ferreira, R. Lebrun, P. Bortolotti, U. Ebels, J. Grollier, and V. Cros, *Beyond the gyrotropic motion: Dynamic c-state in vortex spin torque oscillators*, *Applied Physics Letters* **118**, 1 (2021).
[129] R. P. Cowburn, *Property variation with shape in magnetic nanoelements*, *Journal of Physics D: Applied Physics* **33**, R1 (2000).
[130] C. A. F. Vaz, J. A. C. Bland, and G. Lauhoff, *Magnetism in ultrathin film structures*, *Reports on Progress in Physics* **71**, 56501 (2008).
[131] F. Abreu Araujo, *Python package SNIFA*, *PyPI* (2021).
[132] B. A. Ivanov, and C. E. Zaspel, *Excitation of Spin Dynamics by Spin-Polarized Current in Vortex State Magnetic Disks*, *Physical Review Letters* **99**, 247208 (2007).
[133] K. S. Buchanan, P. E. Roy, M. Grimsditch, F. Y. Fradin, K. Y. Guslienko, S. D. Bader, and V. Novosad, *Magnetic-field tunability of the vortex translational mode in micron-sized permalloy ellipses: Experiment and micromagnetic modeling*, *Physical Review B* **74**, 64404 (2006).
[134] G. R. Lee, R. Gommers, F. Waselewski, K. Wohlfahrt, and A. O'Leary, *PyWavelets: A Python package for wavelet analysis*, *Journal of Open Source Software* **4**, 1237 (2019).
[135] K. Y. Guslienko, K.-S. Lee, and S.-K. Kim, *Dynamic Origin of Vortex Core Switching in Soft Magnetic Nanodots*, *Physical Review Letters* **100**, 27203 (2008).
[136] S. Kasai, Y. Nakatani, K. Kobayashi, H. Kohno, and T. Ono, *Current-Driven Resonant Excitation of Magnetic Vortices*, *Physical Review Letters* **97**, 107204 (2006).
[137] R. Hertel, S. Gliga, M. Fähnle, and C. M. Schneider, *Ultrafast nanomagnetic toggle switching of vortex cores*, *Physical Review Letters* **98**, 117201 (2007).
[138] S. Gliga, Y. Liu, and R. Hertel, *Energy thresholds in the magnetic vortex core reversal*, *Journal of Physics: Conference Series* **303**, 012005 (2011).
[139] K.-S. Lee, S.-K. Kim, Y.-S. Yu, Y.-S. Choi, K. Y. Guslienko, H. Jung, and P. Fischer, *Universal Criterion and Phase Diagram for Switching a Magnetic Vortex Core in Soft Magnetic Nanodots*, *Physical Review Letters* **101**, 267206 (2008).
[140] K. Y. Guslienko, X. F. Han, D. J. Keavney, R. Divan, and S. D. Bader, *Magnetic vortex core dynamics in cylindrical ferromagnetic dots*, *Physical Review Letters* **96**, 067205 (2006).
[141] I. L. Prejbeanu, W. Kula, K. Ounadjela, R. C. Sousa, O. Redon, B. Dieny, and J.-P. Nozieres, *Thermally assisted switching in exchange-biased storage layer magnetic tunnel junctions*, *IEEE Transactions on Magnetics* **40**, 2625-2627 (2004).

[142] I. L. Prejbeanu, S. Bandiera, J. Alvarez-Hérault, R. C. Sousa, B. Dieny, and J.-P. Nozières, *Thermally assisted MRAMs: ultimate scalability and logic functionalities*, *Journal of Physics D: Applied Physics* **46**, 074002 (2013).

[143] N. Strelkov, A. Chavent, A. Timopheev, R. Sousa, I. L. Prejbeanu, L. D. Buda-Prejbeanu, and B. Dieny, *Impact of Joule heating on the stability phase diagrams of perpendicular magnetic tunnel junctions*, *Physical Review B* **98**, 214410 (2018).

[144] D. H. Lee, and S. H. Lim, *Increase of temperature due to Joule heating during current-induced magnetization switching of an MgO-based magnetic tunnel junction*, *Applied Physics Letters* **92**, 23 (2008).

[145] F. Abreu Araujo, C. Chopin, and **S. de Wergifosse**, *Data-driven Thiele equation approach for solving the full nonlinear spin-torque vortex oscillator dynamics*, *arXiv:2206.13596* (2022).

[146] A. Moureaux, **S. de Wergifosse**, C. Chopin, J. Weber, and F. Abreu Araujo, *Neuromorphic spintronics accelerated by an unconventional data-driven Thiele equation approach*, *arXiv:2301.11025v2* (2023).

[147] A. Moureaux, C. Chopin, **S. de Wergifosse**, L. Jacques, and F. Abreu Araujo, *Spintronics for image recognition: performance benchmarking via ultrafast data-driven simulations*, *arXiv:2308.05810v3* (2023).

[148] C. Chopin, **S. de Wergifosse**, A. Moureaux, and F. Abreu Araujo, *Current-controlled periodic double-polarity reversals in a spin-torque vortex oscillator*, *Scientific Reports* **14**, 24177 (2024).

[149] J. Leliaert, and J. Mulkers, *Tomorrow's micromagnetic simulations*, *Journal of Applied Physics* **125**, 180901 (2019).

[150] J.-H. Shim, H.-G. Piao, S. Hyuk Lee, S. Kun Oh, S.-C. Yu, S. Kee Han, and D.-H. Kim, *Nonlinear motion of magnetic vortex under alternating-current magnetic field: Dynamic correction of a gyrovector and a damping tensor of the Thiele's equation*, *Applied Physics Letters* **99**, 14 (2011).

[151] C. Ducarme, **S. de Wergifosse**, and F. Abreu Araujo, *Core position-dependent gyrotropic and damping contributions to the Thiele equation approach for accurate spin-torque vortex oscillator dynamics*, *arXiv:2508.14829v2* (2025).

[152] T. Okuno, K. Shigeto, T. Ono, K. Mibu, and T. Shinjo, *MFM study of magnetic vortex cores in circular permalloy dots: behavior in external field*, *Journal of Magnetism and Magnetic Materials* **240**, 1-6 (2002).

[153] A. Thiaville, J. M. García, R. Dittrich, J. Miltat, and T. Schrefl, *Micromagnetic study of Bloch-point-mediated vortex core reversal*, *Physical Review B* **67**, 094410 (2003).

[154] Q. F. Xiao, J. Rudge, B. C. Choi, Y. K. Hong, and G. Donohoe, *Dynamics of vortex core switching in ferromagnetic nanodisks*, *Applied Physics Letters* **89**, 26 (2006).

[155] B. Van Waeyenberge, A. Puzic, H. Stoll, K. W. Chou, T. Tyliszczak, R. Hertel, M. Fähnle, H. Brückl, K. Rott, G. Reiss, I. Neudecker, D. Weiss, C. H. Back, and G. Schütz, *Magnetic vortex core reversal by excitation with short bursts of an alternating field*, *Nature* **444**, 461-464 (2006).

[156] S. Choi, K.-S. Lee, K. Y. Guslienko, and S.-K. Kim, *Strong Radiation of Spin Waves by Core Reversal of a Magnetic Vortex and Their Wave Behaviors in Magnetic Nanowire Waveguides*, *Physical Review Letters* **98**, 087205 (2007).

[157] R. Wang, and X. Dong, *Sub-nanosecond switching of vortex cores using a resonant perpendicular magnetic field*, *Applied Physics Letters* **100**, 082402 (2012).

[158] M.-W. Yoo, J. Lee, and S.-K. Kim, *Radial-spin-wave-mode-assisted vortex-core magnetization reversals*, *Applied Physics Letters* **100**, 17 (2012).

[159] X.-P. Ma, M.-X. Cai, P. Li, J.-H. Shim, H.-G. Piao, and D.-H. Kim, *Periodic vortex core switching in curved magnetic nanodisk*, *Journal of Magnetism and Magnetic Materials* **502**, 166481 (2020).

[160] K.-S. Lee, K. Y. Guslienko, J.-Y. Lee, and S.-K. Kim, *Ultrafast vortex-core reversal dynamics in ferromagnetic nanodots*, *Physical Review B* **76**, 174410 (2007).

[161] M. Curcic, B. Van Waeyenberge, A. Vansteenkiste, M. Weigand, V. Sackmann, H. Stoll, M. Fähnle, T. Tyliszczak, G. Woltersdorf, C. H. Back, and G. Schütz, *Polarization selective magnetic vortex dynamics and core reversal in rotating magnetic fields*, *Physical Review Letters* **101**, 197204 (2008).

[162] K. Yamada, S. Kasai, Y. Nakatani, K. Kobayashi, H. Kohno, A. Thiaville, and T. Ono, *Electrical switching of the vortex core in a magnetic disk*, *Nature Materials* **6**, 270-273 (2007).

[163] S.-K. Kim, Y.-S. Choi, K.-S. Lee, K. Y. Guslienko, and D.-E. Jeong, *Electric-current-driven vortex-core reversal in soft magnetic nanodots*, *Applied Physics Letters* **91**, 82506 (2007).

[164] Y. Liu, S. Gliga, R. Hertel, and C. M. Schneider, *Current-induced magnetic vortex core switching in a Permalloy nanodisk*, *Applied Physics Letters* **91**, 11 (2007).

[165] D. D. Sheka, Y. Gaididei, and F. G. Mertens, *Current induced switching of vortex polarity in magnetic nanodisks*, *Applied Physics Letters* **91**, 8 (2007).

[166] S. Petit-Watelot, J.-V. Kim, A. Ruotolo, R. M. Otxoa, K. Bouzehouane, J. Grollier, A. Vansteenkiste, B. Van de Wiele, V. Cros, and T. Devolder, *Commensurability and chaos in magnetic vortex oscillations*, *Nature Physics* **8**, 682-687 (2012).

[167] M.-W. Yoo, D. Rontani, J. Létang, S. Petit-Watelot, T. Devolder, M. Sciamanna, K. Bouzehouane, V. Cros, and J.-V. Kim, *Pattern generation and symbolic dynamics in a nanocontact vortex oscillator*, *Nature Communications* **11**, 601 (2020).

[168] C. Chopin, L. Martins, L. Benetti, **S. de Wergifosse**, A. S. Jenkins, R. Ferreira, and F. Abreu Araujo, *A semi-analytical model to simulate the spin-diode effect and accelerate its use in neuromorphic computing*, *arXiv:2301.11980* (2023).

[169] M.-W. Yoo, K.-S. Lee, D.-E. Jeong, and S.-K. Kim, *Origin, criterion, and mechanism of vortex-core reversals in soft magnetic nanodisks under perpendicular bias fields*, *Physical Review B* **82**, 174437 (2010).

[170] R. Hertel, and C. M. Schneider, *Exchange explosions: magnetization dynamics during vortex-antivortex annihilation*, *Physical Review Letters* **97**, 177202 (2006).

[171] M. J. Rozenberg, O. Schneegans, and P. Stoliar, *An ultra-compact leaky-integrate-and-fire model for building spiking neural networks*, *Scientific Reports* **9**, 11123 (2019).

[172] D. Marković, N. Leroux, A. Mizrahi, J. Trastoy, V. Cros, P. Bortolotti, L. Martins, A. S. Jenkins, R. Ferreira, and J. Grollier, *Detection of the microwave emission from a spin-torque oscillator by a spin diode*, *Physical Review Applied* **13**, 044050 (2020).

[173] D. I. Albertsson, M. Zahedinejad, A. Houshang, R. Khymyn, J. Åkerman, and A. Rusu, *Ultrafast Ising Machines using spin torque nano-oscillators*, *Applied Physics Letters* **118**, 11 (2021).

[174] N. A. Aadit, A. Grimaldi, M. Carpentieri, L. Theogarajan, J. M. Martinis, G. Finocchio, and K. Y. Camsari, *Massively parallel probabilistic computing with sparse Ising machines*, *Nature Electronics* **5**, 460-468 (2022).

[175] B. Georges, J. Grollier, V. Cros, and A. Fert, *Impact of the electrical connection of spin transfer nano-oscillators on their synchronization: an analytical study*, *Applied Physics Letters* **92**, 232504 (2008).

[176] J. Turtle, P.-L. Buono, A. Palacios, C. Dabrowski, V. In, and P. Longhini, *Synchronization of spin torque nano-oscillators*, *Physical Review B* **95**, 144412 (2017).

[177] R. Lebrun, S. Tsunegi, P. Bortolotti, H. Kubota, A. S. Jenkins, M. Romera, K. Yakushiji, A. Fukushima, J. Grollier, S. Yuasa, and V. Cros, *Mutual synchronization of spin torque nano-oscillators through a long-range and tunable electrical coupling scheme*, *Nature Communications* **8**, 15825 (2017).

[178] T. Taniguchi, S. Tsunegi, and H. Kubota, *Mutual synchronization of spin-torque oscillators consisting of perpendicularly magnetized free layers and in-plane magnetized pinned layers*, *Applied Physics Express* **11**, 013005 (2017).

[179] S. Tsunegi, T. Taniguchi, R. Lebrun, K. Yakushiji, V. Cros, J. Grollier, A. Fukushima, S. Yuasa, and H. Kubota, *Scaling up electrically synchronized spin torque oscillator networks*, *Scientific Reports* **8**, 13475

[180] P. Talatchian, M. Romera, F. Abreu Araujo, P. Bortolotti, V. Cros, D. Vodenicarevic, N. Locatelli, D. Querlioz, and J. Grollier, *Designing Large Arrays of Interacting Spin-Torque Nano-Oscillators for Microwave Information Processing*, *Physical Review Applied* **13**, 24073 (2020).

[181] S. Perna, M. Anand, G. Oliviero, A. Quercia, M. d'Aquino, S. Wittrock, R. Lebrun, V. Cros, and C. Serpico, *Coupling-induced bistability in self-oscillating regimes of two coupled identical Spin-Torque Nano-oscillators*, *Physica B: Condensed Matter* **674**, 415594 (2024).

[182] A. A. Matveev, A. R. Safin, and S. A. Nikitov, *Exceptional points in coupled vortex-based spin-torque oscillators*, *Physical Review B* **108**, 174443 (2023).

[183] S. Wittrock, S. Perna, R. Lebrun, K. Ho, R. Dutra, R. Ferreira, P. Bortolotti, C. Serpico, and V. Cros, *Non-hermiticity in spintronics: oscillation death in coupled spintronic nano-oscillators through emerging exceptional points*, *Nature Communications* **15**, 971 (2024).

[184] J. Shibata, K. Shigeto, and Y. Otani, *Dynamics of magnetostatically coupled vortices in magnetic nanodisks*, *Physical Review B* **67**, 224404 (2003).

[185] J. Shibata, and Y. Otani, *Magnetic vortex dynamics in a two-dimensional square lattice of ferromagnetic nanodisks*, *Physical Review B* **70**, 012404 (2004).

[186] A. D. Belanovsky, N. Locatelli, P. N. Skirdkov, F. Abreu Araujo, K. A. Zvezdin, J. Grollier, V. Cros, and A. K. Zvezdin, *Numerical and analytical investigation of the synchronization of dipolarly coupled vortex spin-torque nano-oscillators*, *Applied Physics Letters* **103**, 122405 (2013).

[187] O. V. Sukhostavets, J. González, and K. Y. Guslienko, *Multipole magnetostatic interactions and collective vortex excitations in dot pairs, chains, and two-dimensional arrays*, *Physical Review B* **87**, 9 (2013).

[188] L. Martins, A. S. Jenkins, J. Borme, J. Ventura, P. P. Freitas, and R. Ferreira, *Second harmonic injection locking of coupled spin torque vortex oscillators with an individual phase access*, *Communications Physics* **6**, 72 (2023).

[189] Y. Li, X. De Milly, O. Klein, V. Cros, J. Grollier, and G. de Loubens, *Selective control of vortex polarities by microwave field in two robustly synchronized spin-torque nano-oscillators*, *Applied Physics Letters* **112**, 2 (2018).

[190] R. L. Compton, and P. A. Crowell, *Dynamics of a pinned magnetic vortex*, *Physical Review Letters* **97**, 137202 (2006).

[191] R. L. Compton, T. Y. Chen, and P. A. Crowell, *Magnetic vortex dynamics in the presence of pinning*, *Physical Review B* **81**, 144412 (2010).

[192] K. Y. Guslienko, R. H. Heredero, and O. Chubykalo-Fesenko, *Nonlinear gyrotropic vortex dynamics in ferromagnetic dots*, *Physical Review B* **82**, 1 (2010).

[193] V. Novosad, F. Y. Fradin, P. E. Roy, K. S. Buchanan, K. Y. Guslienko, and S. D. Bader, *Magnetic vortex resonance in patterned ferromagnetic dots*, *Physical Review B* **72**, 024455 (2005).

[194] T. Y. Chen, A. T. Galkiewicz, and P. A. Crowell, *Phase diagram of magnetic vortex dynamics*, *Physical Review B* **85**, 180406 (2012).

[195] K.-S. Lee, and S.-K. Kim, *Gyrotropic linear and nonlinear motions of a magnetic vortex in soft magnetic nanodots*, *Applied Physics Letters* **91**, 132511 (2007).

[196] K.-S. Lee, and S.-K. Kim, *Two circular-rotational eigenmodes and their giant resonance asymmetry in vortex gyrotropic motions in soft magnetic nanodots*, *Physical Review B* **78**, 1 (2008).

[197] A. Drews, B. Krüger, G. Selke, T. Kamionka, A. Vogel, M. Martens, U. Merkt, D. Möller, and G. Meier, *Nonlinear magnetic vortex gyration*, *Physical Review B* **85**, 144417 (2012).

[198] S. Urazhdin, P. Tabor, V. S. Tiberkevich, and A. N. Slavin, *Fractional Synchronization of Spin-Torque Nano-Oscillators*, *Physical Review Letters* **105**, 104101 (2010).

[199] A. Vogel, A. Drews, T. Kamionka, M. Bolte, and G. Meier, *Influence of Dipolar Interaction on Vortex Dynamics in Arrays of Ferromagnetic Disks*, *Physical Review Letters* **105**, 37201 (2010).

[200] V. Novosad, K. Y. Guslienko, H. Shima, Y. Otani, S. G. Kim, K. Fukamichi, N. Kikuchi, O. Kitakami, and Y. Shimada, *Effect of interdot magnetostatic interaction on magnetization reversal in circular dot arrays*, *Physical Review B* **65**, 060402 (2002).

[201] M. Grimsditch, P. Vavassori, V. Novosad, V. Metlushko, H. Shima, Y. Otani, and K. Fukamichi, *Vortex chirality in an array of ferromagnetic dots*, *Physical Review B* **65**, 172419 (2002).

[202] K. S. Buchanan, K. Y. Guslienko, A. Doran, A. Scholl, S. D. Bader, and V. Novosad, *Magnetic remanent states and magnetization reversal in patterned trilayer nanodots*, *Physical Review B* **72**, 134415 (2005).

[203] M. Bolte, G. Meier, B. Krüger, A. Drews, R. Eiselt, L. Bocklage, S. Bohlens, T. Tyliszczak, A. Vansteenkiste, B. Van Waeyenberge, K. W. Chou, A. Puzic, and H. Stoll, *Time-resolved x-ray microscopy of spin-torque-induced magnetic vortex gyration*, *Physical Review Letters* **100**, 176601 (2008).

[204] W.-Y. Kim, and K.-J. Lee, *Effect of current-induced magnetic field on magnetization dynamics in spin-torque nano-oscillator with point-contact geometry*, *Current Applied Physics* **13**, 890-893 (2013).

[205] A. S. Jenkins, L. Martins, L. C. Benetti, A. Schulman, P. Anacleto, M. S. Claro, I. Caha, F. L. Deepak, E. Paz, and R. Ferreira, *The impact of local pinning sites in magnetic tunnel junctions with non-homogeneous free layers*, *Communications Materials* **5**, 7 (2024).

[206] H. Min, R. D. McMichael, J. Miltat, and M. D. Stiles, *Effects of disorder on magnetic vortex gyration*, *Physical Review B* **83**, 064411 (2011).

[207] M. Rahm, J. Biberger, V. Umansky, and D. Weiss, *Vortex pinning at individual defects in magnetic nanodisks*, *Journal of Applied Physics* **93**, 7429-7431 (2003).

[208] T. Uhlig, M. Rahm, C. Dietrich, R. Höllinger, M. Heumann, D. Weiss, and J. Zweck, *Shifting and pinning of a magnetic vortex core in a permalloy dot by a magnetic field*, *Physical Review Letters* **95**, 237205 (2005).

[209] S. Martin, N. de Mestier, C. Thirion, C. Hoarau, Y. Conraux, C. Baraduc, and B. Diény, *Parametric oscillator based on nonlinear vortex dynamics in low-resistance magnetic tunnel junctions*, *Physical Review B* **84**, 144434 (2011).

[210] S. Wintz, V. Tiberkevich, M. Weigand, J. Raabe, J. Lindner, A. Erbe, A. N. Slavin, and J. Fassbender, *Magnetic vortex cores as tunable spin-wave emitters*, *Nature Nanotechnology* **11**, 948-953 (2016).